UNIVERSITY OF CALIFORNIA, MERCED

INVERSE APPROACHES FOR IDENTIFICATION OF CONSTITUTIVE LAWS OF SLENDER STRUCTURES MOTIVATED BY APPLICATION TO BIOLOGICAL FILAMENTS

A dissertation submitted in partial satisfaction of the requirements
for the degree Doctor of Philosophy

in

Mechanical Engineering

by

Soheil Fatehiboroujeni

Committee in charge:
Professor Sachin Goyal, Chair
Professor Ashlie Martini
Professor Ajay Gopinathan
Professor Noemi Petra
Professor Arvind Gopinath

2018

The dissertation of Soheil Fatehiboroujeni is approved:

Sachin Goyal, Chair	Date
Ashlie Martini	Date
Arvind Gopinath	Date
Noemi Petra	Date
Ajay Gopinathan	Date

University of California, Merced

To my parents for all their sacrifices, and my wife for her blissful comradeship.

TABLE OF CONTENTS

LIST OF FIGURES

LIST OF TABLES

ABSTRACT

Slender structures–bodies with large length to thickness ratio–occur not only in structural engineering applications, but also in several biological and nano-scale applications. Some of the recently emerging examples of interest include nanoscale biological filaments (e.g. DNA molecules, microtubules, cilia and flagella), carbon nano-tubes and silver nano-wires. Several of these slender structures undergo very large twisting and bending deformations. For example, biological filaments such as DNA perform their biological functions via well-regulated structural deformations that involve large twisting and bending.

Continuum mechanics based models of slender structures are effective in simulating the mechanics of nano-scale filaments. However, the accuracy of these simulations strictly depends on the knowledge of the constitutive laws that may in general be nonlinear and non-homogeneous. It necessitates an inverse problem framework that can leverage the data provided by physical experiments and molecular dynamics simulations to estimate the unknown parameters in the constitutive law.

The primary purpose of this research is to show the possibility of developing inverse methods for identification of constitutive laws of slender structures modeled as continuum rods. The overarching goal of this research was originally motivated by the query into structure-function relationship of biological filaments; how these two features of the constitutive law (nonlinearity and non-homogeneity) influence structural deformations of biological filaments that in turn govern their biological activity or functions. However, little is known even from the perspective of structural engineering that could serve this overarching goal. Therefore, I defined mechanics problems that address and focus on some engineering and mathematical challenges as a stepping stone towards the overarching goal. This research in a broad outlook makes a bipartite contribution. The first contribution is the development of a computational rod model that captures large dynamic bending and torsion of slender filaments with user-defined nonlinear constitutive laws. The second contribution is the development of both deterministic and statistical inverse methods to identify the uncertain parameters of the constitutive law of slender structures.

Finally, the forward rod model developed here offers a platform to study a variety of interesting engineering problems. Therefore, as an additional contribution of this dissertation, I studied the beating oscillations of buckled rods subjected to nonconservative follower loads. This is motivated by the beating dynamics of active filaments and paves the way towards designing biomimetic applications of active filaments.

Chapter 1

INTRODUCTION

The primary purpose of my doctoral research is to show the possibility of developing inverse methods for identification of constitutive laws of slender structures modeled as continuum beams or rods. I particularly focused on cases where the unknown constitutive law could either be nonlinear or non-homogeneous without any a priori knowledge of it. The overarching goal of this research was originally motivated by the query into the structure-function relationship of biological filaments; how these two features of the constitutive law (nonlinearity and non-homogeneity) influence structural deformations of biological filaments that in turn govern their biological activity or functions. However, my dissertation does not directly address such applications. Instead, I recognize that little is known even from the perspective of structural engineering toward this overarching goal. Therefore, I defined mechanics problems that address and focus on some engineering and mathematical challenges as a stepping stone towards the overarching goal.

As a prerequisite to the inverse approaches I needed to reinvent a forward computational rod model based on existing rod theories and models. One of the novel contributions that I made to the computational rod model was to add a capability to input any arbitrary nonlinear constitutive law. The second major contribution of my dissertation is the development of both deterministic and statistical inverse approaches to identify the uncertain parameters of the constitutive law of slender structures. Finally, the forward rod model that I developed offers a platform to study a variety of interesting engineering problems. Therefore, as an additional contribution of my dissertation, I studied the beating oscillations of buckled rods subjected to nonconservative follower loads. This is motivated by the beating dynamics of active filaments and paves the way towards designing biomimetic applications of active filaments.

The following sections in this chapter seek to contextualize and clarify these contributions. Examples of research application that motivate this research are introduced and finally a summary of research contributions is presented.

1.1 Motivating Research Applications

It is known that bending and twisting deformations of biological filaments such as DNA, microtubules, flagella, cilia, and sheath proteins play a central role in their biological functions. For example, looping of DNA often mediated by protein binding, shown in Figure 1.1(a), left, is a crucial step in many gene regulatory processes [1, 2]. Another

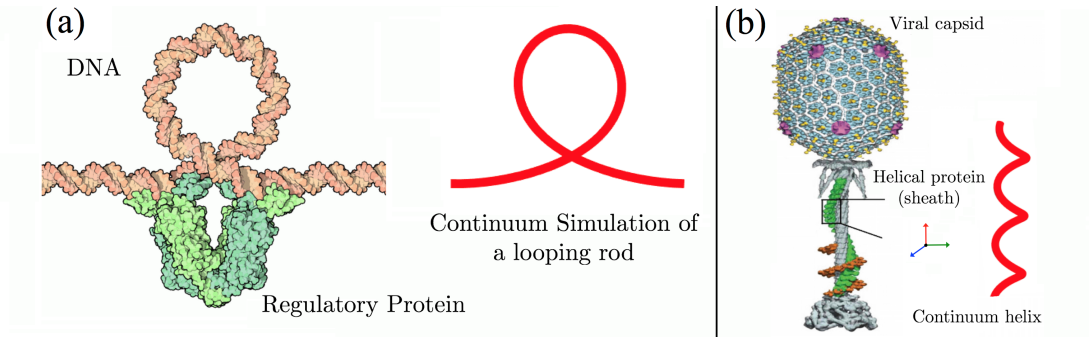

Figure 1.1: (a) DNA looping (left) regulates gene expression (pdb101.rcsb.org). Continuum simulation of a looping rod (right). (b) Viral injection mechanism (left) in which elastic energy of helical sheath proteins plays a central role. Continuum simulation of a helical rod (right).

example is the viral injection mechanism, shown in Figure 1.1(b) left, in which elastic energy of helical sheath proteins plays a central role in injecting the viral DNA into the host cell [3,4]. Both examples elucidate how understanding structural mechanics of biological filaments provides an essential perspective for medical research and drug discovery.

Another example of a motivating research problem is buckling of microtubules. Microtubules that are important components of cytoskeletal structures, in conjunction with actin and intermediate filaments provide both the static and dynamic framework that maintains cell structure. The morphology of cytoskeleton is known to regulate the intercellular transport of material [5] which is critical for proper cellular function. Microtubules resist various internal/external forces to maintain cell shape and they support motor proteins to generate the force required for cell movement and changes in shape [6–9]. Figure 1.2 adopted from Bicek *et al* [10] is showing actin-myosin contractility which is one of the many possible mechanisms that causes buckling of the microtubules. One of the important steps toward understanding such mechanics is to develop appropriate modeling techniques that are described in the following section.

1.2 Required Modeling Capabilities

The continuum mechanics based elastic rod models [11,12] have evolved as viable tools to efficiently simulate the bending and twisting deformations of a variety of slender structures. Slender structures occur not only in structural engineering applications, but also in the type of biological and nano-scale applications described above. Some of the recently emerging applications involving slender structures at nano-scale include biological filaments [13–15] (e.g. DNA molecules [2, 16, 17], microtubules [7, 8], cila

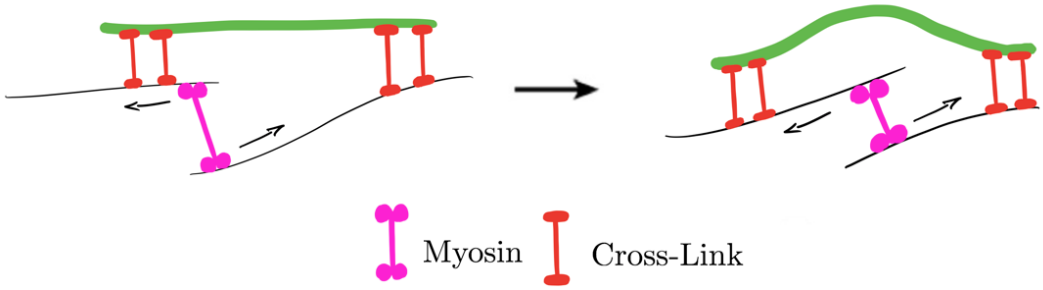

Figure 1.2: Actin-myosin contractility can cause a microtubule to buckle. Myosin which is an actin-based motor, can contract anti-parallel actin filaments as it moves. As a result, a microtubule that is attached to the actin will buckle.

and flagella [18] and several others [19–21]), carbon nano-tubes [22] and silver nanowires [23]. Several of these slender structures undergo very large twisting and bending deformations. For example, biological filaments such as DNA perform their biological functions via well-regulated structural deformations that involve large twisting and bending deformations [24] (Figure 1.1(a) left). Computational rod models are capable of simulating the nonlinear dynamics of such deformations (Figure 1.1(a,b) right) by employing appropriate constitutive laws in bending and torsion [25, 26], including intertwining with self-contact [27] and fluid-structure interaction. Yet, highly limited knowledge of the constitutive laws of biological filaments and nanorods has been a major roadblock for applicability of continuum rod models.

A continuum rod model, in general, consists of dynamic equilibrium equations and compatibility equations, which need to be solved respecting the prescribed constitutive law. Although dynamic equilibrium equations and compatibility conditions, which I henceforth refer to as the *rod model*, remain the same for all slender structures, the key distinguishing factor is the constitutive law. Traditional models assume linear homogenous constitutive laws in bending and torsion. However, nonlinearities and non-homogeneities in the constitutive law strongly influence the dynamics of such large deformations. For example, both DNA [28, 29] and microtubules [30, 31] are known to kink suggesting that these filaments must have non-convex stored energy functions [32]. The material nonlinearities are also known to influence the onset of buckling of nanorods and nanotubes [33, 34] as well as the post-bucking behavior [35]. Such details of buckling dynamics of filaments play an important role in biological systems [36]. Moroever, it is intuitive, and is also well recognized in continuum mechanics that the constitutive law of a material depends on its atomistic-level structure and interactions. Atomistic-level structure and interactions may in general vary along the length of biological filaments

leading to non-homogenous constitutive law. In case of DNA, while it is a readily accepted dogma that the genetic code resides in the chemical sequence of its four different types of monomer units, the base pairs, only recently it has been recognized that there is a second layer of coding in that sequence, that directly influences the mechanical behavior by varying the constitutive law of the filament along its length [37]. While physicists are already giving increasing attention to the subtle importance of mechanical layer of coding in DNA [37, 38], the need for understanding of how atomistic-level details affect the mechanics of thin filaments in general, opens the doors for a profound fundamental research in the field of mechanics of slender structures.

Unfortunately, for nano-scale filaments direct measurements of the parameters in the constitutive law are not feasible through laboratory experiments. For example, atomic force microscopy is used to find elastic moduli of silver nano-wires [23]. Single-molecule experiments that use optical and magnetic tweezers to prescribe or measure the dynamics of microscopic beads attached to one or both ends of DNA [39, 40] or microtubules [6] provide indirect estimates of their bending or torsional stiffness averaged over the entire length [41–43]. Direct imaging and thermal fluctuations also provide some data to estimate bending stiffness of microtubules and actin filaments [44, 45]. However, to detect the non-homogeneity along the length, the experiments are yet to evolve further accounting for the challenge that the current technology does not allow direct observation of nano-scale filaments in motion with sufficient resolution [46].

Accurate identification of constitutive law parameters that are not directly measurable involve challenging inverse methods. While a computational forward model can simulate and predict deformations given initial and boundary conditions as well as parameters defining the constitute law, inverse models seek to identify unknown parameters of the constitutive law given some measurements of deformations by leveraging the other known components of the forward model (such as the equilibrium and compatibility equations). However, in developing inverse methods, a review of which can be found here [47, 48], the need first arises for a computational forward model that can efficiently simulate the deformations with any *user-defined* nonlinear constitutive law. Therefore, the inverse models for nonlinear constitutive laws have to evolve together with the development of corresponding forward models.

1.3 Research Challenges and Thesis Objectives

Previous sections identify a knowledge gap that has been the subject of interest to a large research community and can be summarized as the following research question: how can the constitutive law of filaments be identified from physical measurements and/or molecular dynamics simulations? Answering this question involves a number of challenges. First, an inverse approach to identify the constitutive law of filaments based on measurement data has to cope with the inherent ill-posedness of the inverse problems [49, 50]. Ill-posedness is a typical feature of many inverse problems, in which the

data do not uniquely determine the inversion parameter(s). Second, in physical experiments it is not often possible to measure the observable quantity, in our case deformations, everywhere in the domain. So, a compelling inverse approach not only returns a solution to the inverse problem, but also need to determine the faith–to quantify the uncertainty–in the inversion results systematically. And third, any measurement data includes some level of noise, hence robustness is a critical feature of any viable inverse approach.

So, on one hand physicists are developing futuristic techniques of super-resolution imaging to collect more and more informative data [46, 51]. On the other hand, as a mechanician, *I defined the main objective of my research as to explore the possibilities of developing inverse methods for identification of constitute law of slender structures.* For this objective, instead of using actual measured data specific to any research application described in Section 1.1, it is more useful, and suffices, to use synthetic data tailored to addressing specific challenges in developing inverse methods. Synthetic data is generated by forward models and provides us with the necessary control for addressing the issues of reconstructability (invertability), robustness, and data sparsity, one at a time. *Development of a computational rod model (a forward rod model) that is capable of incorporating user-defined constitutive laws is an associated objective of this research.*

Another knowledge gap in the field of mechanics is how the nonlonearity in constitutive law influences the deformations of slender structures. Recognizing that the post-buckling dynamics is crucial to several biological filaments, *I defined another main objective of my research as to analyze the effect of nonlinearities in the constitutive law on mechanics of slender structures, in particular, their post-buckling stability region.* This research objective, by focusing on a specific problem, exhibits the sensitivity of the mechanical response (or post-buckling stability) of slender structures to nonlinearities in their constitutive law. This in turn, indicates the significance of having accurate knowledge of the constitutive law for accurate modeling.

Finally, forward rod model offers a highly versatile tool to investigate several scientific questions related to how a variety of filaments in nature function. However, modeling and simulating the dynamics of deformation with a computational rod model is a known challenge in the mechanics community. So, I defined an additional research objective that shows the potential impact of the computational tools developed in this research. The computational rod model which uses a *linear* constitutive law is not by itself a novel contribution of this work, but is reinvented here building upon existing theories. *The additional research objective that I defined is to use this model to investigate if and how follower forces in pre-stressed clamped rods mimic oscillatory beating of active filaments.* Flagella and cilia are examples of actively oscillating, whiplike biological filaments that are crucial to processes as diverse as locomotion, mucus clearance, embryogenesis and cell motility. Elastically driven rod-like filaments subjected to compressive follower forces provide a synthetic way to mimic such oscillatory beating.

The following list summarizes the objectives of my dissertation described above.

1. To explore the possibilities of developing inverse methods for identification of constitute law of slender structures.

2. To develop a computational rod model (a forward rod model) that is capable of incorporating user-defined constitutive laws.

3. To analyze the effect of nonlinearities in the constitutive law on the mechanics of slender structures, in particular, their post-buckling stability region.

4. To investigate if and how follower forces in pre-stressed clamped rods mimic oscillatory beating of active filaments.

These research objectives provide stepping stones towards addressing broader research challenges. By developing modeling tools and elucidating a number of novel findings this dissertation opens the way for a wider range of queries and developments that would have not been possible without the basic contributions of this thesis.

1.4 Summary of Research Contributions

Here, I summarize my research contributions in the order they appear in Chapters 2 to 6.

- Effect of Softening Nonlinearities of Constitutive Law on Buckling

For a class of materials which exhibit cubic nonlinearity in the constitutive law, the condition for post-buckling stability is characterized in literature using perturbation analysis [52, 53]. Previous work reports that there is a limit on cubic parameter in the constitutive law, beyond which the post-buckling configuration transitions from stable to unstable. In Chapter 2, I showed that there is a regime of partially stable post-buckling solutions which are not predicted by any of the previous work. By perturbation analysis I derived the domain of partial stability in the post-buckling response of clamped-free beam for softening constitutive laws. Thus, I quantitatively showed how initially stable post-buckling solutions transition to unstable post-buckling solutions as buckling continues. Post-buckling instability results into catastrophic collapse of the structure unless the external or body forces vanish immediately.

- A Computational Rod Model with User-Defined Nonlinear Constitutive Law

In Chapter 3, I contributed an efficient formulation of a computational rod model that has the capability of incorporating constitutive laws with any nonlinear functional form defined by the user. Jacobian-based computational rod models require users to change the Jacobian if the functional form of the constitutive law is changed, and hence are not user-friendly. Chapter 3 presents a scheme that automatically modifies the Jacobian based on any user-defined constitutive law without requiring symbolic differentiation.

While the same purpose could be achieved by "automatic differentiation" (also known as algorithmic differentiation or AD), the scheme that I developed is much simpler to implement, yet as efficient. The scheme is then used to simulate force-extension behavior of a coiled spring with a softening constitutive law. This case study is motivated by mechanism of genomic delivery from virus to its host cell that is driven by elastic energy stored in a compressed helical (sheath) protein [3].

- An Inverse Approach Directly Based on Forward Rod Model for Nonlinear Constitutive Laws

Chapter 4 presents an inverse approach based on a continuum rod model to identify nonlinear constitutive laws of slender structures from geometric data. This approach can use data from the dynamic states of deformation obtained, in principle, from atomistic simulations or other sources, however throughout this chapter I synthesize deformation data using the computational rod model. Depending on the kinematic quantities that may be computed from the observation or measured data, the algorithm of inverse approaches differ in their steps to estimate the internal moments and forces. I also investigated and compared the robustness of these inverse algorithms accounting for the effect of noise in the data. Overall in this chapter, for the first time, I showed a viable approach of developing an inverse rod model which can be further extended to specific applications.

- An Adjoint-Based Inverse Approach for Non-homogeneous Constitutive Laws

Chapter 5 contributes an inverse approach for identification of the non-homogeneous constitutive laws of slender structures in a linear elastic model. In doing so, I made two levels of contributions that are described below:

- Fast and Scalable Deterministic Approach with Regularization

I formulated a simple but representative inverse problem governed by the linear elastic equation (Navier-Lamé model of linear elasticity) with non-homogeneous constitutive law. Here, the inverse problem is a nonlinear least-squares optimization in which the cost functional is the misfit between synthetic observations of a cantilever displacement field and model predictions. A Tikhonov regularization term is added to the cost functional to render the problem well-posed and account for observational error. I solve this optimization problem with an adjoint-based inexact Newton-conjugate gradient method. I showed that the reconstruction of the Lamé parameter field converges to the exact coefficient as the observation error decreases. I also showed that the number of Newton iterations is insensitive to the dimension of the parameters, i.e., the computational cost of solving the inverse problem measured in number of PDE (Partial Differential Equations) solves is constant as the size of the problem is increased. Therefore, this computationally fast and scalable framework has the potential to solve high-dimensional inverse elasticity problems that are of practical interest.

- Uncertainty Quantification Using Bayesian Inference

I also formulated the inverse problem of identifying Young's modulus field from noisy synthetic observations of the displacement field implementing a Bayesian inference framework. Computing the general solution of this inverse problem (i.e., the posterior probability density) can become prohibitive, due to the expense of solving the forward model and the high dimensionality of the uncertain parameters (which are discretizations of the Young's modulus field). To cope with the infinite-dimensional (i.e., large-scale) character of the parameter field, it is common to construct a Gaussian approximation to the posterior at the maximum a posteriori probability (MAP) point [54]. The MAP point in the Gaussian case coincides with the mean and it is given by the solution of the deterministic inverse elasticity problem. Here, the mean is computed by minimizing a regularized misfit functional between observed and modeled displacement. The resulting least-squares minimization problem is solved using an adjoint-based inexact Newton method, which uses first and second derivative information. I apply this method to quantify uncertainties in the inference of the Young's modulus field from synthetic observations of both cantilever deformation and rod with a helical structure.

- Stability of Slender Structures Subjected to Follower Loads

Flagella and cilia are examples of actively oscillating, whiplike biological filaments that are crucial to processes as diverse as locomotion, mucus clearance, embryogenesis and cell motility. Elastically driven rod-like filaments subjected to compressive follower forces provide a synthetic way to mimic such oscillatory beating. In the continuum limit, this time-periodic, stable response results from the interplay between the structural instability of the inextensible slender rod, geometric constraints that control the onset of instability, energy pumped into the system by the active follower forces, and motion-driven viscous dissipation in ambient media.

In Chapter 6, I investigate the dynamical, nonlinear buckling instabilities that arise due to the action of nonconservative follower forces on a pre-stressed slender rod clamped at both ends. I systematically calculate the critical follower forces for onset of oscillations, the emergent frequencies and the spatiotemporal patterns of the nonlinear rod shapes that result for two types of fluid drag forces, namely, Stokes drag and Morrison drag. The minimum (critical) force required to initiate stable oscillations depends strongly on the initial slack and weakly on the nature of the drag force. The emergent frequencies at onset however depend strongly on both the extent of pre-stress as well as the nature of the fluid drag. Far from onset, and for large follower forces, the frequency of the oscillations is determined by a power balance between the energy input by the active forces and the dissipation due to fluid drag. Previous studies have focused on the buckling dynamics of free-free, fixed-free, and pinned-free filaments with the base state being a straight non-stressed filament or rod. Analyzing the role of pre-stress in emergent oscillations driven by active distributed follower forces is a novel contribution of this dissertation.

Chapter 2

EFFECT OF NONLINEAR CONSTITUTIVE LAW ON BUCKLING

2.1 Introduction

Buckling of slender structures under compressive loads has been the subject of the investigation for many engineering and biological systems. Buckling of microtubules and actin filaments are shown to have a fundamental impact on the cytoskeletal shape and contractility of the cells [10, 55, 56]. Microtubules are important components of cytoskeletal structure that in conjunction with actin and intermediate filaments provide both the static and dynamic framework to maintain the structure of the cell. Morphology of cytoskeleton is known to regulate the intercellular transport of material [5] which is critical for proper cellular function. Microtubules resist various internal/external forces to maintain cell shape and they support motor proteins to generate the force required for cell movement and changes in shape [6–9]. For microtubules the critical buckling load reported in the literature varies form around 1 pN, without taking into account the effect of the cytoplasm [57] and up to around 100 pN when the interaction of microtubules with the surrounding elastic filament network (cytoskeletal network) is considered [55,58]. Microtubules demonstrate short buckling wavelengths in vivo, however, they can attain highly buckled shapes (large amplitudes of buckling) [59]. For highly buckled microtubules it is suggested that [59] using a nonlinear model to capture the interaction of the microtubule with the surrounding elastic network, in combination with a non-Newtonian viscous fluid model is necessary to accurately characterize the buckling deformation since the linear models result in an underestimated buckling amplitude or overestimated critical load. On the same basis, it is reasonable to assume that due to the large rates of deformations that microtubules attain when buckled in vivo, the assumption of linear constitutive law in bending is a part of the model discrepancy that accounts for the mismatch of the current models such as [59] and the experimental observations. Therefore, I argue that an investigation on the effect of nonlinear constitutive law on post-buckling behavior of slender filaments, which is the subject of this chapter, has an implication for a better understanding of the buckling of biological filaments such as microtubules and actin filaments. In fact, nonlinear material properties are known to influence the onset of buckling for nanorods and nanotubes [33,34]. Existence of post-buckling solution for elastic rods with nonlinear constitutive law has been established in the continuum mechanics literature [60, 61].

Treatment of the post-buckling stability analysis for a class of materials such as redwood which exhibit cubic nonlinearity in the constitutive law

$$\sigma = E_1\varepsilon + E_2\varepsilon^3, \tag{2.1}$$

is presented in the literature [52,53]. Here E_1 and E_2 are constants, σ is normal stress and ε is normal strain. Although this cubic nonlinear constitutive law is originally proposed to capture softening nonlinearity of redwood it is very well fit to many other applications such as softening nonlinearity of Silicon nanowire [62]. For this particular form of nonlinear constitutive law, the condition of post-buckling stability is characterized using perturbation analysis [52] [53]. To summarize the results in the existing literature for this particular case we can say that for a given column with fixed slenderness ratio, as the coefficient E_2 decreases form zero in the negative direction (i.e. as the constitutive law becomes more and more softenning), there is a threshold on the negative scale after which the post-buckling solution is unstable. However, I demonstrated in this chapter that there is a regime of partially stable post-buckling solutions which are not predicted by previous work. Similar to Haslach [52], I used the perturbation method and by investigating the convergence of the solutions to higher order terms I derived the domain of partial stability in the post-buckling response of clamped-free beams. These initially stable post-buckling solutions transition to unstable post-buckling solutions as the buckling continues.

In the Section 2.2, I first demonstrate three stability regimes of post-buckling solutions that are stable, unstable, and partially stable using an idealized model of rigid bar and rotational spring. Next, in Section 2.3, I present the analytical solution for the buckling of a continuous fixed-free column using perturbation analysis. In Section 2.4, I present some illustrative results to visualize the three post-buckling stability regimes. Finally, in Section 2.5, I discuss the overall findings of this chapter and scope of the future work.

2.2 Idealized Model

The idealized model represents the elastic column with a combination of a rigid bar and a rotational spring. The stability of the structure can be examined using this simple model as shown in Figure 2.1. Consider a rigid bar with length L connected to a pin joint and a rotational spring that captures the restoring bending moment M_R following the law given in Eq. (2.2).

$$M_R = k_1\theta + k_2\theta^3 \tag{2.2}$$

The angle θ represents the deflection of the beam from initial direction and the k_1 and k_2 are constant parameters. To exclude the cases with negative stiffness around $\theta = 0$, the parameter k_1 requires to be nonnegative. Consequently, the positive k_2 values correspond to hardening constitutive laws, $k_2 = 0$ represents a linear constitutive law, and negative k_2 value correspond to softening constitutive laws.

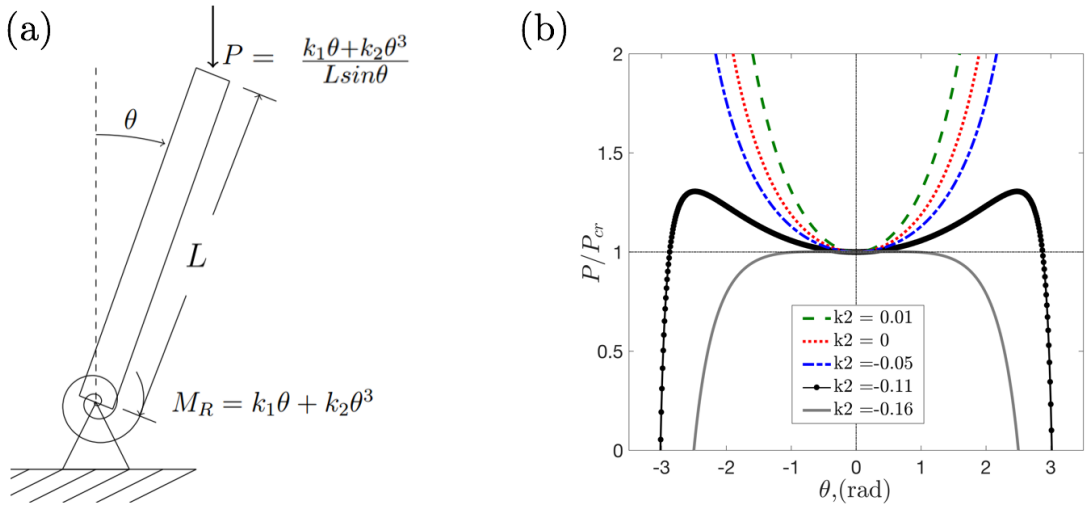

Figure 2.1: (a) Idealized model of buckling of a clamped-free column where $k_1 = 1$ Nm/rad, $L = 1$ m. (b) This buckling bifurcation diagram shows that as k_2 (in units of Nm/rad^3) decreases, the stable buckling (dashed curves with green, red, or blue colors) transitions to a partially stable buckling (black curve with circular markers) and finally to unstable buckling (gray solid curve).

Equilibrium of the moments for the column about the pin joint is shown in Eq. (2.3). Here, the direction of the compressive load, P is preserved along the initial direction of the column's axis. This equation can be rearranged to find an expression for the buckling load, P as a function of deflection, θ which is given in Eq. (2.4).

$$k_1\theta + k_2\theta^3 - PL\sin\theta = 0 \tag{2.3}$$

$$P = \frac{k_1\theta + k_2\theta^3}{L\sin\theta} \tag{2.4}$$

The buckling critical load P_{cr} can be found by taking the limit of the Eq. (2.4) as θ goes to zero which leads to

$$P_{cr} = \frac{k_1}{L}. \tag{2.5}$$

Figure 2.1 is showing the plots of the load P normalized by P_{cr} versus the deflection θ for three different possible types of spring laws. It can be seen that for $k_2 = 0$ we have a linear system which its buckling stability reflects what was famously demonstrated by Euler. For positive values of k_2 we are observing stable post-buckling similar to the linear case. This means as the angle, θ increases, the required load to hold the structure in equilibrium also increases. However, as the value of k_2 decreases from zero, the effect of nonlinear softening at some point becomes significant and we observe a partially stable post-buckling. In this regime, the buckled column is initially stable but after a critical

value of the deflection the required load, P to hold the structure in equilibrium decreases as the deflection, θ increases. Finally, we observe a range for parameter k_2 for which the post-buckling response of the beam is completely unstable. This simple analysis and its findings call for a detailed analysis of the post-buckling stability of columns with softening constitutive law of cubic form using a continuum description of the beam, which is discussed in next section.

2.3 Perturbation Analysis

Since the idealized model revealed catastrophic post-buckling instabilities due to softening nonlinearity of the constitutive law, I investigated this problem in more detail using a continuum beam theory. Perturbation analysis is used, similar to Haslach [52], to find the buckling response of a cantilever beam under a compressive force. A schematic diagram of this loading scenario is shown in Figure 2.2. In this method, the external load, P and the deflection of the beam, $w(s)$ are expanded in terms of a perturbation parameter, b.

$$w(s) = w_1(s)b + w_2(s)b^2 + w_3(s)b^3 + ... \tag{2.6}$$

$$P = P_{cr} + P_{(1)}b + P_{(2)}b^2 + P_{(3)}b^3 + ... \tag{2.7}$$

Next, the variations of the potential energy of the system with respect to the deflection function, $w(s)$ is calculated as we will present and discuss in this section. This allows us to derive infinite number of differential equations that are solvable for the $w_i(s)$'s and the $P_{(i)}$'s.

We consider a beam with the cubic nonlinear constitutive law

$$\sigma = E_1\varepsilon + E_2\varepsilon^3 \tag{2.8}$$

where E_1, E_2 are constants, σ is the normal stress and ε is the strain. For a beam under bending, the normal strain on the cross-section of the beam for a material point at distance, ν from the bending neutral axis can be written as follows.

$$\varepsilon = -\nu\kappa = -\nu\frac{d\theta}{ds} \tag{2.9}$$

In Eq. (2.9), κ is denoting the bending curvature which is equal to the rate of change of the orientation θ with respect to the arc length variable s. Using this relationship the constitutive law is integrated over the cross section to find an expression relating the bending curvature to the restoring moment.

$$M = -\int_A \sigma\nu dA = E_1I_1\kappa + E_2I_2\kappa^3 \tag{2.10}$$

In Eq. (2.10) M is representing the restoring bending moment and I_1 and I_2 are given

below.

$$I_1 = \int_A \nu^2 dA \tag{2.11}$$

$$I_2 = \int_A \nu^4 dA \tag{2.12}$$

The curvature can be expressed in terms of the deflection function and its derivatives along s. For this I need to find the first and second derivative of deflection function with respect to s which I here denote by w' and w'', respectively.

$$w' = \frac{dw(s)}{ds} = sin(\theta) \tag{2.13}$$

$$w'' = \frac{dw'}{ds} = cos(\theta)\frac{d\theta}{ds} = -cos(\theta)\kappa \tag{2.14}$$

Thus, by combining Eqs. (2.9), (2.13), and (2.14) we can rewrite the curvature, κ as follows.

$$\kappa^2 = \frac{w''^2}{1-w'^2} \tag{2.15}$$

Now we have all the ingredients to represent the potential energy of the system in terms of $w(s)$ and P. The potential energy has two terms. First, the bending strain energy and second, the work done by the external force. Therefore the potential energy, V can be written as

$$V = \int_0^L \big(\int M d\kappa \big) ds - P\Delta, \tag{2.16}$$

where

$$\Delta = \int_0^L (1 - cos(\theta)) ds = \int_0^L (1 - \sqrt{(1-w'^2)}) ds, \tag{2.17}$$

or alternatively, by using Eqs. (2.15) and (2.17)

$$\begin{aligned} V = \int_0^L \big(\frac{1}{2} E_1 I_1 \frac{w''^2}{(1-w'^2)} + \frac{1}{4} E_2 I_2 \frac{w''^4}{(1-w'^2)^2} \big) ds - \\ P \int_0^L (1 - \sqrt{(1-w'^2)}) ds. \end{aligned} \tag{2.18}$$

The derivative of this energy function with respect to $w(s)$ is calculated as follows.

$$\begin{aligned} E_1 I_1 [w''''(1-w'^2)^{-1} + 4w'w''w'''(1-w'^2)^{-2} + \\ w''^3(1+3w'^2)(1-w'^2)^{-3}] + E_2 I_2 [3w''''w''^2(1-w'^2)^{-2} + \\ 6w'''^2 w''(1-w'^2)^{-2} + 24w'''w''^3(1-w'^2)^{-3} + \\ 3w''^5(1+5w'^2)(1-w'^2)^{-4}] + Pw''(1-w'^2)^{-3/2} = 0 \end{aligned} \tag{2.19}$$

Substituting polynomial expansions of Eqs. (2.6) and (2.7) in Eq. () results into a polynomial equation in terms of powers of b. By equating the coefficients of all powers of b to zero we can find infinite number of differential equations that are solvable for w_i's and $P_{(i)}$'s subjected to sufficient boundary condition. Differential equations that are found by collecting the coefficients of b from both sides of the Eq. (2.3) is given below. The first equation is a linear homogeneous fourth order differential equation.

$$E_1 I_1 {w_1}^{(4)}(s) + P_{\text{cr}} w_1''(s) = 0 \tag{2.20}$$

The rest of the equations, found by collecting the coefficients of b^i, are linear non-homogeneous fourth order differential equation which can be written as

$$E_1 I_1 {w_i}^{(4)}(s) + P_{\text{cr}} w_i''(s) = R_i, \text{ for } i = 2,3,4,... \tag{2.21}$$

where R_i consolidates all non-homogenous terms that depend on the solution of equations $i-1$, $i-2$, $i-3$, etc. To solve each of these fourth order differential equations four boundary conditions are required. For the buckling of a cantilever beam under compressive force three boundary conditions can be summarized as follows.

$$w(0) = w'(0) = w''(L) = 0 \tag{2.22}$$

The fourth boundary condition is defined by prescribing the deflection of the beam at the free end to be equal to the perturbation parameter.

$$w(L) = -b \tag{2.23}$$

In addition, to solve for the unknown terms of the load function, $P_{(i)}$'s another boundary condition is required. The relation between the restoring moment and curvature at the fixed end is used to find the fifth boundary condition. The restoring moment at $s = 0$ is found using Newton's second law while the weight of the beam is neglected.

$$M(0) = -Pb \tag{2.24}$$

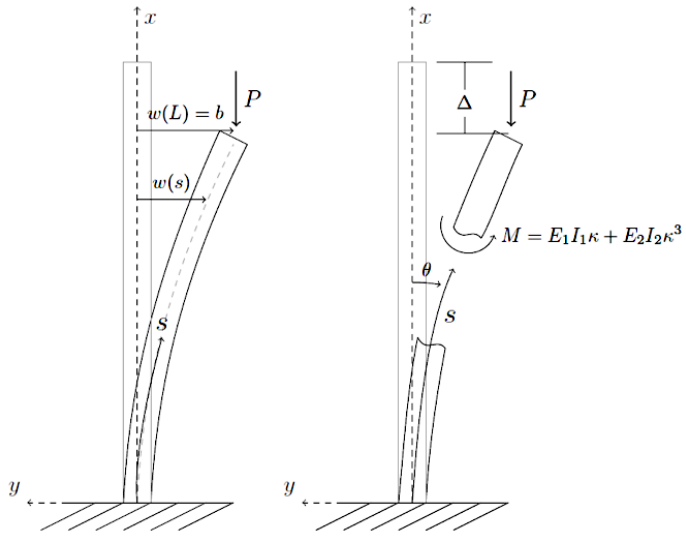

Figure 2.2: Schematic diagram of the buckling of a cantilever beam under compressive force.

Using the fact that $w'(0) = 0$, curvature at $s = 0$ is reduced to

$$\kappa(0) = w''(0). \tag{2.25}$$

Now using the constitutive law we can find the fifth necessary boundary condition to solve the problem.

$$-Pb = E_1 I_1 w''(0) + E_2 I_2 w''(0)^3 \tag{2.26}$$

The boundary condition expressed in Eqs. (2.22), (2.23), and (2.26) can be translated in terms of $w_i(s)$'s as shown in the following.

$$w_i(0) = w_i'(0) = w_i''(L) = 0 \tag{2.27}$$

$$\begin{aligned} w_1(L) &= -1, \quad \text{and} \\ w_i(L) &= 0, \quad \text{for } i \neq 1. \end{aligned} \tag{2.28}$$

The fifth boundary condition, Eq. (2.26), can be rewritten in terms of $P_{(i)}$ by collecting

the coefficients of b^i.

$$\begin{aligned}
-P_{cr} =& E_1 I_1 w_1''(0) \\
-P_{(1)} =& E_1 I_1 w_2''(0) \\
-P_{(2)} =& E_1 I_1 w_3''(0) + 3E_2 I_2 w_3''(0)^3 \\
-P_{(3)} =& 3E_2 I_2 w_2''(0) w_1''(0)^2 + E_2 I_2 w_4''(0) \\
-P_{(4)} =& 3E_2 I_2 w_3''(0) w_1''(0)^2 + 3E_2 I_2 w_2''(0)^2 w_1''(0) + E_2 I_2 w_5''(0) \\
& \text{etc.}
\end{aligned} \tag{2.29}$$

In the next section, a systematic way to derive analytical solutions of these fourth order differential equations using Mathematica is discussed.

2.4 Results

Using five boundary conditions that discussed in previous section the differential equations are solved systematically in Mathematica for both the deflection function, w_i and the load, $P_{(i)}$. A complete description of the solution terms for the load, P up to 14-th order is given in Appendix A, in addition to the Mathematica script. Here, the solution corresponding to the 1-st up to 6-th order of accuracy is presented.

$$\begin{aligned}
P_{cr} =& \frac{\pi^2 E_1 I_1}{4L^2} \\
w_1 =& \cos\left(\frac{\pi s}{2L}\right) - 1
\end{aligned} \tag{2.30}$$

$$P_{(1)} = w_2 = 0 \tag{2.31}$$

$$\begin{aligned}
P_{(2)} =& \frac{2\pi^4 E_1 I_1 L^2 + 3\pi^6 E_2 I_2}{256 L^6} \\
w_3 =& 2\sin\left(\frac{\pi s}{2L}\right)\sin\left(\frac{\pi s}{L}\right)
\end{aligned} \tag{2.32}$$

$$P_{(3)} = w_4 = 0 \tag{2.33}$$

$$\begin{aligned}
P_{(4)} =& \frac{\pi^6 (76 E_1 I_1^2 L^4 + 148\pi^2 E_1 I_1 E_2 I_2 L^2 - 21\pi^4 E_2 I_2^2)}{131072 L^{10} E_1 I_1} \\
w_5 =& -\left(\pi^4 \sin^2\left(\frac{\pi s}{2L}\right)\cos\left(\frac{\pi s}{2L}\right)(68 E_1 I_1^2 L^4 + 2\left(2E_1 I_1 L^2 - 3\pi^2 \mathrm{EI}_2\right)^2 \cos\left(\frac{\pi s}{L}\right) \right. \\
& \left. -20\pi^2 E_1 I_1 \mathrm{EI}_2 L^2 + 57\pi^4 \mathrm{EI}_2^2)\right)/(65536 E_1 I_1^2 L^8)
\end{aligned} \tag{2.34}$$

$$P_{(5)} = w_6 = 0 \tag{2.35}$$

Following the similar pattern, the solution to all even numbered differential equations are zero which means all of the even numbered terms in the deflection function (w_2, w_4, w_6, etc.) and all the odd numbered terms in the load ($P_{(1)}$, $P_{(2)}$, $P_{(3)}$, etc.) are zero. In previous work [52] the solution was truncated after solving the third differential equation which gives a 4-th order approximation, $O(b^4)$ of the load, P.

$$P(b) = \frac{\pi^2 E_1 I_1}{4L^2} + (\frac{2\pi^4 E_1 I_1 L^2 + 3\pi^6 E_2 I_2}{256 L^6})b^2 + O(b^4) \tag{2.36}$$

By determining the sign of the coefficient of the b^2, Haslach [52] reported the condition for the post-buckling stability to be $E_1 I_1 (\frac{2L}{\pi})^2 \frac{1}{6I_2} < -E_2$ or equivalently

$$(E_2 I_2)_{cr} = -\frac{E_1 I_1}{6}(\frac{2L}{\pi})^2, \tag{2.37}$$

and as a result for any $E_2 I_2 > (E_2 I_2)_{cr}$ considered the post-buckling shapes stable. However, in what follows I demonstrate how this truncation is causing a salient feature of the post-buckling stability to be missed. The results presented in this section indicate that to capture a post-buckling regime with partial stability, the solution needs to be calculated at least with 6-th order accuracy. Furthermore, employing a systematic truncation criteria, such as the convergence of the solution which is used in this section, enhances the accuracy of predictions for the stable post-buckling regime and prevents the over estimation of stability range. The load function, P with 6-th order accuracy is represented in Eq. (2.38).

$$\begin{aligned} P(b) =& \frac{\pi^2 E_1 I_1}{4L^2} + (\frac{2\pi^4 E_1 I_1 L^2 + 3\pi^6 E_2 I_2}{256 L^6})b^2 \\ &+ (\frac{\pi^6 (76 E_1 I_1^2 L^4 + 148\pi^2 E_1 I_1 E_2 I_2 L^2 - 21\pi^4 E_2 I_2^2)}{131072 L^{10} E_1 I_1})b^4 + O(b^6) \end{aligned} \tag{2.38}$$

Using the Wolfram Mathematica [63] I have automated the derivation of analytical solutions to this perturbation problem. A script to perform the analysis is included in Appendix A. Here, I first demonstrate the convergence of solution by choosing a set of parameters for the column properties. I assume the length $L = 1$, coefficient $E_1 I_1 = \frac{4}{\pi^2}$, and $E_2 I_2 = \frac{9}{10}(E_2 I_2)_{cr}$. Figure 2.3 shows that for the chosen set of parameters the 14-th order solution $O(b^{14})$ has enough accuracy in calculating the load, P as a function of deflection, b. It is important to note that here we chose to illustrate the convergence plot for a value of $E_2 I_2$ close to its critical value, since for very stiff beams ($E_2 I_2 \gg (E_2 I_2)_{cr}$) or very soft beams ($E_2 I_2 \ll (E_2 I_2)_{cr}$) the solution will converge faster in comparison to the cases where $E_2 I_2$ is close to critical value. Figure 2.3 also demonstrates an instance of a column with partially stable post-buckling which is only predictable by a solution, at least, of order 6, i.e., Eq. (2.38). In Figure 2.3 the solutions show negligible improvement by increasing the order of accuracy from 12 to 14, therefore, the solutions are considered

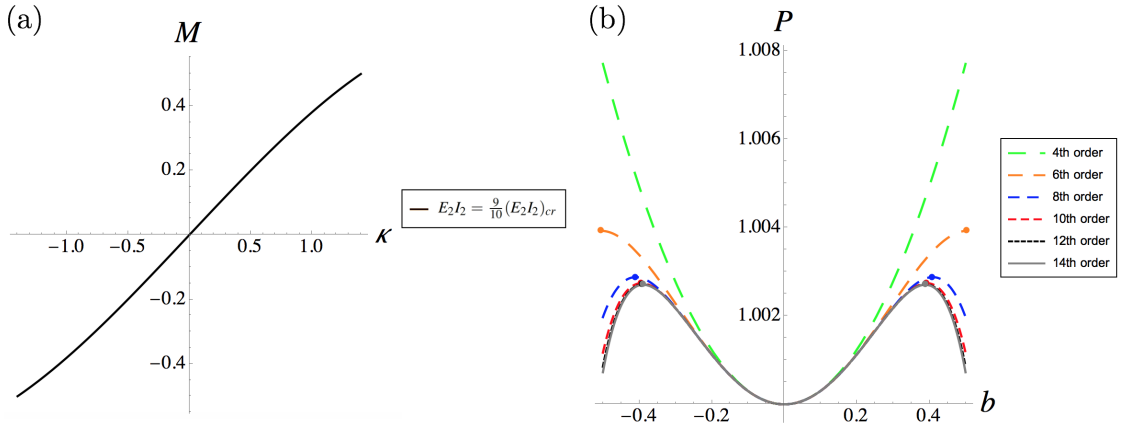

Figure 2.3: The external compressive load, P as a function of deflection, b for a column with the length $L = 1$, coefficient $E_1I_1 = \frac{4}{\pi^2}$, and $E_2I_2 = \frac{9}{10}(E_2I_2)_{cr}$. The curves show negligible improvement by moving from the order of accuracy $O(b^{12})$ to $O(b^{14})$, hence the solutions is considered to be converged at $O(b^{14})$.

to be converged at 14-th order.

Figure 2.4 illustrates four instances of load-deflection plots based on the results obtained by previous work, as well as the predictions by the analysis presented in this chapter. In part (a) of the Figure 2.4 the cubic coefficient is chosen to be zero, $E_2I_2 = 0$, which corresponds to a column with linear constitutive law. In this case the 14-th order solution provides only a slight improvement in estimation of the load and both methods estimate an stable post-buckling. The situation is similar in part (b) despite the fact that the this case represents a column with softening nonlinear constitutive law where $E_2I_2 = \frac{6}{10}(E_2I_2)_{cr}$. However, part (c) of the Figure 2.4 in which, $E_2I_2 = \frac{9}{10}(E_2I_2)_{cr}$, the load-deflection curve obtained by solutions of the order 6 and higher demonstrate a qualitatively different shape. I call this regime initially (or partially) stable post-buckling regime, since for a specific value of deflection, b the post-buckling response transitions from stable to unstable. And finally part (d) of the Figure 2.4 corresponds to an unstable post-buckling regime, $E_2I_2 = \frac{6}{5}(E_2I_2)_{cr}$, in which predictions by solutions of all orders are qualitatively the same. Figure 2.5 demonstrates the bending moment versus curvature diagrams for the the same instances that are showcased in Figure 2.4 to provide a visual representation of the softening nonlinearity in the constitutive law in various post-buckling regimes.

2.5 Discussion and Conclusions

Using an analysis with simple idealized model of the slender columns with the cubic nonlinearity in the constitutive law, it is observed that the post-buckling behavior of

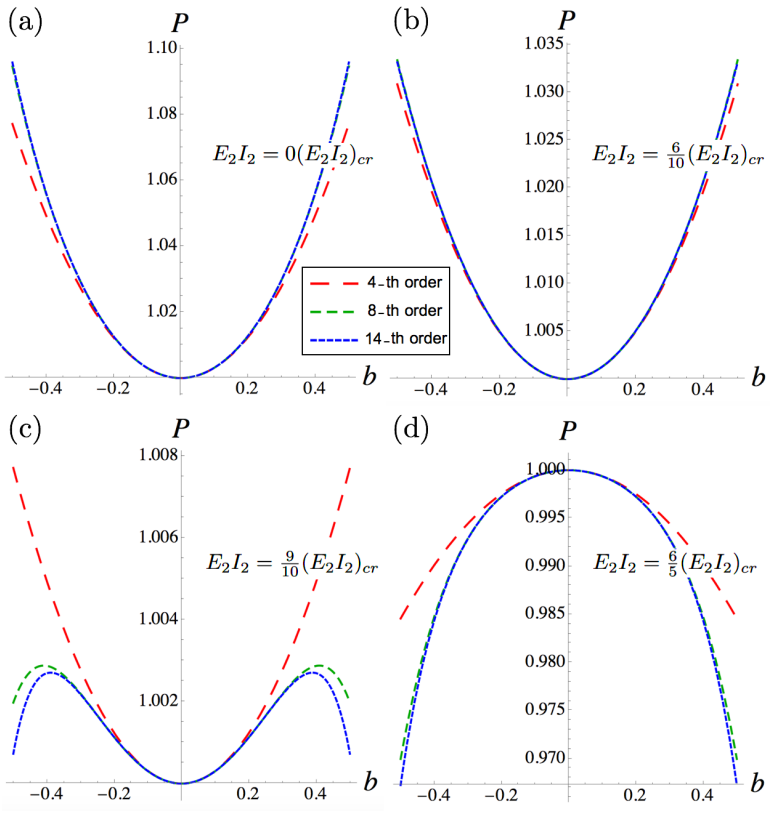

Figure 2.4: External compressive load is plotted against the deflection, obtained by perturbation analysis and corresponding to the solutions with 4-th, 8-th, and 14-th order of accuracy. Solutions with 6-th or higher order accuracy show that as E_2I_2 decreases from 0 (a) to below $(E_2I_2)_{cr}$, the column transitions through a partially stable buckling for $0 > E_2I_2 > (E_2I_2)_{cr}$, e.g., the transition from (b) to (c), and finally for $E_2I_2 \leqslant (E_2I_2)_{cr}$ the post-buckling becomes fully unstable. The 4-th order solution (red dashed curve) shows only an abrupt change from stable to unstable buckling at $(E_2I_2)_{cr}$.

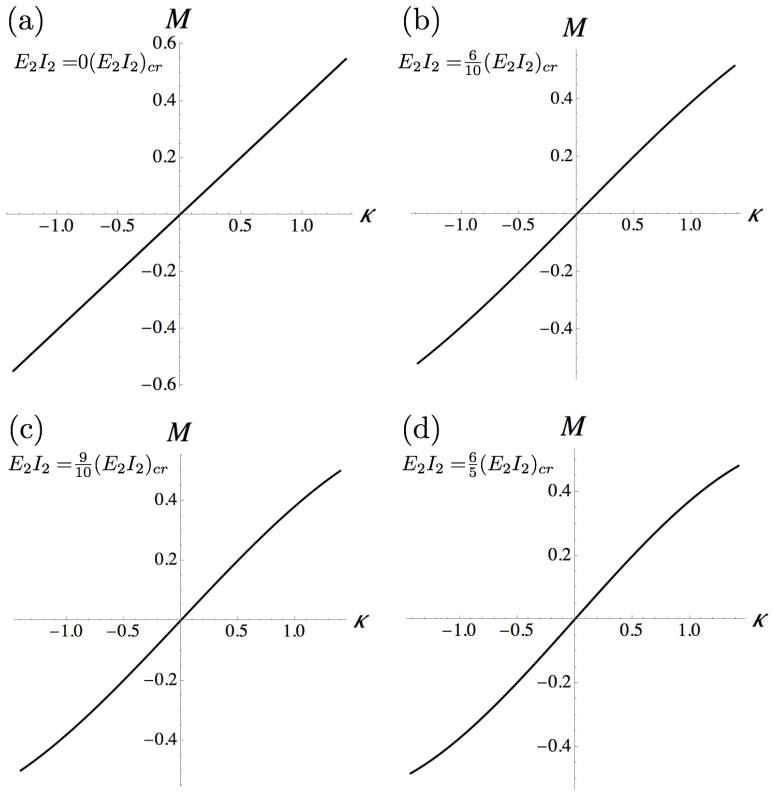

Figure 2.5: The bending moment versus curvature is depicted for each case of the load versus deflection shown in Figure 2.4. In all four cases (a, b, c, d) the constitute law is strictly monotonic.

columns does not abruptly change from being stable to being unstable as the cubic (softening) nonlinearity in the constitutive law is increased. Instead, the domain of stability diminishes smoothly. In other words, the post-buckling behavior is stable at the onset, but after at a critical value of the cubic coefficient, it becomes unstable and the column collapses catastrophically.

Motivated by this observation, I further investigated post-buckling stability using a continuum beam theory. By including higher order terms in the perturbation analysis of the beam, I observed similar trends as those observed in the idealized model. Therefore, I conclude that it is necessary to include higher order terms in the perturbation analysis that were truncated in previous work [52], to capture all important regimes of post-buckling stability of columns with cubic nonlinear constitutive laws.

I found the higher order solutions (up to 14-th order accuracy) of perturbation problem for a fixed-free column, where all of the solutions with 6-th or higher order of accuracy reveal the existence of a partially stable post-buckling regime for a range of cubic parameter E_2I_2. In order to extend the analysis presented here to further cases such as pined-pined, fixed-pinned, and fixed-fixed columns two major steps are necessary. First, to derive the Euler equation by taking the derivative of the total energy of the system with respect to the deflection curve. Second, to identify the boundary conditions corresponding to each loading scenario. Hence, in principle, it would be possible to conduct a similar analysis and examine the post-buckling stability of columns with cubic constitute law subject to a variety of loading following the method of this chapter.

On a bigger picture perspective, this work helps us recognize the high sensitivity of post-buckling stability and dynamics on the nonlinearity of the constitutive law. It reinforces the need for accurately identifying the nonlinearity in the constitutive law for modeling and simulating the buckling dynamics of biological filaments using rod models.

Chapter 3

ROD MODEL WITH USER-DEFINED CONSTITUTIVE LAW

3.1 Introduction

A continuum rod model, in general, consists of dynamic equilibrium equations and compatibility equations, which need to be solved respecting the prescribed constitutive law. Although dynamic equilibrium equations and compatibility conditions, which I henceforth refer to as the *rod model*, remain the same for all slender structures, the key distinguishing factor is the constitutive law. Accurate identification of constitutive law parameters that are not directly measurable involve challenging inverse methods.However, in developing inverse methods, a review of which can be found here [47,48], the need first arises for a computational forward model that can efficiently simulate the deformations with any *user-defined* nonlinear constitutive law. Developing a computational rod model that is capable of incorporating user-defined constitutive laws, which is the contribution of this chapter, is also a stepping stone for addressing the research on estimation and identification of constitutive law parameters.

Given the wide range of applications in which the computational rod model is being employed and the commonalities among these applications, a user-friendly computational rod model framework that is applicable across these applications will greatly impact research in these areas. As discussed earlier, while the equations of dynamic equilibrium and compatibility are the same across these variety of applications, the key difference is the exact functional form of the nonlinear constitutive law. This exact functional form of nonlinear constitutive law vary from material to material depending on their atomistic structures [64, 65]. Thus, to develop a user-friendly computational tool employing rod model, an important required feature is to allow the user to prescribe or input any functional form of the constitutive law. Currently available computational rod models, such as [66] that simulate the deformations, are unable to allow the user to define different constitutive laws in a user-friendly way. This is so because the computational model numerically solves the governing nonlinear differential equations with Jacobian-based methods, and the constitutive law contributes to the Jacobian. Any change in the form of the constitutive law thus necessitates extensive rewriting of the parts of the code that relate to the Jacobian. This poses a barrier in modularizing the constitutive law as a user input in the computer program. One way to circumvent this hurdle is to introduce symbolic differentiation to compute the Jacobian. However, symbolic differentiation is computationally very sluggish, and must be avoided, especially when they are required

iteratively within "for" loops. Another brute-force approach is to pre-program a library of different functional forms of the nonlinear constitutive law (along with the respective Jacobians-related codes) and allow users to choose from the list of available functions, but this approach is neither elegant, nor can it handle unanticipated constitutive laws.

Yet another approach is Automatic or Algorithmic Differentiation (AD) [67], which is as accurate as the method of symbolic differentiation and also faster than that. However, the approach that this chapter presents is simpler in programming than AD, yet as accurate. The main focus of this chapter is to allow a user-friendly computational rod model environment wherein a user who is not necessarily familiar with programming of the computational rod model can easily input a constitutive law, the rod parameters, boundary conditions and can compute the rod deformations in a short span of time required to set up the simulation. I achieve this by programming into the model (and Jacobian) not a specific functional form of the constitutive law, but rather basis functions that can be used to represent arbitrary functions. For instance, if powers of the deformation variables are coded into the Jacobian, they can be used to represent any analytic function (by Taylor series expansion) of the deformation variables by simply supplying the appropriate coefficients. This is therefore an efficient approach that has one pre-programmed Jacobian that can accommodate any user-defined constitutive law without requiring symbolic differentiation. In this scheme, the user simply enters the constitutive law desired, and the computer program first expands the user-defined constitutive law into a series (such as Taylor series) or in terms of appropriately chosen basis functions. The coefficients of the series (or the basis functions) are automatically passed on to the Jacobian, the form of which is hard-coded based on the derivative of the series or the basis functions. Thus, this scheme numerically (not symbolically) passes on the information of the functional form of the user-defined constitutive law directly to the Jacobian via coefficients, and no reprogramming by the user is needed.

The above-proposed approach is demonstrated in this chapter by implementing the above scheme into an existing computational rod model [66] using MATLAB, and testing it with hardening, softening and other types of constitutive laws including the implicit forms. I analyzed the results (including the accuracy and speed) for several loading scenarios leading to highly nonlinear rod deformations.

The chapter is organized as follows. Section 3.2 summarizes the mathematical formulation of the dynamic rod model [12] with a general form of a nonlinear constitutive law in bending and torsion. The mathematical formulation consists of nonlinear partial differential equations that need to be integrated numerically for any given initial and boundary conditions. Section 3.3 begins with describing the computational approach for the numerical integration that was adopted in [12]. Section 3.3 then continues further with introducing the proposed strategy for incorporating the user-defined nonlinear constitutive law in the computational approach. Section 3.4 presents some case-studies to compare the proposed strategy with existing (but non user-friendly) approaches.

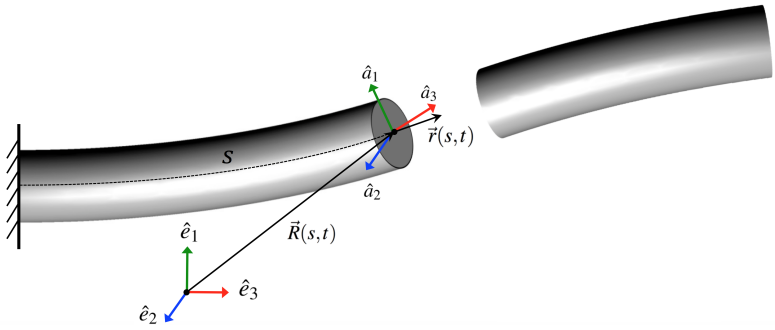

Figure 3.1: The motion of each cross-section of the rod at length s and time t is determined by tracking the transformations of the body-fixed frame $\hat{a}_i(s,t)$ with respect to the inertial frame of reference $\hat{e}_i$.

3.2 Mathematical Formulation of Rod Model

The mathematical formulation of the dynamic rod model that I use [12] employs the classical approach of the Kirchhoff [68] which assumes each cross-section of the rod to be rigid. The position and orientation of each cross-section is determined in space, s and time, t by tracking the transformation of a body-fixed frame, $\hat{a}_i(s,t)$ with respect to an inertial frame of reference, $\hat{e}_i$ that are shown in Figure 3.1, where subscript $i = 1,2,3$.

Vector $\vec{R}(s,t)$ defines the position of the body-fixed reference frame, $\hat{a}_i(s,t)$ relative to the inertial frame of reference, $\hat{e}_i$. The spatial derivative of $\vec{R}(s,t)$, which I denote by $\vec{r}(s,t)$, is in the tangential direction along the centerline. Deviation of $\vec{r}(s,t)$ from the unit normal of a cross-section determines the shear and stretch at that cross-section. The change in magnitude of $\vec{r}(s,t)$ quantifies the extension or compression along s, and the change in its orientation with respect to the body-fixed frame, $\hat{a}_i(s,t)$ quantifies shear. Furthermore, the spatial rate of change of cross-sectional orientation is denoted by $\vec{\kappa}(s,t)$ and describes the curvature and twist of the rod. In general, the rod may be intrinsically curved and twisted in its stress-free state. I denote this stress-free curvature and twist by $\vec{\kappa}_0(s)$. The stress distribution over the cross-section of the rod results in a net internal force, $\vec{f}(s,t)$ and a net internal moment, $\vec{q}(s,t)$. Moreover, the translational velocity, $\vec{v}(s,t)$ and angular velocity, $\vec{\omega}(s,t)$ corresponding to the frame $\hat{a}_i(s,t)$ are used to describe the rigid-body motion of the cross-sections.

Thus, the dynamics of rod deformation is described by six vector fields, $\vec{\kappa}(s,t)$ and $\vec{r}(s,t)$ that represent deformation of the rod, $\vec{q}(s,t)$ and $\vec{f}(s,t)$ that represent the restoring moment and force, and $\vec{v}(s,t)$ and $\vec{\omega}(s,t)$ that represent motion of each cross-section. These six vector fields must satisfy equations of dynamic equilibrium and compatibility as well as a constitutive law.

3.2.1 Equilibrium and Compatibility Equations

By applying Newton's second law to an element of the rod with infinitesimal length, the equations of equilibrium (3.1) and (3.2) are derived. The compatibility equations (3.3) and (3.4) follow from the space-time continuity of the cross-section position, $\vec{R}(s,t)$, and the space-time continuity of the transformation that maps $\hat{a}_i(s,t)$ to $\hat{e}_i$, respectively.

$$m(\frac{\partial \vec{v}}{\partial t} + \vec{\omega} \times \vec{v}) - (\frac{\partial \vec{f}}{\partial s} + \vec{\kappa} \times \vec{f}) - \vec{F} = \vec{0} \tag{3.1}$$

$$\underline{\mathbf{I_m}} \frac{\partial \vec{\omega}}{\partial t} + \vec{\omega} \times \underline{\mathbf{I_m}} \vec{\omega} - (\frac{\partial \vec{q}}{\partial s} + \vec{\kappa} \times \vec{q}) + \vec{f} \times \vec{r} - \vec{Q} = \vec{0} \tag{3.2}$$

$$\frac{\partial \vec{r}}{\partial t} + \vec{\omega} \times \vec{r} - (\frac{\partial \vec{v}}{\partial s} + \vec{\kappa} \times \vec{v}) = \vec{0} \tag{3.3}$$

$$\frac{\partial \vec{\kappa}}{\partial t} - (\frac{\partial \vec{\omega}}{\partial s} + \vec{\kappa} \times \vec{\omega}) = \vec{0} \tag{3.4}$$

In Eqs. (3.1) to (3.4) all the derivatives are relative to the body-fixed reference frame, m is the mass of the rod per unit length, and $\underline{\mathbf{I_m}}(s)$ is a 3-by-3 tensor of the moments of inertia per unit length. The interaction of the rod with the environment is captured with external force per unit length $\vec{F}(s,t)$ as well as the external moment per unit length $\vec{Q}(s,t)$.

3.2.2 Constitutive Law

The differential equations of equilibrium and compatibility have to be solved together with a constitutive law to find the six unknown vector fields. The constitutive law describes the relationship between the deformation of the rod and the restoring internal force and moment. In general, an elastic constitutive law can be written as the following set of implicit algebraic equations in an $\mathbb{R}^6$ space:

$$\Psi\left(\vec{q}, \vec{f}, \vec{\kappa}, \vec{r}, s\right) = 0\ ,\ \ \Psi \in \mathbb{R}^3 \times \mathbb{R}^3 \times \mathbb{R}^3 \times \mathbb{R}^3 \times \mathbb{R} \to \mathbb{R}^6. \tag{3.5}$$

However, for an inextensibile rod $\vec{r}(s,t)$ has unit magnitude, and for an unshearable rod, its orientation relative to the body-fixed frame is constant. Therefore, for an inextensible and unshearable rod, $\frac{\partial \vec{r}(s,t)}{\partial t} = \vec{0}$. Extension and shear are indeed negligible in majority of applications of thin rods in low-tension or compression, for which deformation of the rod is dominated by large bending and twisting. So, I describe the numerical approach in this chapter for inextensible and unshearable rods, but recognize that the same approach is applicable to a geometrically exact rod as well. I further assume the constitutive law to be such that the restoring moment is an explicit function of curvature and twist and not dependent on the internal forces. Thus, the constitutive law takes the following form:

$$\vec{q} = \vec{\psi}(\vec{\kappa} - \vec{\kappa}_0, s),\ \ \vec{\psi} \in \mathbb{R}^3 \times \mathbb{R} \to \mathbb{R}^3, \tag{3.6}$$

where recall that $\vec{\kappa}_0$ describes the initial stress-free curvature and twist of the rod. Note that in this case, I have one less vector field to solve for ($\vec{r}(s,t)$ is constant, not variable). Furthermore, the constitutive law (Eq. (3.6)) can be directly substituted in the angular momentum equation (Eq. (3.2)) to eliminate $\vec{q}(s,t)$. In particular, the constitutive law is used to express the internal moment, $\vec{q}$ and its derivatives in terms of $\vec{\kappa}$ using the total derivative of function $\vec{\psi}$ given in equation (3.7) below:

$$\frac{\partial \vec{q}}{\partial s} = \frac{\partial \vec{\psi}}{\partial \vec{\kappa}} \frac{\partial \vec{\kappa}}{\partial s} - \frac{\partial \vec{\psi}}{\partial \vec{\kappa}_0} \frac{d\vec{\kappa}_0}{ds} + \frac{\partial \vec{\psi}}{\partial s}. \tag{3.7}$$

With this substitution, I am left with four vector differential equations to solve for four unknown vector fields, namely, $\vec{v}(s,t)$, $\vec{\omega}(s,t)$, $\vec{\kappa}(s,t)$ and $\vec{f}(s,t)$. The four partial differential equations of equilibrium and compatibility can be assembled as described next, to apply a numerical integration scheme.

3.2.3 Assembled System of Equations

The equations of the inextensible and unshearable rod model (Eqs. (3.1) to (3.4)) are assembled after substitution of the constitutive law (Eq. (3.6) and its spatial derivative Eq. (3.7)) to write them in the following compact form:

$$\mathbf{M}\frac{\partial \mathbf{Y}}{\partial t} + \mathbf{K}\frac{\partial \mathbf{Y}}{\partial s} + \mathbf{F} = \mathbf{0}. \tag{3.8}$$

Here,

$$\mathbf{Y} = \begin{bmatrix} \vec{v} \\ \vec{\omega} \\ \vec{\kappa} \\ \vec{f} \end{bmatrix} \tag{3.9}$$

is a 12×1 column matrix of unknowns, to be solved for, that describe the dynamic state of the system. $\mathbf{M}$ and $\mathbf{K}$ are 12×12 matrices that describe the overall inertia and stiffness of the system, and $\mathbf{F}$ is a 12×1 column matrix of non-homogeneous terms. In the computational script, I assembled the four equations in the following order: Eq. (3.3), (3.4, (3.2, and finally(3.1) that resulted in the following form of $\mathbf{M}$, $\mathbf{K}$ and $\mathbf{F}$:

$$\mathbf{M} = \begin{bmatrix} \mathbf{O} & \mathbf{O} & \mathbf{O} & \mathbf{O} \\ \mathbf{O} & \mathbf{O} & \mathbf{I} & \mathbf{O} \\ \mathbf{O} & \mathbf{I_m} & \mathbf{O} & \mathbf{O} \\ m\mathbf{I} & \mathbf{O} & \mathbf{O} & \mathbf{O} \end{bmatrix}, \tag{3.10}$$

$$\mathbf{K} = -\begin{bmatrix} \mathbf{I} & \mathbf{O} & \mathbf{O} & \mathbf{O} \\ \mathbf{O} & \mathbf{I} & \mathbf{O} & \mathbf{O} \\ \mathbf{O} & \mathbf{O} & \frac{\partial \vec{\psi}}{\partial \vec{\kappa}} & \mathbf{O} \\ \mathbf{O} & \mathbf{O} & \mathbf{O} & \mathbf{I} \end{bmatrix}, \tag{3.11}$$

$$\mathbf{F} = \begin{bmatrix} \vec{\omega} \times \vec{r} - \vec{\kappa} \times \vec{v} \\ -\vec{\kappa} \times \vec{\omega} \\ -(\frac{\partial \vec{\psi}}{\partial s} - \frac{\partial \vec{\psi}}{\partial \vec{\kappa}_0} \frac{d\vec{\kappa}_0}{ds}) + \vec{\omega} \times \underline{\mathbf{I_m}} \vec{\omega} + \vec{f} \times \vec{r} - \vec{\kappa} \times \vec{\psi} - \vec{Q} \\ m(\vec{\omega} \times \vec{v}) - \vec{\kappa} \times \vec{f} - \vec{F} \end{bmatrix}. \tag{3.12}$$

In Eqs. (3.10) and (3.11), the symbols **I** and **O** respectively refer to the identity tensor and the null tensor (with the dimensions of 3×3). Note that the four rows of **M**, **K**, and **F** correspond to the four equations of rod model and their order is immaterial.

The *Generalized-α method* [69] is adopted to compute the numerical solution of this system, subjected to necessary and sufficient initial and boundary conditions. To compute the geometric shape of the rod I use the method of incremental rotation [12, 70] to construct the transformation matrix from body-fixed frame to an inertial frame. The rod model formulation presented here is distinctly different from geometrically local approaches that were first proposed by Simo and L. Vu-Quoc [71] and describe configuration of a slender structure locally by using displacements and the rotation of a cross-section. There are many choices to parametrize the rotation of a cross-section in geometrically local approaches and various approaches such as Euler angles [72], the rotation vector [73], and Euler parameters [74] have been used. In the following section, I illustrate how the *Generalized-α method* is applicable to a rod with nonlinear and non-homogenous constitutive law. Here, note that **K** and **F** have the contribution of the nonlinear constitutive law from its derivative given by Eq. (3.7), and therefore must have contribution to the Jacobian of the system. In the next section, I introduce my strategy for implementation of the user-defined nonlinear constitutive law in the computational approach.

3.3 Numerical Algorithm with User-Defined Constitutive Law

I first devise a numerical algorithm in Section 3.3.1 that is general enough to allow for any constitutive law by expressing it in terms of the arbitrary function $\vec{\psi}$. In doing so, I identify the parts of the algorithm that get affected by $\vec{\psi}$, the constitutive law. Then, in Section 3.3.2, I introduce how a symbolic implementation would (traditionally) take care of any constitutive law given any arbitrary function $\vec{\psi}$. This is the most accurate approach, but computationally extremely sluggish due to recurring symbolic differentiations. Finally, in Section 3.3.3, I introduce my user-friendly and computationally efficient strategy for inputting the user-defined nonlinear constitutive law that circumvents the need of symbolic differentiation.

3.3.1 Generalized-α Discretization

For a rod with linear and homogenous constitutive law, the matrices $\mathbf{M}$ and $\mathbf{K}$ are constant and are not discretized in space and time. Therefore, Eq. (3.8) can be discretized as

$$\mathbf{M}(\frac{\partial \mathbf{Y}}{\partial t})^{1-\alpha_t}_{1-\alpha_s} + \mathbf{K}(\frac{\partial \mathbf{Y}}{\partial s})^{1-\beta_t}_{1-\beta_s} + \mathbf{F}^{1-\beta_t}_{1-\beta_s} = \mathbf{0}, \tag{3.13}$$

in which the notation $\mathbf{A}^{1-x}$ and $\mathbf{A}_{1-x}$ for any quantity $\mathbf{A}$ and any parameter x, are defined as follows.

$$\mathbf{A}^{1-x} = (1-x)\mathbf{A}^{\dot{\mathbb{i}}} + x\mathbf{A}^{\dot{\mathbb{i}}-1} \tag{3.14}$$

$$\mathbf{A}_{1-x} = (1-x)\mathbf{A}_{\mathbb{j}} + x\mathbf{A}_{\mathbb{j}-1} \tag{3.15}$$

The indices $\mathbb{i}$ and $\mathbb{j}$ enumerate the discretized nodes in time and space, respectively. The parameters α_t and α_s are called mass averaging parameters and β_t and β_s are stiffness averaging.

In the case of nonlinear constitutive laws, the term $\frac{\partial \vec{\psi}}{\partial \vec{\kappa}}$ in the stiffness matrix $\mathbf{K}$, depends on the curvature and twist vector, therefore, it varies in space and time and is discretized as given in Eq. (3.16).

$$\begin{aligned}\mathbf{K}^{1-\beta_t}_{1-\beta_s} = \Big[(1-\beta_t)\Big((1-\beta_s)\mathbf{K}^{\dot{\mathbb{i}}}_{\mathbb{j}} + \beta_s\mathbf{K}^{\dot{\mathbb{i}}}_{\mathbb{j}-1}\Big) + \\ \beta_t\Big((1-\beta_s)\mathbf{K}^{\dot{\mathbb{i}}-1}_{\mathbb{j}} + \beta_s\mathbf{K}^{\dot{\mathbb{i}}-1}_{\mathbb{j}-1}\Big)\Big]\end{aligned} \tag{3.16}$$

For non-homogeneous rods the mass matrix $\mathbf{M}$ varies along the length of rod but not in time. Therefore, the discretized form of the system can be written as

$$\mathbf{M}_{1-\alpha_s}(\frac{\partial \mathbf{Y}}{\partial t})^{1-\alpha_t}_{1-\alpha_s} + \mathbf{K}^{1-\beta_t}_{1-\beta_s}(\frac{\partial \mathbf{Y}}{\partial s})^{1-\beta_t}_{1-\beta_s} + \mathbf{F}^{1-\beta_t}_{1-\beta_s} = \mathbf{0}. \tag{3.17}$$

The derivatives of $\mathbf{Y}$ are then discretized with Newmark-like formulation. In Eqs. (3.18) and (3.19) the Newmark constants γ_t and γ_s control the averaging of time and space derivatives.

$$(\frac{\partial \mathbf{Y}}{\partial t})^{\dot{\mathbb{i}}} = \frac{\mathbf{Y}^{\dot{\mathbb{i}}} - \mathbf{Y}^{\dot{\mathbb{i}}-1}}{\gamma_t \Delta t} - \frac{1-\gamma_t}{\gamma_t}(\frac{\partial \mathbf{Y}}{\partial t})^{\dot{\mathbb{i}}-1} \tag{3.18}$$

$$(\frac{\partial \mathbf{Y}}{\partial s})_{\mathbb{j}} = \frac{\mathbf{Y}_{\mathbb{j}} - \mathbf{Y}_{\mathbb{j}-1}}{\gamma_s \Delta s} - \frac{1-\gamma_s}{\gamma_s}(\frac{\partial \mathbf{Y}}{\partial s})_{\mathbb{j}-1} \tag{3.19}$$

Applying this scheme to the Eq. (3.17) results in an algebraic equation with nonlinear terms of $\mathbf{Y}^{\dot{\mathbb{i}}}_{\mathbb{j}}$ and $\mathbf{Y}^{\dot{\mathbb{i}}}_{\mathbb{j}-1}$ and linear terms of $(\frac{\partial \mathbf{Y}}{\partial s})^{\dot{\mathbb{i}}}_{\mathbb{j}-1}$. In Eq. (3.20), $A(\mathbf{Y}^{\dot{\mathbb{i}}}_{\mathbb{j}})$ and $B(\mathbf{Y}^{\dot{\mathbb{i}}}_{\mathbb{j}-1})$ represent the nonlinear terms, $\mathbf{H}$ contains all of the known terms from previous time-step

$(\dot{\mathbb{i}}-1)$, and the matrix $\hat{\mathbf{K}}$ is given in Eq. (3.21).

$$\hat{\mathbf{K}}(\frac{\partial \mathbf{Y}}{\partial s})^{\dot{\mathbb{i}}}_{\dot{\mathbb{j}}-1} + A(\mathbf{Y}^{\dot{\mathbb{i}}}_{\dot{\mathbb{j}}}) + B(\mathbf{Y}^{\dot{\mathbb{i}}}_{\dot{\mathbb{j}}-1}) = \mathbf{H} \tag{3.20}$$

$$\hat{\mathbf{K}} = (1-\beta_t)\Big(\beta_s - (1-\beta_s)(\frac{1-\gamma_s}{\gamma_s})\Big)\mathbf{K}^{1-\beta_t}_{1-\beta_s} \tag{3.21}$$

To derive an integrable linear algebraic equation in the space, Eq. (3.20) is linearized about a guessed solution. The linearization requires the calculation of the Jacobian of the terms $A(\mathbf{Y}^{\dot{\mathbb{i}}}_{\dot{\mathbb{j}}})$ and $B(\mathbf{Y}^{\dot{\mathbb{i}}}_{\dot{\mathbb{j}}-1})$ that I will show with $\mathbf{A_Y}$ and $\mathbf{B_Y}$.

$$\mathbf{A_Y} = (1-\alpha_t)(1-\alpha_s)\Big(\frac{\mathbf{M}_{1-\alpha_s}}{\gamma_t \Delta t}\Big) + (1-\beta_t)(1-\beta_s)\Big(\frac{\mathbf{K}^{1-\beta_t}_{1-\beta_s}}{\gamma_s \Delta s} + \mathbf{F}_{\mathbf{Y}^{\dot{\mathbb{i}}}_{\dot{\mathbb{j}}}}\Big) \tag{3.22}$$

$$\mathbf{B_Y} = (1-\alpha_t)(\alpha_s)\Big(\frac{\mathbf{M}_{1-\alpha_s}}{\gamma_t \Delta t}\Big) + (1-\beta_t)\Big((1-\beta_s)\frac{\mathbf{K}^{1-\beta_t}_{1-\beta_s}}{\gamma_s \Delta s} + \beta_s \mathbf{F}_{\mathbf{Y}^{\dot{\mathbb{i}}}_{\dot{\mathbb{j}}-\mathbb{1}}}\Big) \tag{3.23}$$

To linearize the terms $A(\mathbf{Y}^{\dot{\mathbb{i}}}_{\dot{\mathbb{j}}})$ and $B(\mathbf{Y}^{\dot{\mathbb{i}}}_{\dot{\mathbb{j}}-1})$, the Jacobian of the vector $\mathbf{F}$ needs to be calculated. The Jacobian of $\mathbf{F}$ which is called $\mathbf{F_Y}$ is given in Eq. (3.24) for the case that external force and external moment, $\vec{F}$ and $\vec{Q}$, do not depend on $\mathbf{Y}$.

$$\mathbf{F_Y} = \begin{bmatrix} -\tilde{\kappa} & -\tilde{r} & \tilde{v} & \mathbf{O} \\ \mathbf{O} & -\tilde{\kappa} & \tilde{\omega} & \mathbf{O} \\ \mathbf{O} & \tilde{\omega}\underline{\mathbf{I_m}} - \widetilde{(\underline{\mathbf{I_m}}\vec{\omega})} & \tilde{\psi} - \tilde{\kappa}\frac{\partial \vec{\psi}}{\partial \vec{\kappa}} + \mathbf{J}_{\psi_s} & -\tilde{r} \\ m\tilde{\omega} & -m\tilde{v} & \tilde{f} & -\tilde{\kappa} \end{bmatrix} \tag{3.24}$$

The symbol $\tilde{v}$ in Eq. (3.24) represents the skew-symmetric tensor associated with the vector $\vec{v}$ generated as follows from its components

$$\tilde{v} = \begin{bmatrix} 0 & -v_3 & v_2 \\ v_3 & 0 & -v_1 \\ -v_2 & v_1 & 0 \end{bmatrix}, \tag{3.25}$$

and the $\mathbf{J}_{\psi_s}$ is given below.

$$\mathbf{J}_{\psi_s} = -\frac{\partial\big(\frac{\partial \vec{\psi}}{\partial s} - \frac{\partial \vec{\psi}}{\partial \vec{\kappa}_0}\frac{d\vec{\kappa}_0}{ds}\big)}{\partial \vec{\kappa}} \tag{3.26}$$

Equation (3.20) is linearized around a guessed solution. This means that the terms $\mathbf{A_Y}$, $\mathbf{B_Y}$, and $\hat{\mathbf{K}}(\frac{\partial \mathbf{Y}}{\partial s})^{\dot{\mathbb{i}}}_{\dot{\mathbb{j}}-1}$ are calculated using the guessed solution so that the Eq. (3.20)

```
for i = 1,2,...
    choose a guessed solution Y*^i
    while shooting iteration not converged
        for j = 1,2,...
            Calculate A_Y, B_Y, and H*
            Integrate Eq. (27) in space to solve Y_j^i
        end for
        update the guessed solution
        check the shooting method convergence (||Y*^i − Y^i||_2 < ε)
    end while
end for
```

Figure 3.2: The algorithm of the numerical scheme. The guessed solution for all spatial nodes is shown with $\mathbf{Y}^{*\mathbb{i}}$. At each time-step the linearized equation is integrated in space. The spatial integration is iterated and is used to update the guessed solution until it converges to the true solution $\mathbf{Y}^{\mathbb{i}}$ bounded by a small tolerance ε.

rendered integrable with respect to $\mathbf{Y}^{\mathbb{i}}_{\mathbb{j}}$ in space.

$$\mathbf{A_Y}\mathbf{Y}^{\mathbb{i}}_{\mathbb{j}} + \mathbf{B_Y}\mathbf{Y}^{\mathbb{i}}_{\mathbb{j}-1} = \mathbf{H}^* \tag{3.27}$$

The matrix $\mathbf{H}^*$ contains all of the known terms from previous time-step $(\mathbb{i}-1)$ as well as the linearization terms that depend on the guessed solution.

In most scenarios, the boundary condition contains partial information on $\mathbf{Y}$ at one end ($s=0$) and the rest is known at the other end ($s=L$). For example, in the Figure 3.1 the left hand side of the rod is fixed by a clamp which imposes $\vec{v}(0,t)=\vec{0}$ and $\vec{\omega}(0,t)=\vec{0}$, while on the right hand side the external forces and moments, $\vec{f}(L,t)$ and $\vec{q}(L,t)$ are prescribed. I use the shooting method at each time-step as explained by [75] to start integration from one end and match the boundary conditions at the other end. Alternatively, an assembled matrix approach can also be used to match the boundary conditions at both the ends simultaneously. Figure 3.2 shows the algorithm of how shooting method is applied to this problem.

Now the aim is to implement the numerical solution of the rod model as explained here in a way that user has to provide the initial and boundary conditions for the simulation, the parameters for the numerical scheme (α_t, α_s, β_t, β_s, γ_t, γ_s, Δ_t, and Δ_s), the physical properties of the rod (L, m, $\underline{\mathbf{I_m}}$), and the function $\vec{\psi}$ that describes the constitutive law of the rod. The constitutive law is allowed to have any arbitrary functional form and its derivatives need to be calculated for this formulation. In particular, the matrices $\mathbf{K}$ and $\mathbf{F}$ in Eqs. (3.11) and (3.12) depend on the constitutive law and its derivatives. In addition, the Jacobian of the matrix $\mathbf{F}$ as represented in Eq. (3.24) also depends on the derivatives of the constitutive law.

In the next two sections, I discuss two approaches to incorporate a user-defined constitutive law with an arbitrary functional form in the numerical solution of the rod model. The first approach uses accurate description of the constitutive law and its derivatives while the second approach, which I propose, approximates the constitutive law using polynomial functions. It is important to note that by approximating the matrices $\mathbf{K}$ and $\mathbf{F}$, the true solution of the system $\mathbf{Y}$ will be directly affected while by approximating the Jacobian $\mathbf{F_Y}$ merely the number of iterations for guessed solution to converge may get affected and the true (converged) solution will remain unchanged. Such approximation of the Jacobian does not necessarily increase the Newton-Raphson iterations. Instead, a slightly inexact Jacobian helps overcome some known singularities that are encountered with exact Jacobian.

It is also important to note that an alternative way to assemble the system of equations in comparison to Eqs. (3.8) and (3.9) would be to use a five-variable formulation. By defining the state variable to be $\mathbf{Y} = [\vec{v}, \vec{\omega}, \vec{f}, \vec{q}, \vec{\kappa}]$ there would be no substitution of the constitutive law in Eq. (3.2) and therefore the matrices $\mathbf{K}$ and $\mathbf{F}$ will not contain any term that depends on the derivatives of the constative law. Instead of the substitution, the constitutive law will be captured through the fifth row of the system of equations in order to complete the five-variable formulation. However, elaborating on the implementation of the five-variable variable formulation is not in the scope of this chapter.

3.3.2 Symbolic Implementation

I will compare the performance of my method with that of the symbolic implementation, which is the most accurate approach. So, here I describe how I used the method of symbolic implementation in getting my benchmark results.

The constitutive law is defined as an input by the user in terms of the scalar symbolic variables $\kappa_1, \kappa_2, \kappa_3$, and s in the form similar to Eq. (3.6). The matrices $\mathbf{K}$, $\mathbf{F}$, and $\mathbf{F_Y}$ are implemented in terms of the symbols $\kappa 1$, $\kappa 2$, $\kappa 3$, and s and MATLAB substitute command is used to compute the value of these matrices. The algorithm as shown in Figure 3.2 requires the calculation of matrices $\mathbf{K}$, $\mathbf{F}$, and $\mathbf{F_Y}$ at each space-step. The shooting method iteration will repeat the spatial integration until it converges which requires reevaluation of all matrices. Therefore, the accuracy of this description comes with a high computational cost due to iterative calculation of the matrices of symbolic type. A comparison of the computational costs among the two methods is presented in the subsequent sections.

3.3.3 Least-Squares Polynomial Approximation

The second method that this chapter contributes has a similar user interface in which the constitutive law is defined symbolically as expressed in equation (3.6). However in this approach the least-squares polynomial fitting is used to approximate the functions ψ_i where subscript $i = 1,2,3$ as given in the following equation.

$$q_i = \sum_{j=0}^{n_1} \sum_{k=0}^{n_2} \sum_{l=0}^{n_3} \sum_{m=0}^{n_4} p_{jklm} \kappa_1^j \kappa_2^k \kappa_2^l s^m \tag{3.28}$$

The user can control and choose the order of the polynomial functions so that approximations match well with the true constitutive law or it can be automated with a convergence criteria.

For the cases in which the two axes of bending of the rod and its one axis of twist are decoupled, the polynomial approximation reduces to

$$q_i = \sum_{j=0}^{n_1} \sum_{k=0}^{n_2} p_{jk} \kappa_i^j s^k. \tag{3.29}$$

And finally if in addition to the decoupling, the rod also has homogeneous elastic properties, the function approximation can be written as

$$q_i = \sum_{j=0}^{n} p_j \kappa_i^j. \tag{3.30}$$

Therefore, in this approach the matrices $\mathbf{K}$, $\mathbf{F}$, and $\mathbf{F_Y}$ are defined in terms of arrays of polynomial coefficients, for example p_j's that are calculated before entering the iteration loops. For instance, the derivative of the function ψ_i with respect to the curvature or twist κ_i which appears in both $\mathbf{K}$ and $\mathbf{F_Y}$ has the following form, for any arbitrary constitutive law.

$$\frac{\partial q_i}{\partial \kappa_i} = \sum_{j=1}^{n} j p_j \kappa_i^{j-1} \tag{3.31}$$

Thus, there is no need for symbolic description of the constitutive law and it is expected to gain a significant computation advantage by using this method. This will be addressed in the following sections with more detail.

To compute the derivative of the constitutive law and using these values in the Jacobian and other matrices, one might also use an existing technique of *Automatic Differentiation* as described in [67]. Automatic differentiation (AD) uses exact formulas along with floating-point values, instead of expression strings as in symbolic differentiation, and it involves no approximation error as in numerical differentiation using difference quotients. This method is as accurate as symbolic differentiation and very quick in computation also.

But using this technique might not be of great help when compared to the method mentioned above. The constitutive laws in real life will not be too complex which cannot be approximated accurately by Taylor Series. The current method as shown in the previous examples is giving very accurate results when compared with symbolic differentiation. Also, understanding and then implementing Automatic Differentiation in the rod theory will take some extra effort. Introducing this new technique might just make the current code complex and might not be of significant help when studying the non-convex constitutive laws.

3.4 Results

In this section a case study is defined to illustrate and compare the results of the two methods that are previously explained. In order to show the effect of nonlinear constitutive laws on the overall dynamics and mechanics of the rod I also present the results for a rod with linearized constitutive laws in bending and torsion.

All the simulations are conducted for a rod with an intrinsic curvature $\vec{\kappa}_0$ that corresponds to a helix and resembles a coil spring. There are many scenarios in which these types of structures are important. For example, recently it is shown [4] how the injection mechanism of the viral genome which involves compressing and stressing helical proteins can be understood and modeled by the continuum rod model.

3.4.1 Geometry and Properties of the Rod

As explained in previous sections the vector $\vec{\kappa}_0$ captures the stress-free configuration of the rod. In this section a rod with helical shape is simulated by prescribing the $\vec{\kappa}_0$. The rod has an arc-length of 1 meter, the radius and the pitch of the helix are respectively called R and P and are chosen to be both equal to $\frac{\sqrt{2}}{10\pi}$. Therefore the stress-free curvature and twist of the helix is calculated as follows.

$$\vec{\kappa}_0 = \frac{1}{R^2+P^2}(R,R,P) \tag{3.32}$$

The rod has a circular cross-section with the radius of 1 centi meter and its density is 2766.67 $\frac{\text{kg}}{\text{m}^3}$. The rod is assumed to be composed of homogenous isotropic matrial with the following constitutive laws.

$$\psi_1 = EI_1 4arctan(\frac{\kappa_1-\kappa_{01}}{4}) \tag{3.33}$$

$$\psi_2 = EI_2 4arctan(\frac{\kappa_2-\kappa_{02}}{4}) \tag{3.34}$$

$$\psi_3 = GI_3 4arctan(\frac{\kappa_3-\kappa_{03}}{4}) \tag{3.35}$$

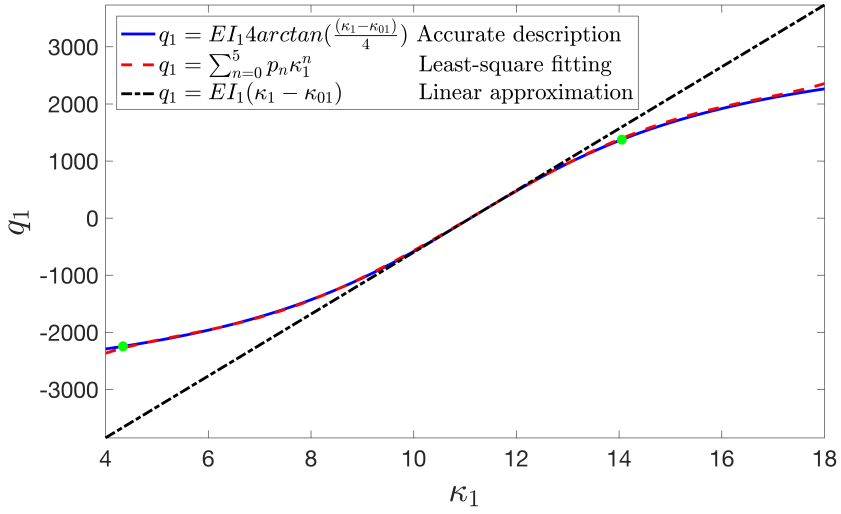

Figure 3.3: Bending constitutive law that captures the relationship between the restoring moment, q_1 and curvature, κ_1. The rod is chosen to be isotropic with a circular cross-section. Therefore, the bending constitutive law for both planes of bending, $q_1 - \kappa_1$ and $q_2 - \kappa_2$, is the same.

In Eqs. (3.33), (3.34), and (3.35), I_1 and I_2 represent the second moment of area of the rod cross-section about the axes $\hat{a}_1$ and $\hat{a}_2$ and I_3 is the polar moment of area of the cross-section about $\hat{a}_3$. The values of the E and G are chosen to correspond to the Young's modulus and shear modulus of the aluminum in its linear elastic regime where $E = 68.95 \times 10^9$ Pa and $G = 27.58 \times 10^9$ Pa.

3.4.2 Loading Scenario

The helical rod that is described in previous section is equivalent to a coil spring. The following boundary conditions are devised to stretch and compress the rod along its helical axis as depicted in Figure 3.5. The end of the rod at $s = 0$ is clamped by imposing $\vec{v}(0,t) = \vec{0}$ and $\vec{\omega}(0,t) = \vec{0}$. The other end at $s = L$ is also clamped but slowly moves toward or away from the clamp at $s = 0$ by prescribing $\vec{v}(L,t) = h(t)\vec{\mathcal{N}}$ and $\vec{\omega}(L,t) = \vec{0}$. The vector $\vec{\mathcal{N}} = (1,1,1)$ is along the helical axis of the rod and the scalar function, $h(t)$ is given by the following expression.

$$h(t) = \pm \begin{cases} 5t \text{ m/s}, & \text{if } t \leq 0.1, \\ 0.5 \text{ m/s}, & \text{otherwise.} \end{cases} \tag{3.36}$$

The positive and negative signs on the right hand side of the Eq. (3.36) respectively correspond to the extension and compression of the spring.

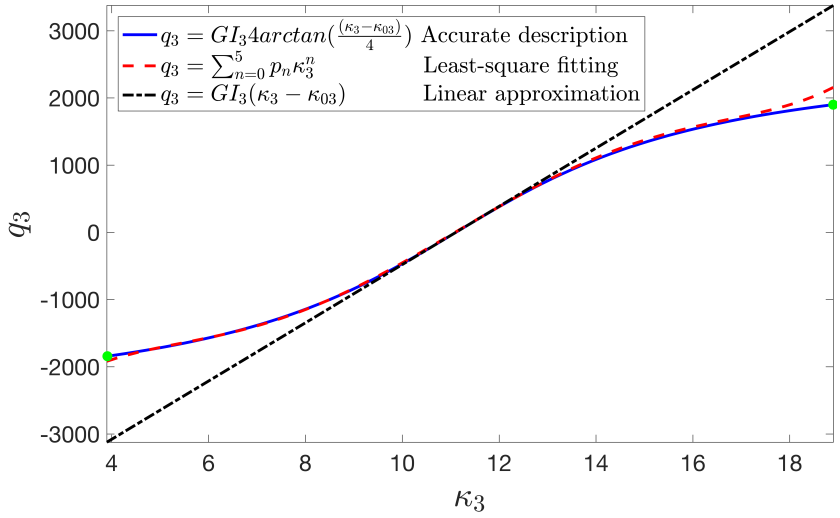

Figure 3.4: Twisting constitutive law that captures the relationship between the restoring torque, q_3 and torsion, κ_3.

In the following section, the force-extension relationship of the rod is extracted from the results of the simulations that are described here.

3.4.3 Force-Extension Relation

In this section the simulation results of the loading scenario that explained previously are compared when the symbolic implementation of the accurate constitutive laws are used versus the case in which the constitutive laws are approximated by a polynomial function as explained in Section 3.3. The least-squares fitting is used to find 5-th order polynomial functions that approximate ψ_i's in the interval $0.4\kappa_{0i} < \kappa_i < 1.6\kappa_{0i}$. The order of polynomial and the range of κ_i's can be controlled by the user for the desirable accuracy. Figures 3.3 and 3.4 show the accurate constitutive laws and the corresponding polynomial approximations as well as the linearized constitutive laws about the initial curvature and twist. The symmetry of the circular cross-section of the rod in addition to the isotropic mechanical properties result into having equal bending constitutive laws or equivalently $I_1 = I_2$ and $\psi_1 = \psi_2$.

Figure 3.6 is showing the force-extension relationships obtained by the two different methods proposed in Section 3.3 as well as the results using the linearized constitutive law. We can see in this figure that the method explained in Section 3.3.3 is able to closely reproduce the same results as the method of Section 3.3.2 which incorporates accurate description of the constitutive laws. I also observe that the linearized constitutive law is over estimating the hardening behavior of this coil spring in stretching while under estimates its softening behavior in compression.

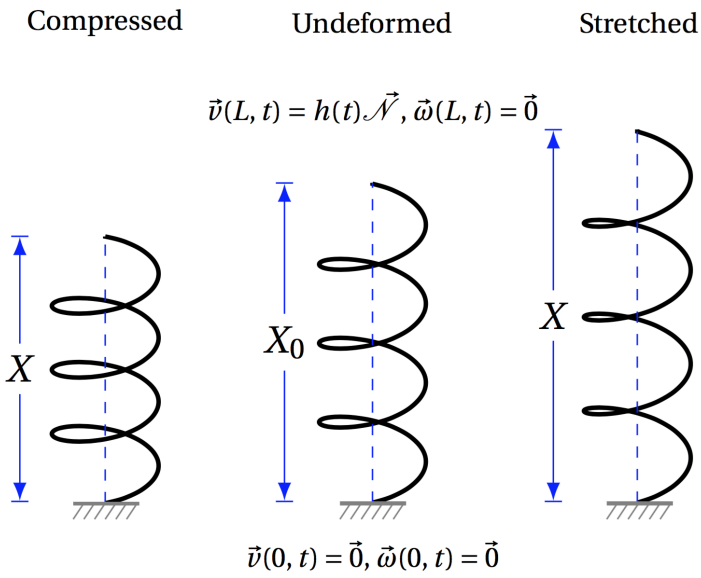

Figure 3.5: Loading scenarios of compressing and stretching the helical rod.

The method of Section 3.3.2, as mentioned before, uses symbolic variables to implement the accurate constitutive laws. This increases the computational cost drastically in comparison to the method of the Section 3.3.3 in which the constitutive laws are approximated by polynomial and there is no need to use the symbolic variables. In particular, the simulations that are presented here take about 4 seconds per time-step for the method of the Section 3.3.3 on a 3.1 GHz Intel Core i7 machine with 16GB of memory, while it takes 400 seconds per time-step when the method of the Section 3.3.2 is used on the same machine.

3.4.4 Dynamic Responce

In this section, to compare the performance of the three methods on the dynamic of the rod a loading scenario defined as follows. The rod is initially at rest. The end of the rod at $s = 0$ is clamped similar to the section 3.4.2. The other end of the rod at $s = L$ is stretched along the axis of helix and then released by prescribing the velocity, $\vec{v}(L,t) = g(t)\vec{\mathcal{N}}$ where $\vec{\mathcal{N}} = (1,1,1)$ and

$$g(t) = \begin{cases} 1000t \text{ m/s}, & \text{if } t \leq 0.005, \\ 5 \text{ m/s}, & \text{if } 0.005 \leq t \leq 0.015. \end{cases} \tag{3.37}$$

For the time $t \geq 0.015$ the end of the rod at $s = 0$ is released to freely vibrate by imposing $\vec{f}(L,t) = \vec{0}$ and $\vec{\kappa}(L,t) = \vec{\kappa}_0$.

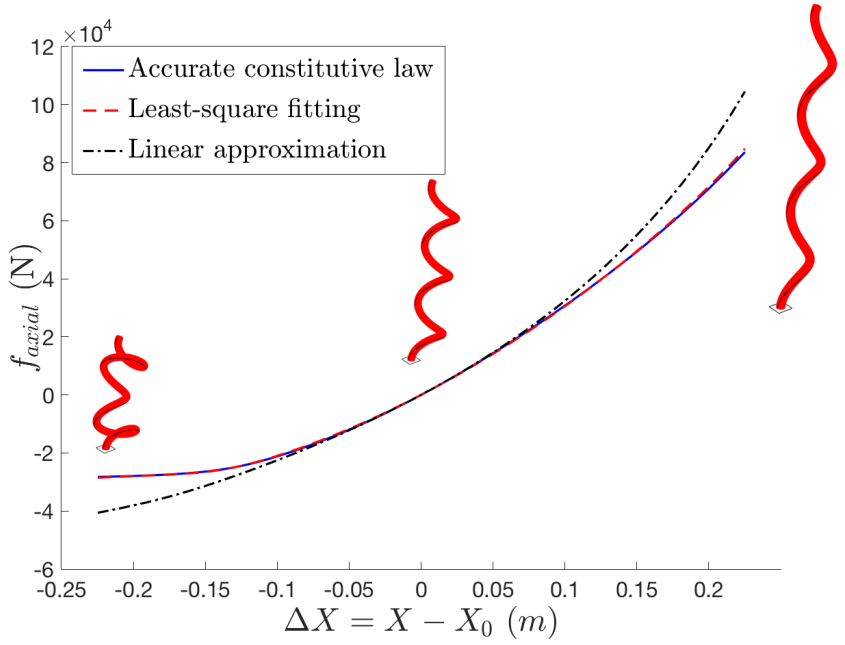

Figure 3.6: This diagram shows the relationship between the magnitude of the force along the axis of the helix, f_{axial} and the change in end-to-end distance, ΔX.

Figure 3.7 is showing the results of the three simulations using the accurate description of the constitutive law, the least-squares fitting method, and the linear approximation of the constitutive law. This figure shows that the polynomial approximation of the constitutive law closely captures the dynamics of the rod when it is compared to the simulation with the accurate description of the constitutive law. Although the deviations of the results using the linear approximation of the constitutive law grows as the time elapses. In these simulations, the rod is surrounded by water and the hydraulic drag which is captured through the external force, $\vec{F}$ in Eq. (3.1) is calculated based on the Morrison law as explained by [27].

$$\vec{F}_{\text{drag}} = -\frac{1}{2}\rho_{\text{f}} d\left(C_n|\vec{v}\times\hat{t}|\hat{t}\times(\vec{v}\times\hat{t}) + \pi C_t(\vec{v}\cdot\hat{t})|\vec{v}\times\hat{t}|\hat{t}\right) \tag{3.38}$$

Here, the diameter of the rod is $d = 2\times10^{-2}$ m, the normal drag coefficient $C_n = 0.1$, the tangential drag coefficient is $C_t = 0.01$, and ρ_{f} is the surrounding fluid density which is chosen to be water. The vector $\hat{t}$ represents the vector $\vec{r}$ for an inextensible and unshearable rod.

3.5 Discussion and Conclusions

This chapter contributes a simple and fast method of implementing any arbitrary user-defined constitutive law in a computational rod model. The method avoids symbolic

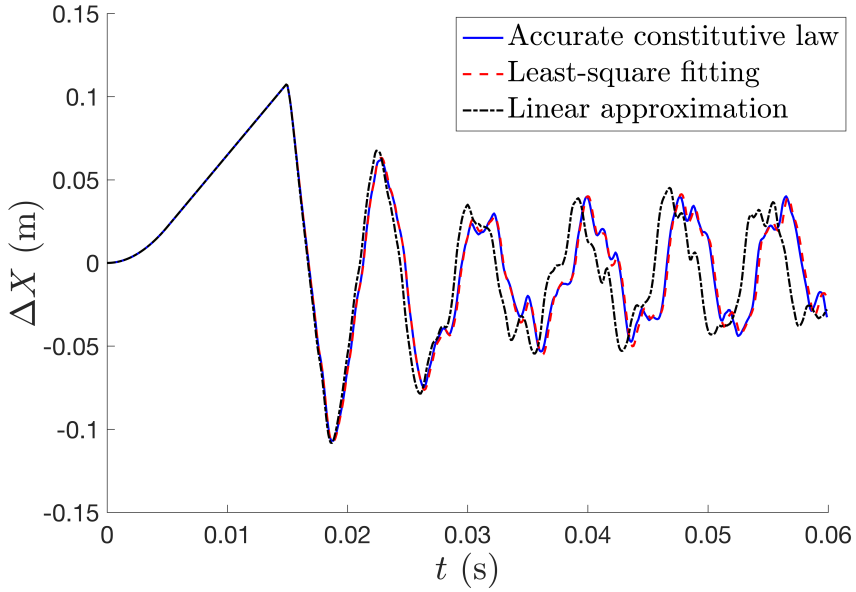

Figure 3.7: The vibrations of the rod is calculated via three different descriptions of the constitutive law. The end-to-end distance of the rod ΔX is plotted versus time using the accurate description of the constitutive law, the least-squares fitting and the linear approximation of the constitutive law.

differentiation by expanding the user-input constitutive law function in a series and using the derivative of the series in the Jacobian. Thus, the method automatically modifies the Jacobian based on the coefficients in the series expansion. The performance of the method is presented for hardening and softening constitutive laws in the force-extension behavior of a helical spring. The effect of nonlinearity in the constitutive law is also emphasized by comparing the results with those for linearized constitutive laws. This comparison further reinforces the need for accurately identifying the nonlinearity in the constitutive law for modeling and simulating the buckling dynamics of biological filaments using rod models.

Chapter 4

AN INVERSE APPROACH DIRECTLY BASED ON FORWARD ROD MODEL FOR NONLINEAR CONSTITUTIVE LAWS

4.1 Introduction

Biological filaments with large length-to-thickness ratio exhibit pronounced bending and twisting deformations that influence their biological functions. For example, looping or supercoiling of DNA, often mediated by proteins is an important step in the gene regulation mechanism [76]. Miele *et al* [77] have also shown that favorable sites of nucleosome formation are not only a function of intrinsic shape of the DNA but also of sequence-dependent elastic properties. Molecular dynamics (MD) methods provide the capability for all-atom simulations and several studies of DNA with these methods has shown encouraging results for modeling the structural deformations of DNA [78]. However the high computational cost becomes a drawback in the MD simulation of large systems. To avoid high computational costs of atomic models, one can use a macroscopic description of a filament as a continuous system. Rod models, in particular, have been shown to be both effective and efficient in capturing essential properties such as *lac* repressor looping [79]. Yet, application of continuum rod theory is dependent on having accurate models of constitutive laws for biological filaments. Unfortunately, direct experimental measurements that can lead to identifying the constitutive law are technologically impractical for most biological filaments due to their sub-micron size and very large thermal fluctuations. There have been several experiments that show that it is possible to estimate average bending and torsional stiffness [80, 81] in DNA strands. However, the experimental derivation of the full functional form of the constitutive laws remains elusive. Developing a computational approach for accurate identification of the constitutive law, hence would be a timely effort. Hinkle et al. [82] proposed an approach that uses a continuum rod model with static deformation data generated from discrete-structure simulation which has shown encouraging success in estimating the constitutive law.

This chapter presents an inverse approach to use the dynamic deformation data, generated by forward rod model, for identifying the constitutive law in bending or torsion. The proposed method uses deformation data as an input to estimate the corresponding restoring forces and moments based on Kirchhoff rod theory [83]. Configurational data in general can be obtained from discrete-structure simulations (or, from other types of simulations, such as MD simulations, for example) to derive the constitutive law of

a filament. However, in this chapter I synthesized the data using the forward rod model developed in Chapter 3. In particular, Section 4.2 illustrates how to use the configuration data of a dynamic simulation to identify the bending constitutive law of an artificial filament. After evaluating the performance of several numerical schemes in Section 4.3, I benchmarked the constitutive law that is derived by applying it to different loading conditions in Section 4.4. Next, in Section 4.5, I present all viable algorithms of the inverse approach and analyze the performance and robustness of various algorithms conceivable in the inverse approach presented in this chapter. Section 4.5.5 investigates the robustness of the inverse approach algorithms by adding noise to the inputs and finally, Section 4.6 draws conclusions on the performance of algorithms based on the results and robustness analysis.

4.2 The Algorithm of Inverse Approach

The inverse approach conceptualized here, in general, is a method to find the functions ψ_i in Eq. (3.6) using the geometric data that specify the deformation of the filament. The deformation of the filament, i.e. $\vec{\kappa}$ and $\vec{r}$, as well as the other kinematic quantities $\vec{v}$ and $\vec{\omega}$ can, in principle, be obtained, for example, from the time series of atomic positions extracted from molecular dynamics simulations. Using kinematic quantities as input variables, the inverse approach presented here leverages the forward model, Eqs. (3.1) to (3.4) to estimate the restoring forces and moments. Depending on which of the kinematic variables can be obtained reliably from the position data, the steps of the inverse method algorithm will vary.

Figure 4.1 outlines the steps involved in one such inverse approach algorithm that uses only $\vec{\kappa}$ and $\vec{r}$ as input. In step 1, the angular velocity $\vec{\omega}$ is calculated, via Eq. (C1), from the input $\vec{\kappa}$ values. Eq. (C2) of the step 2 is used to solve for the velocity using the input $\vec{\kappa}$ and $\vec{r}$ values as well as the angular velocity $\vec{\omega}$ values determined in step 1. The step 3 uses Eq. (E1) to derive the internal force $\vec{f}$ from the input $\vec{\kappa}$, and $\vec{\omega}$ and $\vec{v}$ values, obtained in step 1 and 2 respectively. Finally, in step 4 the internal moment $\vec{q}$ is derived using Eq. (E2) from the values of $\vec{\kappa}$, $\vec{r}$, $\vec{f}$, and $\vec{\omega}$ calculated in the previous steps. Once all of these steps are completed I have, on one hand the strain information in the form of $\vec{\kappa}$ and $\vec{r}$, and on the other hand the restoring forces and moments, $\vec{f}$ and $\vec{q}$. Using this data I can derive the constitutive law in the form of an algebraic relationship, for example as a polynomial function, by an appropriate fitting procedure.

The inverse approach proposed here, requires both numerical integration as well as numerical differentiation. For example, all the steps of the algorithm outlined in Figure 4.1 involves numerical differentiation in time, t, and numerical integration along the spatial coordinate, s using the boundary conditions. So, the inverse approach is vulnerable to integration error compounded with the noise amplification due to numerical differentiation, and is, therefore expected to be very sensitive to the choice of numerical scheme. I tested several numerical schemes implementing the algorithm presented in

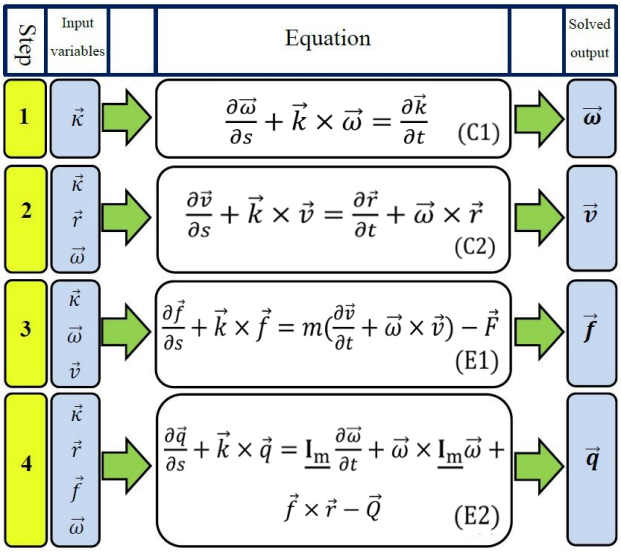

Figure 4.1: Rod model equations and solution procedure in the inverse approach to solve rod model equations with input deformation data for four unknowns namely $\vec{\omega}$, $\vec{v}$, $\vec{f}$ and $\vec{q}$.

Figure 4.1. Next section presents and compares a case study with three representative numerical schemes.

Note that depending on the choice of input kinematic variables, other conceivable algorithms may have steps that involve numerical differentiation in space, and numerical integration in time using initial conditions. Nevertheless, in general, to keep the algorithm fast and simple to implement, the preference would be to have explicit scheme for numerical integration, but can have implicit scheme for numerical differentiation. The first and second schemes presented in the next section adopt this simplicity.

Note also that cantilever loading allows the spatial integration to proceed as an initial value problem (IVP) taking advantage of the explicit integration scheme. In particular, Eqs. (C1) and (C2) can be integrated in a single shot from clamped end towards the free end using only the clamped end boundary conditions, while Eqs. (E1) and (E2) can be integrated in a single shot from the free end towards to the clamped end using only the free end boundary conditions.

4.3 Comparing Different Finite Differences Schemes For The Inverse Approach

4.3.1 Simulation Case Studies

In the following three sections, different finite difference approaches are applied to the inverse algorithm which is illustrated in the Figure 4.1. At each of the steps shown in the figure the calculated output quantity is tracked to evaluate the performance of the

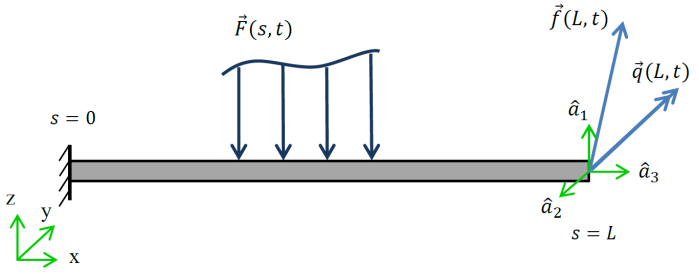

Figure 4.2: Schematic diagram of the cantilever beam with length $L = 1$ m, mass per unit length, $m = 9.8$ kg/m, and the moment of inertia per unit length, $\mathbf{I_m}(s)$ that corresponds to a uniform circular cross-section with the diameter, $d = 0.0141$ m. In Section 4.3, the filament is bent in x-z plane by applying the shear force, $\vec{f}(L,t) = 20000\hat{a}_1$ to the free end while distributed load, $\vec{F}$ and moment at free end, $\vec{q}(L,t)$ are zero. In Section 4.5.4, the filament is bent in x-z plane by applying either the bending moment, $q_2(L,t)$ or the shear force, $f_1(L,t)$ to the free end, but no distributed load.

numerical scheme. The input curvature data is obtained from the planar bending simulation of an artificial filament modeled as a cantilever beam. Figure 4.2 shows a schematic representation of a cantilever beam. The shear force on the free end, $\vec{f}(L,t)$ is applied as a step function in time and is described in body-fixed frame in the positive $\hat{a}_1$ direction. The other external forces and moments are zero in this simulation. The dynamic response of the filament is found by computational forward rod model with the constitutive law provided in Eq. (4.1) as an algebraic constraint.

$$q_2 = 30\kappa_2^5 - 600\kappa_2^3 + 10000\kappa_2. \tag{4.1}$$

Figure 4.3 shows the snapshots of the in-plane bending of the filament subjected to the shear force, $\vec{f}(L,t) = 20000\hat{a}_1$.

4.3.2 First Discretization Scheme

The inverse algorithm that is presented in Figure 4.1 is done through four steps. Each step involves temporal differentiation and spatial integration to compute the desired quantity. Here, finite differences are used to discretize the equations. In the first scheme the temporal derivatives are approximated by second order central difference formula. The spatial derivatives in Eqs. (C1) and (C2) are discretized by backward difference formula to use the boundary values of the $\vec{v}$ and $\vec{\omega}$ at the fixed end and initiate the spatial integration. In all of the following equations, the indices i and j are enumerating the time-steps and space-steps, respectively. Both temporal and spatial grids are uniform and are

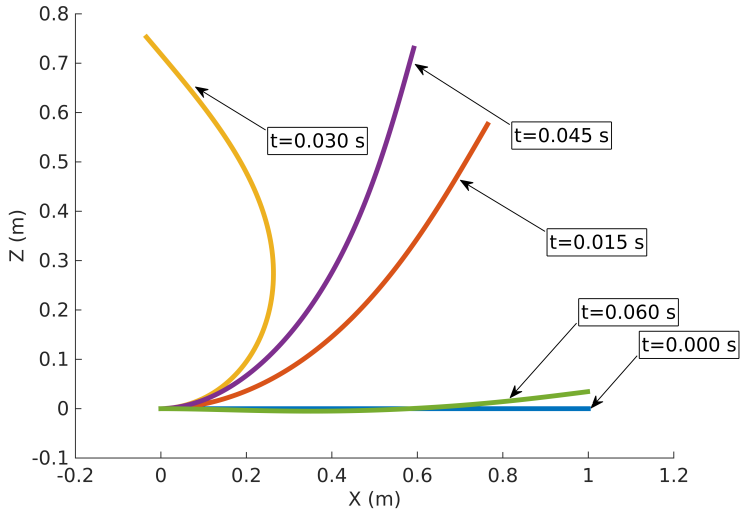

Figure 4.3: Snapshots of the shape of the filament in response to the step shear force simulated by the forward rod model.

described by step sizes, Δt and Δs, respectively. The magnitudes of both time-step and space-step are equal to those used in the forward simulations. The 3-by-3 identity matrix is denoted by $\underline{\mathbf{I_d}}$, and the the skew-symmetric matrix corresponding to the curvature vector, $\vec{\kappa}$ is represents by $\tilde{\kappa}$. Hence, the discretized form of the Eqs. (C1) and (C2) is derived as follows.

$$(\underline{\mathbf{I_d}} + \Delta s\tilde{\kappa}_{i,j})\vec{\omega}_{i,j} = \vec{\omega}_{i,j-1} + \Delta s\Big(\frac{\vec{\kappa}_{i+1,j} - \vec{\kappa}_{i-1,j}}{2\Delta t}\Big) \tag{4.2}$$

$$(\underline{\mathbf{I_d}} + \Delta s\tilde{\kappa}_{i,j})\vec{v}_{i,j} = \vec{v}_{i,j-1} + \Delta s\big(\vec{\omega}_{i,j} \times \vec{r}_{i,j}\big) \tag{4.3}$$

The boundary condition for the internal force and internal moment are known at the free end of the filament. Therefore the forward difference formula is used to approximate the spatial derivative in the Eqs. (E1) and (E2).

$$(\underline{\mathbf{I_d}} - \Delta s\tilde{\kappa}_{i,j})\vec{f}_{i,j} = \vec{f}_{i,j+1} - m\Delta s\Big(\frac{\vec{v}_{i+1,j} - \vec{v}_{i-1,j}}{2\Delta t} + \vec{\omega}_{i,j} \times \vec{v}_{i,j}\Big) \tag{4.4}$$

$$(\underline{\mathbf{I_d}} - \Delta s\tilde{\kappa}_{i,j})\vec{q}_{i,j} = \vec{q}_{i,j+1} - \Delta s\underline{\mathbf{I_m}}\Big(\frac{\vec{\omega}_{i+1,j} - \vec{\omega}_{i-1,j}}{2\Delta t}\Big) - \Delta s\big(\vec{\omega}_{i,j} \times (\underline{\mathbf{I_m}}\vec{\omega}_{i,j}) + \vec{f}_{i,j} \times \vec{r}_{i,j}\big) \tag{4.5}$$

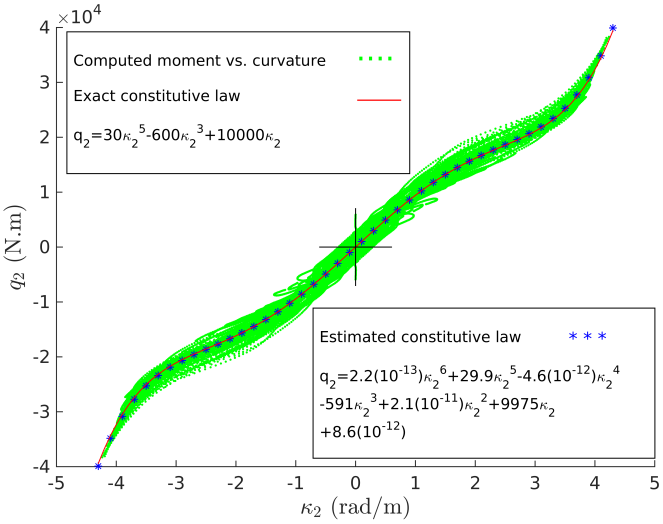

Figure 4.4: Internal moment that is calculated by inverse method versus input curvature data for the first discretization scheme. The red line shows the exact constitutive law, while the asterisks are showing the estimated constitutive law that is found by least-squares fitting.

The values of the internal moments that are estimated by the inverse method are then plotted against curvature values. The least-squares function fitting is used to estimate the relationship between restoring moment and curvature. In the Figure 4.4 the exact constitutive law is shown by red line and the estimated constitutive law with the asterisks. This figure includes the data for the loading scenario that is described in previous subsection in addition to the data where the filament is bent about the opposite direction by applying a shear force of same magnitude to the free end, in the negative $\hat{a}_1$ direction.

4.3.3 Second Discretization Scheme

In this section, temporal derivatives are discretized by forth order central difference formula. The spatial derivatives in Eqs. (C1) and (C2) are discretized by backward difference formula and thus integrated in space from fixed end $(j=0)$ where the boundary conditions are known for angular velocity, $\vec{\omega}(L,t)$ and linear velocity $\vec{v}(L,t)$. Therefore, using discretized forms of Eqs. (C1) and (C2), given below, values of $\vec{\omega}$ and $\vec{v}$ are obtained.

$$(\underline{\mathbf{I_d}} + \Delta s\tilde{\kappa}_{i,j})\vec{\omega}_{i,j} = \vec{\omega}_{i,j-1} + \Delta s\Big(\frac{-\vec{\kappa}_{i+2,j} + 8\vec{\kappa}_{i+1,j} - 8\vec{\kappa}_{i-1,j} + \vec{\kappa}_{i-2,j}}{12\Delta t}\Big) \tag{4.6}$$

$$(\underline{\mathbf{I_d}} + \Delta s\tilde{\kappa}_{i,j})\vec{v}_{i,j} = \vec{v}_{i,j-1} + \Delta s\big(\vec{\omega}_{i,j} \times \vec{r}_{i,j}\big) \tag{4.7}$$

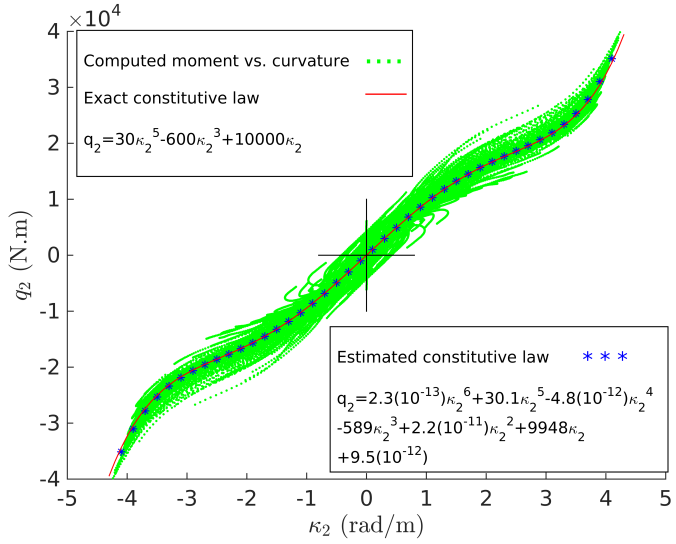

Figure 4.5: Internal moment that is calculated by inverse method versus input curvature data for the second discretization scheme. The red line shows the exact constitutive law, while the asterisks are showing the estimated constitutive law that is found by least-square fitting.

The temporal derivatives in Eqs. (E1) and (E2) are discretized with the same numerical method as Eqs. (4.6) and (4.7). However, since the boundary condition for internal force $\vec{f}$ and internal moment $\vec{q}$ are known at the free end of the cantilever $(j = 31)$, a forward difference formula is used for spatial discretization. Therefore, Eqs. (4.8) and (4.9) are integrated backward in space from last cross-section $(j = 31)$ toward the first one $(j = 1)$ and solved for internal force, $\vec{f}$ and internal moment, $\vec{q}$ as follows.

$$(\underline{\mathbf{I_d}} - \Delta s\tilde{\kappa}_{i,j})\vec{f}_{i,j} = \vec{f}_{i,j+1} - m\Delta s\big(\vec{\omega}_{i,j} \times \vec{v}_{i,j} + \frac{-\vec{v}_{i+2,j} + 8\vec{v}_{i+1,j} - 8\vec{v}_{i-1,j} + \vec{v}_{i-2,j}}{12\Delta t}\big) \quad (4.8)$$

$$(\underline{\mathbf{I_d}} - \Delta s\tilde{\kappa}_{i,j})\vec{q}_{i,j} = \vec{q}_{i,j+1} - \Delta s\underline{\mathbf{I_m}}\big(\frac{-\vec{\omega}_{i+2,j} + 8\vec{\omega}_{i+1,j} - 8\vec{\omega}_{i-1,j} + \vec{\omega}_{i-2,j}}{12\Delta t}\big) - \Delta s\big(\vec{\omega}_{i,j} \times (\underline{\mathbf{I_m}}\vec{\omega}_{i,j}) + \vec{f}_{i,j} \times \vec{r}_{i,j}\big) \quad (4.9)$$

The computed internal moments, the exact constitute law, estimated constitutive laws via this formulation are illustrated in Figure 4.5.

4.3.4 Third Discretization Scheme

Another finite difference scheme that is frequently used to discretize the partial differential equations in both space and time is box method [84]. The unknown vectors in the rod model equations can be assembled into a matrix as shown below.

$$Y = \begin{bmatrix} \vec{\omega} \\ \vec{v} \\ \vec{f} \\ \vec{q} \end{bmatrix} \tag{4.10}$$

Therefore, the set of four differential equations can be represented as

$$M\dot{Y} + KY' + F = 0 \tag{4.11}$$

where $\dot{Y}$ and Y' are partial derivatives of the matrix Y in time and space, respectively. Matrices M and K are coefficients and F contains non-homogeneous terms. Figure 4.6 shows the stencil for the box method scheme and the grid points that are used in space and time averaging are highlighted. Applying the box method to discretize the system of equations represented in Eq. (4.11) will result in the following.

$$\begin{aligned}(M_{i,j} + M_{i-1,j})(\frac{Y_{i,j} + Y_{i-1,j}}{\Delta t}) + (M_{i,j-1} + M_{i-1,j-1})(\frac{Y_{i,j-1} + Y_{i-1,j-1}}{\Delta t}) + \\ (K_{i,j} + K_{i,j-1})(\frac{Y_{i,j} + Y_{i,j-1}}{\Delta s}) + (K_{i-1,j} + K_{i-1,j-1})(\frac{Y_{i-1,j} + Y_{i-1,j-1}}{\Delta s}) + \\ (F_{i,j} + F_{i-1,j} + F_{i,j-1} + F_{i-1,j-1}) = 0\end{aligned} \tag{4.12}$$

Hence, discretized form of the Eq. (C1) by box method can be retrieved as given below.

$$\begin{aligned}(\underline{\mathbf{I_d}} + \underline{\mathbf{I_d}})(\frac{\vec{\omega}_{i,j} - \vec{\omega}_{i,j-1}}{\Delta s}) + (\underline{\mathbf{I_d}} + \underline{\mathbf{I_d}})(\frac{\vec{\omega}_{i-1,j} - \vec{\omega}_{i-1,j-1}}{\Delta s}) \\ - (\underline{\mathbf{I_d}} + \underline{\mathbf{I_d}})(\frac{\vec{\kappa}_{i,j} - \vec{\kappa}_{i-1,j}}{\Delta t}) - (\underline{\mathbf{I_d}} + \underline{\mathbf{I_d}})(\frac{\vec{\kappa}_{i,j-1} - \vec{\kappa}_{i-1,j-1}}{\Delta t}) \\ + \big(\vec{\kappa}_{i,j} \times \vec{\omega}_{i,j} + \vec{\kappa}_{i,j-1} \times \vec{\omega}_{i,j-1} + \vec{\kappa}_{i-1,j} \times \vec{\omega}_{i-1,j} + \\ \vec{\kappa}_{i-1,j-1} \times \vec{\omega}_{i-1,j-1}\big) = 0\end{aligned} \tag{4.13}$$

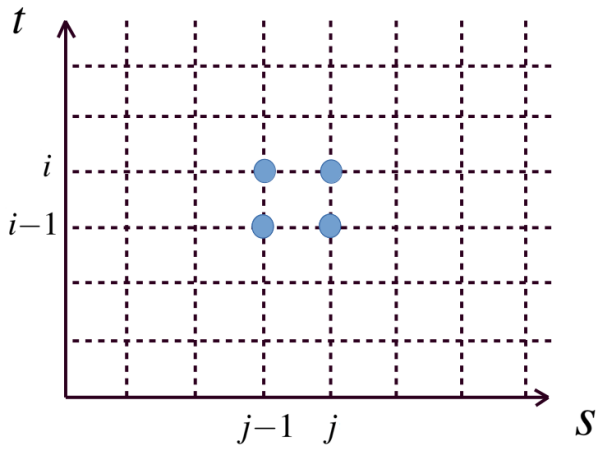

Figure 4.6: Temporal and spatial grid points corresponding to the box method. Blue circles in the figure represent the four nodes that are used for discretization.

The terms are rearranged to obtain the following explicit expression for the unknown.

$$\begin{aligned}(2\underline{\mathbf{I_d}}+\Delta s\tilde{\kappa}_{i,j})(\vec{\omega}_{i,j}) = 2(\vec{\omega}_{i,j-1}-\vec{\omega}_{i-1,j}+\vec{\omega}_{i-1,j-1}) \\ +2\Delta s\Big(\frac{\vec{\kappa}_{i,j}-\vec{\kappa}_{i-1,j}}{\Delta t}+\frac{\vec{\kappa}_{i,j-1}-\vec{\kappa}_{i-1,j-1}}{\Delta t}\Big) \\ -\Delta s\big(\vec{\kappa}_{i,j-1}\times\vec{\omega}_{i,j-1}+\vec{\kappa}_{i-1,j}\times\vec{\omega}_{i-1,j}+ \\ \vec{\kappa}_{i-1,j-1}\times\vec{\omega}_{i-1,j-1}\big) \quad (4.14)\end{aligned}$$

In Figure 4.7 the results of the angular velocity about $\hat{a}_2$ direction that are computed by Eq. (4.14) is plotted, as well as the exact values of the angular velocity that are simulated by forward rod model. Same approach is employed to discretize the rest of the rod model equations. Equation (4.15) shows the discretized form of the Eq. (C2) with the box method.

$$\begin{aligned}(2\underline{\mathbf{I_d}}+\Delta s\tilde{\kappa}_{i,j})(\vec{v}_{i,j}) = 2(\vec{v}_{i,j-1}-\vec{v}_{i-1,j}+\vec{v}_{i-1,j-1}) \\ -\Delta s\big(\vec{\kappa}_{i,j-1}\times\vec{v}_{i,j-1}+\vec{\kappa}_{i-1,j}\times\vec{v}_{i-1,j}+ \\ \vec{\kappa}_{i-1,j-1}\times\vec{v}_{i-1,j-1}\big)+\Delta s\big(\vec{\omega}_{i,j}\times\vec{r}_{i,j}+\vec{\omega}_{i,j-1}\times\vec{r}_{i,j-1}+ \\ \vec{\omega}_{i-1,j}\times\vec{r}_{i-1,j}+\vec{\omega}_{i-1,j-1}\times\vec{r}_{i-1,j-1}\big) \quad (4.15)\end{aligned}$$

The linear velocity in the $\hat{a}_1$ direction is also compared to its exact values as depicted in Figure 4.8 and shows a close match. Likewise, Eqs. (E1) and (E2) are discretized as follows.

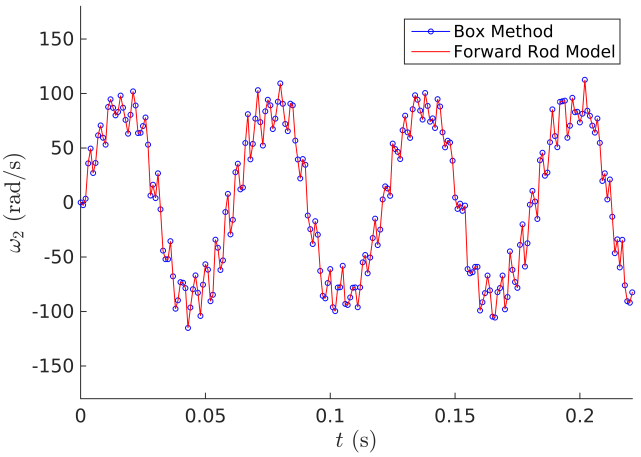

Figure 4.7: The angular velocity of the mid-length cross-section of the filament $(s = \frac{L}{2})$ computed by box method discretization is compared with the exact values of the input data that is simulated by forward rod model.

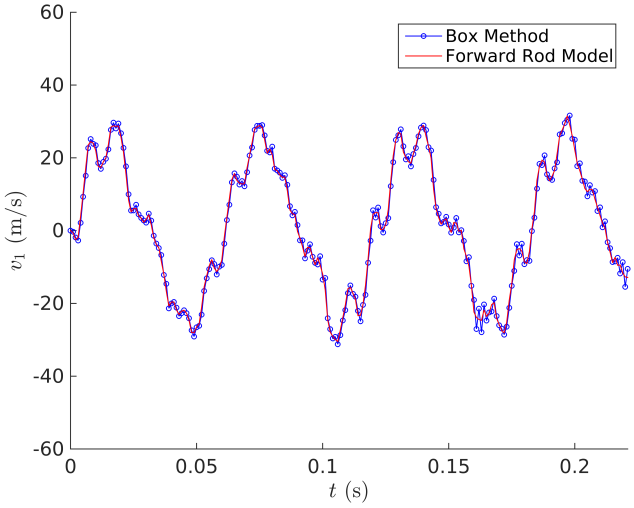

Figure 4.8: The linear velocity of the mid-length cross-section of the filament $(s = \frac{L}{2})$ computed by box method discretization is compared with the exact values of the input data that is simulated by forward rod model.

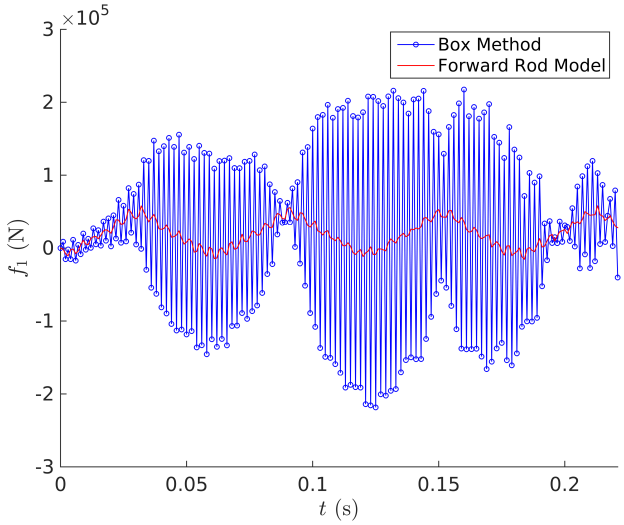

Figure 4.9: The internal force at the mid-length cross-section of the filament $(s = \frac{L}{2})$ computed by box method discretization is compared with the exact values of the input data that is simulated by forward rod model.

$$
\begin{aligned}
(2\underline{\mathbf{I_d}} - \Delta s\tilde{\kappa}_{i,j-1})(\vec{f}_{i,j-1}) = 2(\vec{f}_{i,j} + \vec{f}_{i-1,j} - \vec{f}_{i-1,j-1}) \\
- 2m\Delta s\Big(\frac{\vec{v}_{i,j} - \vec{v}_{i-1,j}}{\Delta t} + \frac{\vec{v}_{i,j-1} - \vec{v}_{i-1,j-1}}{\Delta t}\Big) \\
+ \Delta s\big(\vec{\kappa}_{i,j} \times \vec{f}_{i,j} + \vec{\kappa}_{i-1,j} \times \vec{f}_{i-1,j} + \\
\vec{\kappa}_{i-1,j-1} \times \vec{f}_{i-1,j-1}\big) - m\Delta s\big(\vec{\omega}_{i,j} \times \vec{v}_{i,j} + \vec{\omega}_{i,j-1} \times \vec{v}_{i,j-1} + \\
\vec{\omega}_{i-1,j} \times \vec{v}_{i-1,j} + \vec{\omega}_{i-1,j-1} \times \vec{v}_{i-1,j-1}\big) \quad (4.16)
\end{aligned}
$$

Eq. (4.16) in combination to the quantities from previous steps are used to compute the internal force. As can be seen in Figure 4.9 the internal forces in the $\hat{a}_1$ direction are oscillating about the true solution which in this case is known from the forward rod model simulation. Thus, the box method discretization for computation of the internal forces is not converging and showing the crank-nicolson noise in time.

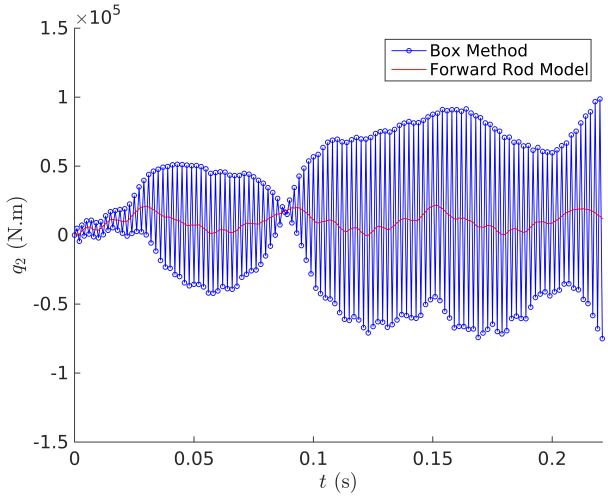

Figure 4.10: The internal moment at the mid-length cross-section of the filament $(s = \frac{L}{2})$ computed by box method discretization is compared with the exact values of the input data that is simulated by forward rod model.

$$
\begin{aligned}
(2\underline{\mathbf{I_d}} - \Delta s\tilde{\kappa}_{i,j-1})(\vec{q}_{i,j-1}) = 2(\vec{q}_{i,j} + \vec{q}_{i-1,j} - \vec{q}_{i-1,j-1}) \\
- 2\Delta s\underline{\mathbf{I_m}}\Big(\frac{\vec{\omega}_{i,j} - \vec{\omega}_{i-1,j}}{\Delta t} + \frac{\vec{\omega}_{i,j-1} - \vec{\omega}_{i-1,j-1}}{\Delta t}\Big) \\
+ \Delta s\big(\vec{\kappa}_{i,j} \times \vec{q}_{i,j} + \vec{\kappa}_{i-1,j} \times \vec{q}_{i-1,j} + \\
\vec{\kappa}_{i-1,j-1} \times \vec{q}_{i-1,j-1}\big) - \Delta s\big(\vec{\omega}_{i,j} \times (\underline{\mathbf{I_m}}\vec{\omega}_{i,j}) + \vec{\omega}_{i,j-1} \times (\underline{\mathbf{I_m}}\vec{\omega}_{i,j-1}) + \\
\vec{\omega}_{i-1,j} \times (\underline{\mathbf{I_m}}\vec{\omega}_{i-1,j}) + \vec{\omega}_{i-1,j-1} \times (\underline{\mathbf{I_m}}\vec{\omega}_{i-1,j-1})\big) \\
- \Delta s\big(\vec{f}_{i,j} \times \vec{r}_{i,j} + \vec{f}_{i,j-1} \times \vec{r}_{i,j-1} + \vec{f}_{i-1,j} \times \vec{r}_{i-1,j} + \\
\vec{f}_{i-1,j-1} \times \vec{r}_{i-1,j-1}\big) \quad (4.17)
\end{aligned}
$$

The internal forces are also used in computation of the internal moments by Eq. (4.17), therefore, the solution is not converged and shows the crank-nicolson noise in time as illustrated in Figure 4.10.

4.4 Validation

Among the three numerical schemes that are implemented in previous section, the first one is proved to be the most efficient and effective. It has the simplest formulation, yet, from Figures 4.4 and 4.5 it can be inferred that the first scheme is more accurate than the second one in estimation of the internal moments and, therefore, of the constitutive law. Here, an alternative loading scenario is defined in order to test how the estimated

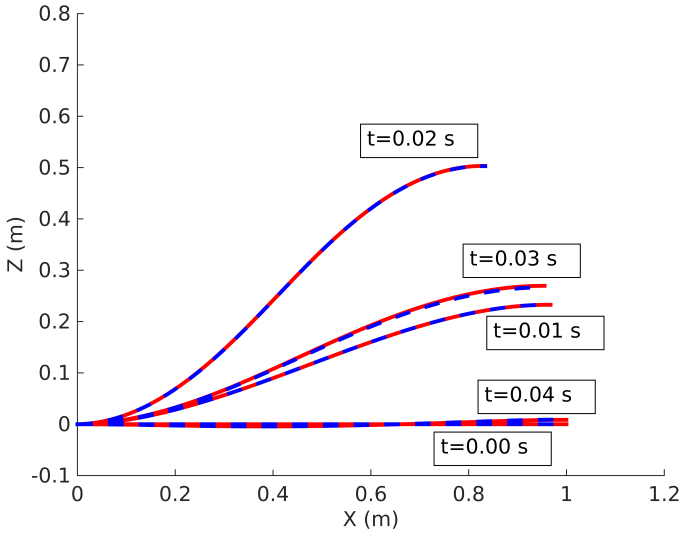

Figure 4.11: Shape of the rod simulated by the exact constitutive law and shown with the solid red line. The dashed blue line as also shape of the rod that is found by the estimated constitutive law.

constitutive law is capturing the dynamics of the filament in comparison to the original constitutive law. A shear force is applied to the free end of the filament, $f(L,t) = 30000\hat{a}_1$ as a step function in time while its angular velocity is constrained to be zero, $\vec{\omega}(L,t) = \vec{0}$. Figure 4.11 illustrates several snapshots of the shape of the filament as time elapses. The response of the filament with the reconstructed constitutive law is in close agreement with the response of the filament obtained by its original constitutive law as time evolves.

4.5 Robustness Analysis

4.5.1 Algorithmic Formulation

Depending on which of the four kinematic variables $\vec{\kappa}$, $\vec{r}$, $\vec{v}$ and $\vec{\omega}$ can be obtained reliably from the position data, the steps of the inverse method algorithm will vary. Figure 4.1 outlines the steps involved in one such inverse method algorithm that uses only $\vec{\kappa}$ and $\vec{r}$ as known inputs. In this scenario, step 1 uses Eq. (C1) to solve for the angular velocity $\vec{\omega}$ substituting the known input $\vec{\kappa}$. Step 2 uses Eq. (C2) to solve for the velocity $\vec{v}$ substituting the known inputs $\vec{\kappa}$ and $\vec{r}$ as well as the angular velocity $\vec{\omega}$ obtained from step 1. Step 3 uses Eq. (E1) to solve for the internal force $\vec{f}$ substituting the input $\vec{\kappa}$ as well as $\vec{\omega}$ and $\vec{v}$ obtained in step 1 and 2 respectively. Finally, step 4 uses Eq. (E2) to solve for the internal moment $\vec{q}$ substituting the inputs $\vec{\kappa}$ and $\vec{r}$ as well as $\vec{f}$ and $\vec{\omega}$ obtained from

Table 4.1: Viable Inverse Algorithms

	Measured kinematic variables	Steps of inverse algorithm
1	$\vec{\kappa}$	1, 2, 3, 4
2	$\vec{\omega}$	1 (inverted), 2, 3, 4
3	$\vec{\kappa}$, $\vec{\omega}$	2, 3, 4
4	$\vec{\kappa}$, $\vec{v}$	1, 3, 4
5	$\vec{v}$, $\vec{\omega}$	1(inverted), 3, 4
6	$\vec{\kappa}$, $\vec{v}$, $\vec{\omega}$	3, 4

the previous steps. The steps 3 and 4 assume that the distributed force, $\vec{F}(s,t)$ and moment, $\vec{Q}(s,t)$, if nonzero, are known, so are the boundary values of $\vec{f}$ and $\vec{q}$ at one of the two boundaries to provide for the constants of the spatial integrations. A 2-dimensional version of this algorithm without distributed force and moment was proposed by [85].

Once all of these steps are completed, we have, on one hand the strain information in the form of the deformations $\vec{\kappa}(s,t)$ and $\vec{r}(s,t)$, and on the other hand the restoring force and moment, $\vec{f}(s,t)$ and $\vec{q}(s,t)$ for all values of s and t. Using this data we can derive the constitutive law in the form of an algebraic relationship by an appropriate fitting procedure.

When extension and shear are negligible, the configurational data will yield $\vec{r}$ to be constant with respect to $\hat{a}_i$, and only the other three kinematic variables $\vec{\kappa}$, $\vec{v}$ and $\vec{\omega}$ will have the physically useful information for estimating $\vec{f}$ and $\vec{q}$. Table 4.1 lists all of the combinations of these three kinematic variables and corresponding steps of the inverse method algorithms for estimating $\vec{f}$ and $\vec{q}$. For options 2 and 5, it may be tempting to consider using step 2 (Eq. (C2)) in place of step 1 (Eq. (C1)) as a viable alternative. However, solving for either $\vec{\omega}$ or $\vec{\kappa}$ from Eq. (C2) is ill-posed because they appear in Eq. (C2) only in the cross-product terms. In other words, solving for any vector $\vec{u}$ from $\vec{u} \times \vec{a} = \vec{b}$ with vectors $\vec{a}$ and $\vec{b}$ given, is an ill-posed problem that has infinite solutions. For the same reason, the option of using $\vec{v}$ alone as input with steps 1 & 2 (coupled), 3, 4, is not viable because Eq. (C2) does not provide for independent three scalar equations for $\vec{\omega}$ and $\vec{\kappa}$ due to the cross-products. Not surprisingly, $\vec{v}$ has information on the centerline, but not on the twist of the filament; consider, for example, a case of pure twist in which full knowledge of linear velocity, $\vec{v}$ does not provide any information on the mechanical response of the rod. Table 4.1 lists only the well-posed choices.

Not all of the options of inverse algorithms listed in Table 4.1 are expected to be equally well-conditioned. Section 4.5.4 tests these algorithms in two different loading scenarios for data generated from forward rod model simulation employing a nonlinear constitutive law, and Section 4.5.5 analyzes their robustness.

4.5.2 Numerical Discretization

The inverse approach is more susceptible to ill-conditioning than the forward model because unlike the forward model, the inverse algorithm requires not only numerical integration but also numerical differentiation, which tends to be ill-conditioned with finite differencing approach [86]. In particular, each of the steps 1, 3 and 4 involves numerical differentiation in time t, and numerical integration along the spatial coordinate s. Step 2 involves numerical integration along the spatial coordinate, s, and if there is shear or extension, it also has a non-trivial timporal derivative. Step 1 (inverted) involves numerical differentiation in s and integration in t. So, all the options of inverse algorithms listed in Table 4.1 are vulnerable to integration error compounded with the noise amplification due to numerical differentiation, and are very sensitive to the choice of numerical difference schemes. Several space-time discretization schemes are applied to this inverse problem [87] and found that while sophisticated schemes such as box method [84] tend to fail, a rather simple scheme that uses second order central differencing for approximating numerical differentiation and forward or backward Euler differencing for numerical integration, surprisingly worked well. So, we adopt the same scheme for the simulations in Section 4.5.4.

4.5.3 Initial and Boundary Conditions

Forward rod model needs twelve initial conditions and twelve boundary conditions (six at each end). However, inverse approach does not require the full set of initial and boundary conditions. To be well-posed, steps 1 through 4 require knowledge of $\vec{\omega}$, $\vec{v}$, $\vec{f}$ and $\vec{q}$ respectively, each at either one of the two ends to integrate towards the other end simply as an initial value problem (IVP) in the spatial coordinate, s [64]. Steps 1 through 4 do not require knowledge of initial conditions. Step 1 (inverted) require only the initial condition for $\vec{\kappa}$.

4.5.4 Comparing Different Algorithms

This section compares the performance of the family of inverse algorithms listed in Table 4.1 using input data obtained by simulating planar bending of a cantilever illustrated in Figure 4.2, with the forward rod model described in previous chapter. All the quantities are in SI units. Without loss of any generality, the cross-section fixed vector $\hat{a}_2$ is aligned with the bending axis. The extension and shear are ignored, and the constitutive law chosen is nonlinear and decoupled along $\hat{a}_2$ as

$$q_2 = 30\kappa_2^5 - 600\kappa_2^3 + 10000\kappa_2. \tag{4.18}$$

The inverse algorithms are tested with the dynamic response of the cantilever simulated in two different loading scenarios:

Loading Scenario 1: A pure bending moment, $q_2(L,t)$ is applied at the free end that results in sinusoidal variation in the curvature at the free end $\kappa_2(L,t) = 4sin(10\pi t)$.

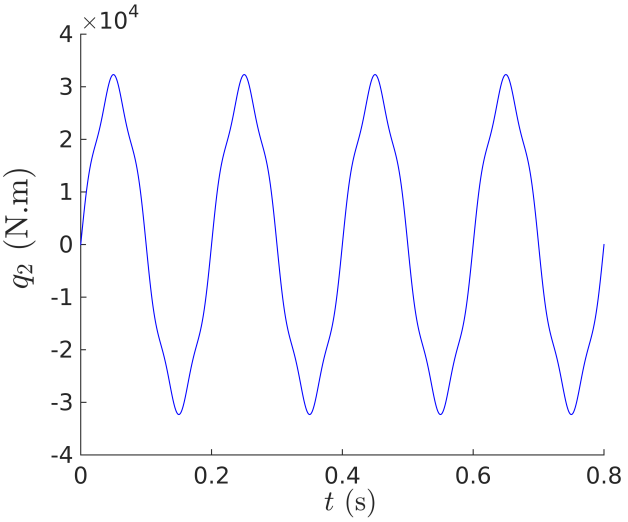

Figure 4.12: Loading scenario 1: bending moment $q_2(L,t) = 30720sin^5(10\pi t) - 38400sin^3(10\pi t) + 40000sin(10\pi t)$ resulting in a sinusoidal curvature, $\kappa_2(L,t) = 4sin(10\pi t)$.

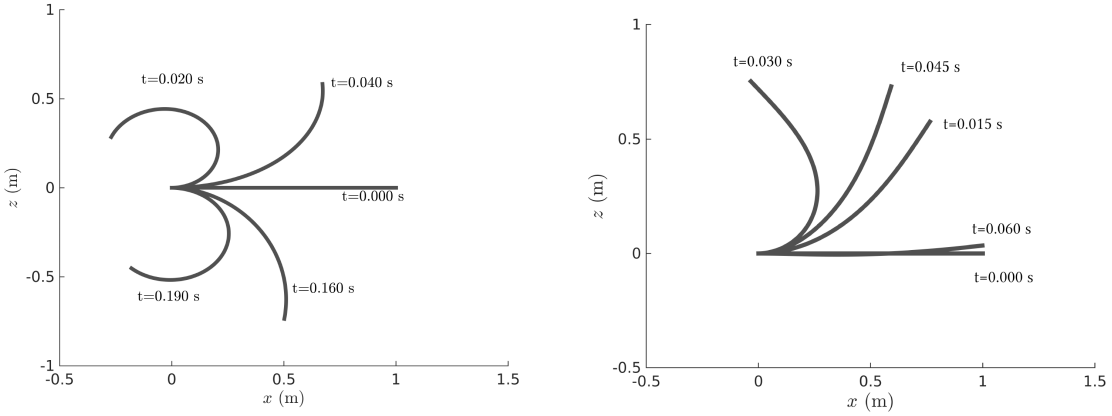

(a) Loading scenario 1 (pure bending moment).

(b) Loading scenario 2 (pure shear force).

Figure 4.13: Simulation snapshots of the cantilever deformation.

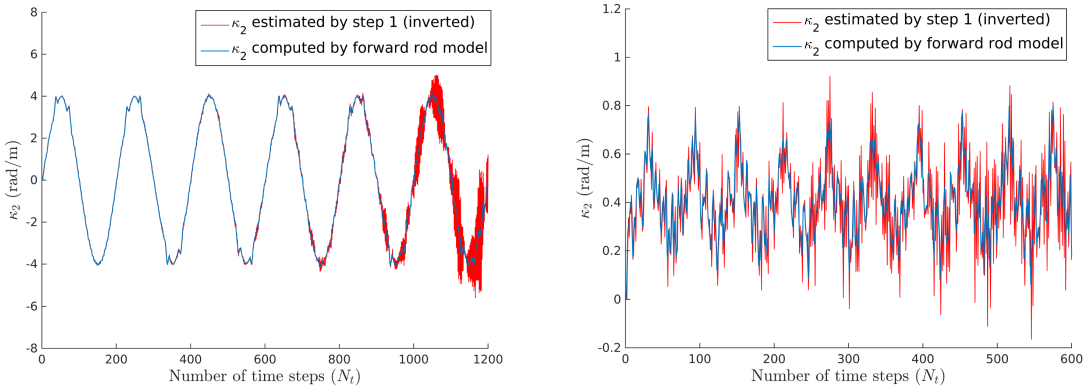

(a) Loading scenario 1 (pure bending moment).

(b) Loading scenario 2 (pure shear force).

Figure 4.14: Curvature $\vec{\kappa}(s = 0.8L, t)$ estimated from $\vec{\omega}$ using Eq. (C1) (step 1 (inverted)) and compared with that computed from the forward model.

The bending moment at the free end, $q_2(L,t)$ is plotted as a function of time in Figure 4.12. A few snapshots of the simulated cantilever deformation are shown in Figure 4.13(a).

Loading Scenario 2: A pure shear force is exerted at the free end as a step function in time $f_1(L,t) = 20000$. A few snapshots of the simulated step response are shown in Figure 4.13(b). The simulations are repeated with the loading in opposite direction, $f_1(L,t) = -20000$ to obtain deformations in a wider range.

The forward model simulation computes all the kinematic variables $\vec{v}(s,t), \vec{\omega}(s,t)$ and $\vec{\kappa}(s,t)$ as well as the restoring force, $\vec{f}(s,t)$ and moment, $\vec{q}(s,t)$. However, The inverse model simulation uses only the kinematic variables required as input for each algorithm listed in Table 4.1 to estimate the restoring force, $\vec{f}(s,t)$ and moment, $\vec{q}(s,t)$.

To begin, consider the estimation with input $\vec{\omega}$ alone or $\vec{\omega}$ and $\vec{v}$ (options 2 or 5 in Table 4.1). Both algorithms begin with step 1 (inverted), in which $\vec{\kappa}$ is integrated in time using forward Euler differencing starting with its initial value. The spatial derivative of $\vec{\omega}$ is approximated by second order central differencing. Figure 4.14(a) and (b) compare the estimated $\vec{\kappa}$ (red curve) at a sample cross-section at $s = 0.8L$ with that computed from the forward model (blue curve) for loading scenarios 1 and 2 respectively. As the integration of $\vec{\kappa}$ marches in time, the error grows rapidly with the compounding effect of noise amplification due to numerical differentiation of $\vec{\omega}$ in s. This error growth renders the algorithms worthless. In fact, in the limit of quasi-static deformation, the kinematic variables $\vec{v}$ and $\vec{\omega}$ will be zero, and the inverse algorithms that rely only on these kinematic variables, will obviously be ill-posed and lacking sufficient information to estimate restoring effects. So, one may intuitively expect that unless the dynamics are reasonably fast, these algorithms will indeed tend to be very ill-conditioned. These algorithms

may be better conditioned if $\vec{\kappa}$ is measured even at intermittent time values to reset the accumulated error to zero.

The remaining options (1,3,4 and 6) in Table 4.1 do have $\vec{\kappa}$ as input that we now recognize is crucial for estimation. The remaining options require all or a subset of the four steps from 1 through 4 outlined in Figure 4.1. Each of these four steps involves integration along s. In steps 1 and 2, $\vec{\omega}$ and $\vec{v}$ are integrated using forward Euler differencing starting with their known values at the clamped end ($s = 0$). For steps 3 and 4, $\vec{f}$ and $\vec{q}$ are known at the free end ($s = L$), and therefore they are integrated back towards the clamped end using backward Euler differencing, which, in this case, is an explicit integration scheme. The temporal derivatives in Steps 1, 3 and 4 are approximated by second order central differencing. Since there is no integration in time, no initial conditions are required.

Figure 4.15 shows the results of each of the four remaining options (1,3,4 and 6) of inverse algorithm for both loading scenarios. The first column represents the results of loading scenario 1 (pure bending moment), while the second column represents the results of loading scenario 2 (pure shear force). The first row corresponds to option 1 ($\vec{\kappa}$ alone as input), the second row to option 3 ($\vec{\kappa}$ and $\vec{\omega}$ as inputs), the third row to option 4 ($\vec{\kappa}$ and $\vec{v}$ as inputs) and the fourth row to option 6 ($\vec{\kappa}$, $\vec{v}$ and $\vec{\omega}$ as inputs). The scattered green dots represent estimated $q_2(s,t)$ versus $\kappa_2(s,t)$, through which a polynomial is fitted and the least-squares error representing the estimated constitutive law and plotted discretely as blue asterisks in the perspective of the red curve, which represents the actual constitutive law given by Eq. 4.18. The degree of the fitted polynomial is automatically converged by a fitting algorithm. It matches the degree of actual constitutive law in all successful results. The actual and fitted polynomial expressions are also shown in each result.

While all of the four options provide good estimates of the constitutive law, the least square differences between the estimated and the actual constitutive laws suggest that the algorithm 4 is consistently the best. The next section analyzes the robustness of these four options.

4.5.5 Robustness of Algorithms

The kinematic variables are obtained from configuration data via numerical differentiations in space and/or time. So, they tend to be noisy. This section analyses the robustness of the aforementioned algorithms with respect to their input kinematic variables. To do so, a numerical approximation of white noise, n is added to the inputs using the random number generator in MATLAB. This noise in the input quantities affect the values of the estimated internal moments and consequently the final estimation of the constitutive law. The root mean square (RMS) of the differences (Dif) between the estimated and exact constitutive laws are plotted as noise increases. The RMS differences are normalized by the maximum value of the moments (infinity norm), and the variance of the noise in the inputs is normalized by the square of maximum value of the corresponding input. Figure 4.16 shows how the estimated constitutive law deviates from the

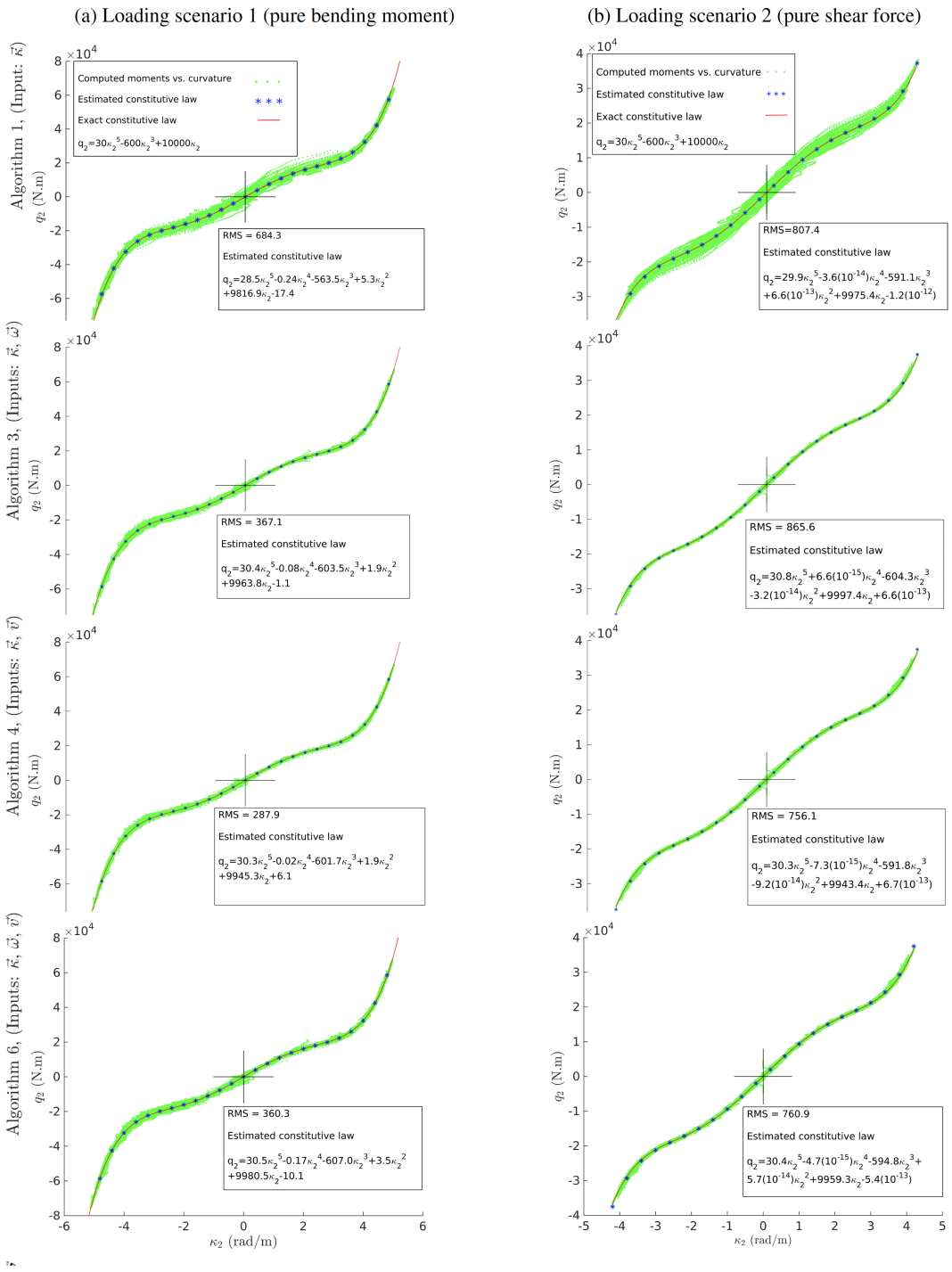

Figure 4.15: Constitutive law estimated by different inverse algorithms.

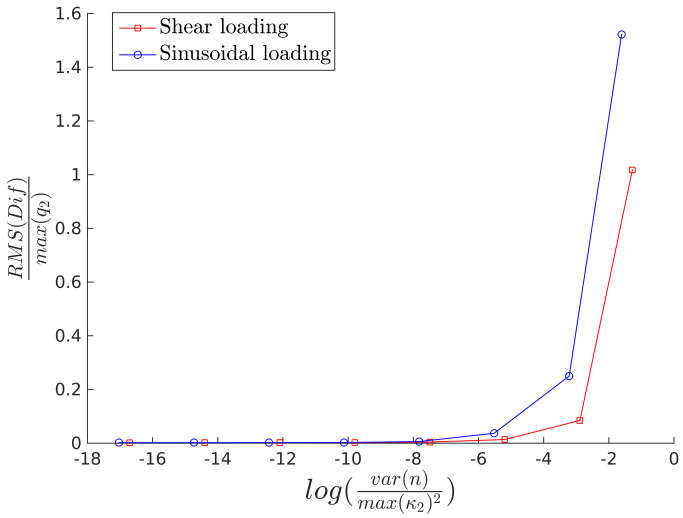

Figure 4.16: The normalized RMS of the differences, Dif between the exact and estimated internal moments versus normalized variance of the input noise for algorithm number one in Table 4.1.

exact constitutive law as the numerical noise in the input curvature increases when the algorithm number one in the Table 4.1 is used to identify the constitutive law. The figure implies that for the normalized variance of the noise in curvature $\frac{var(n)}{max(\kappa^2)}$ less than 10^{-4} the estimation of the constitutive law is not affected significantly and the method gives a reliable estimation. However, when the normalized variance of input noise grows to the order of 10^{-2}, the estimated constitutive law starts to significantly deviate from the exact function.

Next, robustness of the algorithm number three in Table 4.1 is investigated. This algorithm has two input variables $\vec{\kappa}$ and $\vec{\omega}$. Therefore, the white noise is added to both of the input variables. Figure 4.17(a) shows the effects of noise on the estimation of the constitutive law. The color scale represents the RMS of the differences between the exact and estimated constitutive law, normalized by maximum of the internal moment. The result shows that algorithm number three is less sensitive with respect to the noise in the angular velocity in comparison to the noise in the input curvature values.

Furthermore, I analyze the robustness of the algorithm number four in Table 4.1 that uses $\vec{\kappa}$ and $\vec{v}$ as input variables. Figure 4.17(b) shows the effect of numerical noise in the input variables on the estimation of the constitutive law for this algorithm. It can be inferred from Figure 4.17 that the estimation of the constitutive law is more sensitive to the noise in curvature that to the noise in linear velocity.

The robustness of the algorithm number six in Table 4.1 is shown in Figure 4.18 by

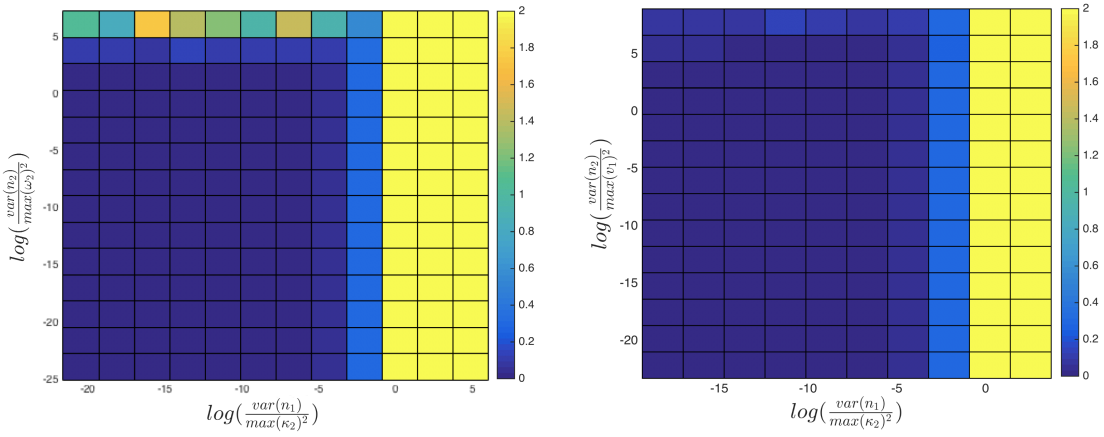

(a) Input $\vec{\kappa}$, $\vec{\omega}$ (b) Input $\vec{\kappa}$, $\vec{v}$

Figure 4.17: The normalized RMS of the differences (Dif) between the exact and estimated constitutive law versus the variance of the input noises for algorithms three (a) and four (b) in Table 4.1 with loading scenario 1. The color scale represent the normalized RMS (Dif), while $var(n_i)$ is the variance of the numerical noise that is normalized by squared value of the maximum of the curvature and angular velocity (a) or velocity (b).

adding noise to the input variables $\vec{v}$, $\vec{\omega}$ and $\vec{\kappa}$. The robustness analysis of this algorithm also reveals that the algorithms are more susceptible to the noise in curvature than to the noise in the angular and linear velocities.

4.6 Discussion and Conclusions

This Chapter presents implementation and analysis of several inverse algorithms that use the dynamic configurational data to estimate the constitutive laws of filaments. The inverse approach is based on a continuum rod model and can use different combination of kinematic variables to estimate the restoring forces and moments in the filament. However, in all the algorithms, it is consistently found that the curvature and twist vector $\vec{\kappa}$ is the most crucial input. The choice of the input variables determines how many steps will be involved in the method. Thus, the number of numerical integrations and differentiations vary in each algorithm and directly affect the estimation of the constitutive law. In this work, the inverse algorithms use the deformation data obtained from a forward rod model simulation of planar bending with nonlinear (5-th order polynomial) constitutive law. The algorithm number four that uses linear velocity along with curvature and twist as measured inputs showed the most accurate estimation of constitutive law. The robustness analysis of each algorithm is also performed. It is found that the method, in general, is more sensitive to the noise in curvature than the noise in velocity and angular velocity.

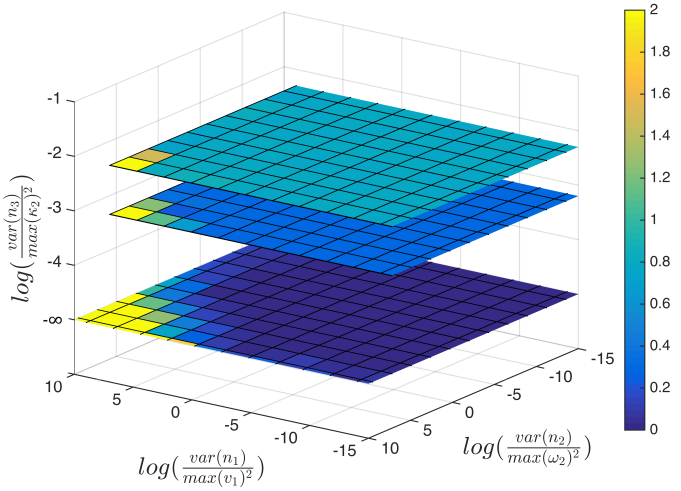

Figure 4.18: The normalized RMS of the differences (Dif) between the exact and estimated moments are color coded and shown against the normalized variances of the noises in inputs for algorithm number six in Table 4.1.

To handle noisy input data there are strategies to smooth them and overcome the corruption of the final estimation. One such strategy is windowing that smooths high frequency harmonics and improves approximation of the numerical derivatives.

Overall, in this chapter, I have shown a viable approach of developing an inverse rod model that requires no a priori knowledge of the form of the nonlinearity in the constitutive law.

Chapter 5

AN ADJOINT-BASED INVERSE APPROACH FOR NON-HOMOGENEOUS CONSTITUTIVE LAWS

5.1 Introduction

In this chapter, I formulated a simple but representative inverse problem governed by the linear elastic equation with non-homogeneous coefficient field. In particular, I discuss the reconstructability of the Lamé parameter field from synthetic observations of the displacement field under cantilever loading. In this section, I follow the approach in [88] and solve the underlying least-squares minimization problem using an adjoint-based inexact Newton-conjugate gradient method, which uses first and second derivative information of the least-squares cost functional. The numerical results show that the reconstructions of the Lamé parameter field converge to the exact parameter as the observation error decreases. We also show that the number of Newton iterations is insensitive to the dimension of the parameters, i.e., the computational cost of solving the inverse problem–measured in number of PDE (Partial Differential Equations) solves–is constant as the size of the problem is increased. Therefore, this computational framework has the potential to solve high-dimensional inverse elasticity problems that are of practical interest.

In addition, I formulated the inverse problem in a Bayesian inference framework [89, 90]. Computing the general solution of this inverse problem (i.e., the posterior probability density) can become prohibitive, due to the expense of solving the forward model and the high dimensionality of the uncertain parameters (which are discretizations of the elasticity parameter field). To cope with the infinite-dimensional (i.e., large-scale) character of the parameter field, it is common to construct a Gaussian approximation to the posterior at the maximum a posteriori probability (MAP) point (see [54], and references therein). The MAP point in the Gaussian case coincides with the mean and it is given by the solution of the deterministic inverse elasticity problem. In this chapter, I followed the approach in [88] and solve the underlying least squares minimization problem using an adjoint-based inexact Newton-conjugate gradient method, which uses first and second derivative information of the least squares cost functional. The posterior covariance matrix can be computed using the inverse of the Hessian of the least squares cost functional of the deterministic inverse elasticity problem. I applied this method to quantify uncertainties in the inference of the Young's modulus parameter field from synthetic

observations of the cantilever deformation as well as a deformations of rod with helical structure.

The Chapter is organized as follows. Section 5.2 introduces the forward problem of a cantilever as the Navier-Lamé model of linear elasticity. The computational forward solver is benchmarked against an analytical solution of a simple loading scenario in Section 5.3. In Section 5.4 we formulate the inverse problem governed by the forward elasticity model and discuss an efficient solution method to solve this problem. In Section 5.5 we present two model problems, one with a smooth non-homogeneous stiffness coefficient, and the other with a discontinuous stiffness coefficient and discuss the performance of the inexact Newton-conjugate gradient method. Section 5.6 offers a discussion on the results of the deterministic inverse approach. In Sections 5.7 and 5.8, formulation of the inverse problem in Bayesian inference framework is discussed. In Section 5.9 two model problems are defined to illustrate the performance of the Bayesian approach. Finally, Section 5.8 provides concluding remarks on the results of Bayesian inversion.

5.2 Forward Problem: Linear Elastic Model

Any inverse numerical model is build upon a rigorous forward model. Therefore, I briefly explain the linear elastic model and will discuss the numerical approach that is used to solve the underlying equations. The equations of linear elasticity are derived in strong form by applying the equilibrium of momentum to a material point. These equations under static equilibrium can be written as follows [91]

$$-\boldsymbol{\nabla}\cdot\boldsymbol{\sigma} = \boldsymbol{f}, \tag{5.1a}$$

where $\boldsymbol{\sigma}$ denotes the stress tensor and the body force is denoted by $\boldsymbol{f}$. Equation (5.1) is the Navier-Lamé model of linear elasticity that describes a boundary value problem for a cantilever. We employ a constitutive law that relates the stress tensor $\boldsymbol{\sigma}$ and the strain tensor $\boldsymbol{\varepsilon_u} = \frac{1}{2}(\boldsymbol{\nabla u} + \boldsymbol{\nabla u}^T)$ by

$$\boldsymbol{\sigma} = 2\mu\boldsymbol{\varepsilon_u} + \lambda tr(\boldsymbol{\varepsilon_u})\boldsymbol{I}, \tag{5.1b}$$

where λ and μ are the Lamé coefficients, and $\boldsymbol{u}$ is the displacement. The relationship between the Lamé coefficients and Young's modulus E and Poisson ratio ν is given in the Section 5.5.

We choose the model domain Ω to be a two-dimensional rectangular section of a cantilever (as shown in Figure 5.1) with the following boundary conditions. On the left boundary, Γ_D, we impose homogeneous Dirichlet condition to model a clamped end, and on Γ_N, we impose a traction-free, i.e., homogeneous Neumann boundary condition

$$\boldsymbol{u} = \boldsymbol{0} \quad \text{on } \Gamma_D \tag{5.1c}$$

$$\boldsymbol{\sigma n} = \boldsymbol{t} \quad \text{on } \Gamma_N. \tag{5.1d}$$

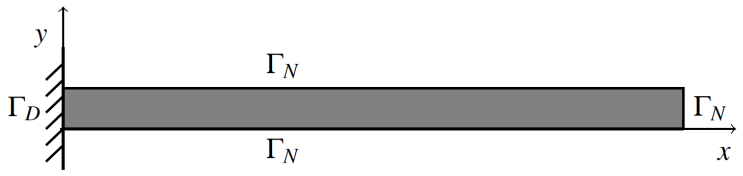

Figure 5.1: The domain Ω (grey shaded region) and coordinate system for the linear elastic problem (5.1) modeling a cantilever. The boundary $\partial\Omega = \Gamma_N \cup \Gamma_D$ (with $\Gamma_N \cap \Gamma_D = \emptyset$), where Γ_N and Γ_D are boundaries with Dirichlet and Neumann boundary conditions, respectively, defined in (5.1c)–(5.1d).

The numerical solution of the boundary value problem (5.1a)–(5.1d) is obtained by the finite element method [92]. Therefore, the weak form of this boundary value problem has to be derived. If we multiply (5.1a) with a test function $\boldsymbol{v}$ belonging to $V_d = \{\boldsymbol{v} \in H^1(\Omega) : \boldsymbol{v} = 0 \text{ in } \Gamma_D\}$ and use the Green's second identity, we obtain the weak form of (5.1a)–(5.1d), that reads: Find $\boldsymbol{u} \in V_d$ such that

$$\int_\Omega \boldsymbol{\sigma} : \boldsymbol{\varepsilon}_{\boldsymbol{v}}\, dx = \int_{\Gamma_N} \boldsymbol{v} \cdot \boldsymbol{t}\, ds + \int_\Omega \boldsymbol{f} \cdot \boldsymbol{v} dx, \quad \forall \boldsymbol{v} \in V_d. \tag{5.2}$$

We note that for the cases in which traction is zero on the boundary, the first term on the right hand side of Eq. (5.2) vanishes. For simplicity, in what follows we assume that this is the case.

5.3 Validation of Forward Solver

In this section the forward model is validated for a simple loading scenario in which deriving the analytical solution of the stress distribution is readily possible.

5.3.1 Analytical Solution

Consider the problem shown in Figure 5.2 (left). The beam is subjected to a uniform shear stress $\sigma_{xy} = \tau$ over its free end. Corresponding boundary conditions are

$$\sigma_{xx}(0,y) = 0, \quad \sigma_{xy}(0,y) = \tau, \quad \sigma_{yy}(0,\pm b) = \sigma_{xy}(0,\pm b) = 0. \tag{5.3}$$

The analytical solution for this problem can be obtained by relaxing one of the above conditions and using Airy stress function. The formulation of Airy stress function ϕ for the planar stress is given below.

$$\nabla^4 \phi = 0 \tag{5.4}$$

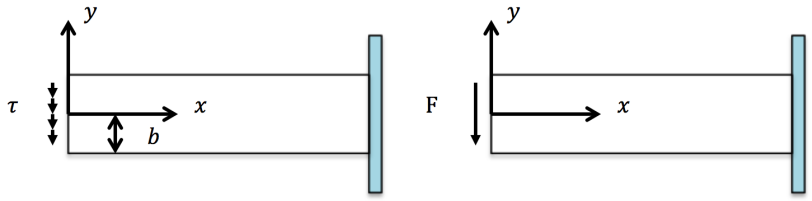

Figure 5.2: A cantilever subjected to a uniform distribution of shear stress on the free end (left) that is modeled by finite element approach. For analytical solution it is assumed a shear force is applied to the free end (right).

$$\sigma_{xx} = \frac{\partial^2 \phi}{\partial y^2} \tag{5.5}$$

$$\sigma_{yy} = \frac{\partial^2 \phi}{\partial x^2} \tag{5.6}$$

$$\sigma_{xy} = -\frac{\partial^2 \phi}{\partial x \partial y} \tag{5.7}$$

Now consider the similar problem in Figure 5.2 (right). This beam is subjected to a shear force F which is defined to be the resultant force of the shear stress τ.

$$\int_{-b}^{+b} \sigma_{xy}(0,y)dy = 2b\tau = F \tag{5.8}$$

This is called the weak boundary condition, since the stress is not specified directly on the boundary and only its resultant is. However, the Saint-Venant's principle states that the stresses in these two problems are equal other than a region very close to the boundary $x = 0$ and $y \in [-b,b]$. Therefore, by constructing the Airy stress function as represented in Eq. (5.9) the stresses can be obtained using the Eqs. (5.5) to (5.7).

$$\phi = \alpha x y^3 - 3\alpha b^2 x y \tag{5.9}$$

Therefore, the elements of the stress tensor are obtained as follows.

$$\sigma_{xx} = \frac{3F}{2b^3}xy, \qquad \sigma_{xy} = \frac{3F}{4b^3}(b^2 - y^2), \qquad \sigma_{yy} = 0 \tag{5.10}$$

The Figure 5.3 is showing the contours of the stress σ_{xx} for the beam with $b = 1$ and length $L = 4$ where $\tau = -10$.

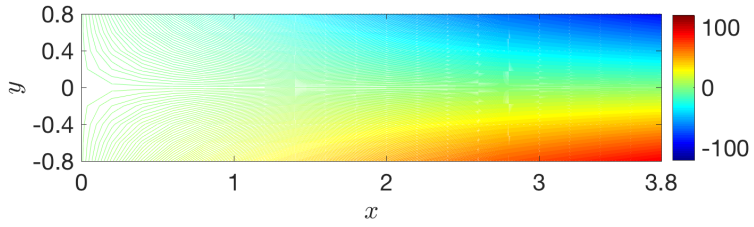

Figure 5.3: Contours of the normal stress $\sigma_{xx} = \frac{3F}{2b^3}xy$ obtained by Airy stress function.

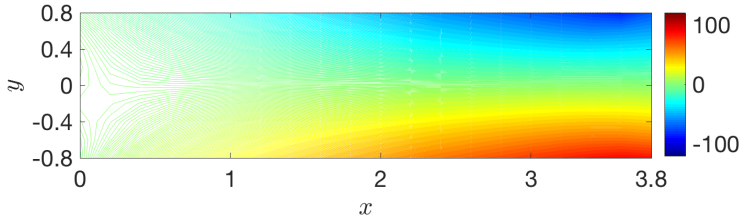

Figure 5.4: Contours of the normal stress σ_{xx} obtained by finine element solution.

5.3.2 Finite Element Solution

The problem that is shown in Figure 5.2 (left) can be solved to find the stress tensor using the equations of linear elasticity (5.1). The domain of this problem is $\Omega = [0,4] \times [-1,1]$ with the following boundary condition.

$$\boldsymbol{u} = (0,0) \quad \text{on } x = 4, \tag{5.11}$$

$$\boldsymbol{\sigma n} = (0,-10) \quad \text{on } x = 0. \tag{5.12}$$

Equation (5.11) expresses the Dirichlet's boundary condition which is imposed on the clamped end of the cantilever. Equation (5.12) is the Neumann's boundary condition and prescribes the traction on the free end. The body force $\boldsymbol{f}$ in this scenario is zero. The Figure 5.4 is showing the contours of the stress σ_{xx} found by the forward solver for the beam with $E = 4000$ and $\nu = 0.3$.

Figures 5.3 and 5.4 are showing that the values of the normal stress σ_{xx} obtained by finite element solution are very close to those obtained by analytical approach.

5.4 Inverse Problem: Inferring the Lamé Parameter from observed Displacement

In this section, I describe the solution of the inverse problem of inferring the two-dimensional Lamé parameter field, λ in (5.25) from synthetic observations of the displacement field under cantilever loading with the elastic model described in the previous section.

5.4.1 The Regularized Inverse Problem

Using noisy (synthetic) measurements $\boldsymbol{u}^{obs}$ (of $\boldsymbol{u}$) in Ω, I seek to estimate the unknown parameter field $\lambda = \lambda(\boldsymbol{x})$, assuming that $\boldsymbol{f}$ and μ are known. That is, I am interested in finding parameter field, λ such that the *misfit*, $\boldsymbol{u} - \boldsymbol{u}^{obs}$ is minimized on Ω. This is expressed as the following constrained minimization problem

$$\min_{\lambda} \mathscr{J}(\lambda) := \frac{1}{2}\int_{\Omega}(\boldsymbol{u} - \boldsymbol{u}^{obs})^2 dx + \mathscr{R}(\lambda, \gamma), \tag{5.13}$$

where $\boldsymbol{u} = \boldsymbol{u}(\lambda)$ is found by solving (5.1) for given λ. The rightmost term in (5.13) is a regularization term, which is needed to cope with the ill-posedness of the inverse problem [49, 50]. Ill-posedness is a typical feature of many inverse problems, in which the data do not uniquely determine the inversion parameter field. In this work, we choose a Tikhonov regularization, namely

$$\mathscr{R}(\lambda, \gamma) = \frac{\gamma}{2}\int_{\Omega}(\boldsymbol{\nabla}\lambda \cdot \boldsymbol{\nabla}\lambda) dx, \tag{5.14}$$

where γ is a regularization parameter.

5.4.2 Inverse Problem Solver: Adjoint-Based Inexact Newton-CG

We now present an efficient method to solve the nonlinear least-squares optimization problem (5.13). Gradient-based methods such as steepest descent or nonlinear conjugate gradients [93,94] can be used to iteratively find the solution of this optimization problem. However, due to the ill-posedness that is a common feature of infinite-dimensional inverse problems, a gradient-based method can converge very slowly. Therefore, to solve (5.13) efficiently, here we focus on Newton method, which is known to converge at a superlinear rate [93, 94].

Starting with an initial guess for the parameter λ, Newton's method iteratively updates this field by $\lambda^{k+1} = \lambda^k + \alpha\hat{\lambda}$, where λ^k is the current parameter and the Newton direction $\hat{\lambda}$ is obtained by solving the linear system

$$\mathscr{H}(\lambda^k)\hat{\lambda} = -\mathscr{G}(\lambda^k). \tag{5.15}$$

Here, $\mathscr{G}$ is the gradient of the regularized data misfit functional $\mathscr{J}$ in (5.13), and $\mathscr{H}$ is its Hessian operator. To guarantee convergence, the new value of the parameter is found by damping the Newton direction, i.e., by choosing a step length α via an Armijo line search for example, such that the cost functional in (5.13) is sufficiently decreased at each iteration [93, 94].

To facilitate the computation of the infinite-dimensional gradient and Hessian, we use the Lagrangian approach [95–97], in which the Lagrange multiplier function $\boldsymbol{p} \in V_d$

plays the role of the test function in enforcing the weak form of the elastic problem (5.2). The Lagrangian functional is given by

$$\mathscr{L}(\boldsymbol{u},\lambda,\boldsymbol{p}) = \mathscr{J}(\lambda) + \int_\Omega \boldsymbol{\sigma_u} : \boldsymbol{\varepsilon_p} dx - \int_\Omega \boldsymbol{f}\cdot\boldsymbol{p} dx,\ \forall \boldsymbol{p} \in V_d. \tag{5.16}$$

The gradient of $\mathscr{J}$ can be found as the variation of the Lagrangian, $\mathscr{L}$ with respect to λ, provided variations of $\mathscr{L}$ with respect to $\boldsymbol{u}$ and $\boldsymbol{p}$ vanish. Thus, the gradient $\mathscr{G}(\lambda)$ at λ

$$\mathscr{G}(\lambda)(\tilde{\lambda}) = \gamma \int_\Omega \boldsymbol{\nabla}\tilde{\lambda}\cdot\boldsymbol{\nabla}\lambda dx + \int_\Omega (\tilde{\lambda} tr(\boldsymbol{\varepsilon_u})\boldsymbol{I}) : \boldsymbol{\varepsilon_p} dx. \tag{5.17}$$

In the gradient expression above, $\boldsymbol{u}$ and $\boldsymbol{p}$ satisfy the *forward* and *adjoint* problems, respectively, which are obtained by invoking stationarity of $\mathscr{L}$ with respect to the Lagrange multiplier (also known as the adjoint) and forward variables $\boldsymbol{p}$ and $\boldsymbol{u}$. We note that enforcing stationarity of $\mathscr{L}$ with respect to the adjoint variable $\boldsymbol{p}$ simply recovers the weak form of the forward equation given by (5.2). The weak form of the adjoint problem is obtained by taking variations of the Lagrangian functional with respect to $\boldsymbol{u}$ in a direction $\tilde{\boldsymbol{u}}$, namely

$$\mathscr{L}_u(\boldsymbol{u},\lambda,\boldsymbol{p})(\tilde{\boldsymbol{u}}) = \int_\Omega (\boldsymbol{u}-\boldsymbol{u}^{obs})\tilde{\boldsymbol{u}} dx + \int_\Omega \boldsymbol{\sigma}_{\tilde{\boldsymbol{u}}} : \boldsymbol{\varepsilon_p} dx,\ \forall \tilde{\boldsymbol{u}} \in V_d, \tag{5.18}$$

and letting this vanish for all directions $\tilde{\boldsymbol{u}}$. The strong form of the adjoint problem is obtained by integration by parts in (5.18)

$$-\boldsymbol{\nabla}\cdot\boldsymbol{\sigma_p} = -(\boldsymbol{u}-\boldsymbol{u}^{obs}) \tag{5.19a}$$

$$\boldsymbol{p} = \boldsymbol{0} \quad \text{on } \Gamma_D \tag{5.19b}$$

$$\boldsymbol{\sigma_p}\boldsymbol{n} = \boldsymbol{0} \quad \text{on } \Gamma_N. \tag{5.19c}$$

We note that the adjoint equation is driven by the misfit between the solution $\boldsymbol{u}$ of the forward problem and the observational data $\boldsymbol{u}^{obs}$.

The action of the Newton Hessian operator in a direction $\hat{\lambda}$ is obtained by taking second variations of $\mathscr{L}$ with respect to all variables [88, 98]. This can be expressed (in weak form) as

$$\mathscr{H}(\lambda,\tilde{\lambda})\hat{\lambda} = \gamma \int_\Omega \boldsymbol{\nabla}\tilde{\lambda}\cdot\boldsymbol{\nabla}\hat{\lambda} dx + \int_\Omega (\tilde{\lambda} tr(\boldsymbol{\varepsilon_u})\boldsymbol{I}) : \boldsymbol{\varepsilon}_{\hat{\boldsymbol{p}}} dx, \tag{5.20}$$

where the incremental adjoint displacement $\hat{\boldsymbol{p}}$ satisfies the *incremental adjoint problem*

$$-\boldsymbol{\nabla}\cdot\boldsymbol{\sigma}_{\hat{\boldsymbol{p}}} = -\hat{\boldsymbol{u}} \tag{5.21a}$$

$$\hat{\boldsymbol{p}} = \boldsymbol{0} \quad \text{on } \Gamma_D \tag{5.21b}$$

$$\boldsymbol{\sigma}_{\hat{\boldsymbol{p}}}\boldsymbol{n} = \boldsymbol{0} \quad \text{on } \Gamma_N, \tag{5.21c}$$

and the incremental forward displacement $\hat{\boldsymbol{u}}$ satisfies the *incremental forward problem*

$$-\boldsymbol{\nabla}\cdot\boldsymbol{\sigma}_{\hat{\boldsymbol{u}}} = \boldsymbol{\nabla}\cdot(\hat{\lambda} tr(\boldsymbol{\varepsilon}_{\boldsymbol{u}})\boldsymbol{I}) \tag{5.22a}$$

$$\hat{\boldsymbol{u}} = \boldsymbol{0} \quad \text{on } \Gamma_D \tag{5.22b}$$

$$\boldsymbol{\sigma}_{\hat{\boldsymbol{u}}}\boldsymbol{n} = \boldsymbol{0} \quad \text{on } \Gamma_N. \tag{5.22c}$$

Thus computation of gradients and Hessian actions are expressed as solutions of forward and adjoint PDEs. Once the gradient and the action of the Hessian operator are defined, we can solve the optimization problem (5.13) with an inexact matrix-free Newton–conjugate gradient (CG) method. To reduce the number of CG iterations, we precondition the Hessian operator by the inverse of the regularization operator. In the numerical results section, we will demonstrate that the number of outer Newton iterations and of inner CG iterations is independent of the mesh size, as is expected for a wide class of inverse problems.

5.5 Inversion results

This section presents two representative problems with cantilever loading (shown in Figure 5.1) to study the performance of inverse method described in Section 5.4 for reconstruction of the parameter field λ. The first problem focuses on the inversion of a smooth (sinusoidal) Lamé parameter field for different signal-to-noise ratios (SNRs). The second problem targets a discontinuous parameter field. In each of the two representative problems, the two-dimensional domain of the cantilever is $\Omega = [0,8]\times[0,0.5]$. The observation data $\boldsymbol{u}^{obs}$ is synthesized by solving the forward problem described in Section 5.2 and adding a numerical noise to the solution. The forward problem, which requires solving Eq. (5.1) as a boundary value problem, is solved using FEniCS [99, 100], a finite element package. In both the problems, the traction $\boldsymbol{t}$ on the boundary Γ_N is zero, and the cantilever bends under a prescribed body force $\boldsymbol{f}$. Since the parameter λ penalizes the volumetric strain in the constitutive law (5.25), the body force is so chosen that the beam experiences some compression in addition to experiencing shear due to bending.

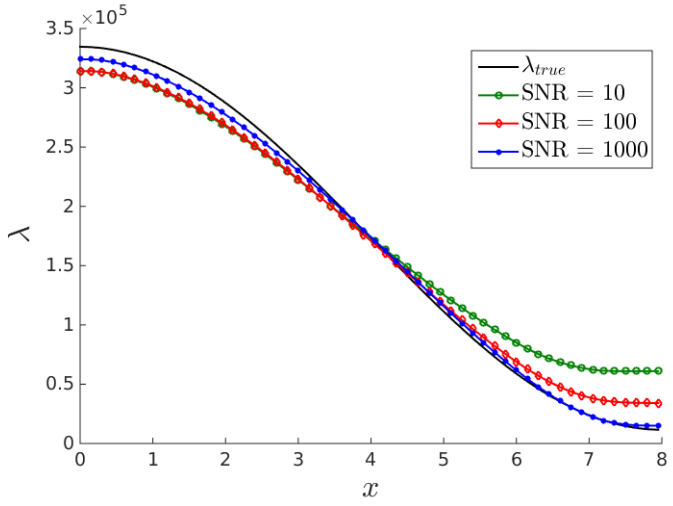

Figure 5.5: The values of the the reconstructed λ field for different signal to noise ratios (SNRs) compared to the true parameter field λ_{true}. The reconstructed λ is taken along a line that passes trough the middle of the beam at $y = 0.25$.

5.5.1 A smooth (sinusoidal) Lamé parameter field

This problems targets a sinusoidal variation in the Young's modulus E and a uniform Poisson ratio ν given by

$$E = 3 \times 10^5 - 2.8 \times 10^5 \sin\left[\pi\left(\frac{x}{8} - \frac{1}{2}\right)\right] \tag{5.23a}$$

$$\nu = 0.3. \tag{5.23b}$$

Lamé parameters, μ and λ, are calculated from E and ν according to

$$\lambda = \frac{E\nu}{(1+\nu)(1-2\nu)} \tag{5.24a}$$

$$\mu = \frac{E}{2(1+\nu)}. \tag{5.24b}$$

The synthetic observation data $\boldsymbol{u}^{obs}$ for the inversion of λ is generated by bending the cantilever under a uniform body force $\boldsymbol{f} = (-1000, 100)$. The inversion is tried for three different signal-to-noise ratios (SNRs), namely 10, 100 and 1000. Figure 5.5 shows the reconstructed λ field for each SNR along with the true λ field. It is noted that the method converges as the magnitude of the numerical noise diminishes.

Figure 5.6 shows the reconstructed Lamé parameter field ($\lambda_{inversion}$) for SNR $=$ 100, the true parameter field (λ_{true}), and the (uniform) initial guess of $\lambda_{initial} = 1.0 \times 10^3$ that was used for Newton iterations. Figure 5.7 shows the displacement fields on a color

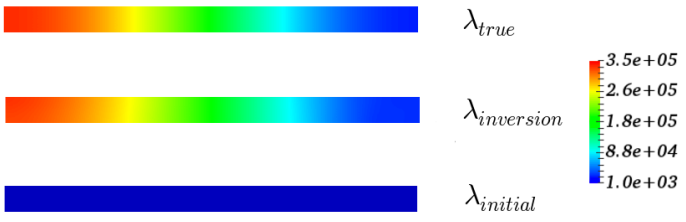

Figure 5.6: The true parameter λ_{true} with sinusoidal variation (top), reconstructed parameter field (middle) and the initial guess for Newton iterations (bottom).

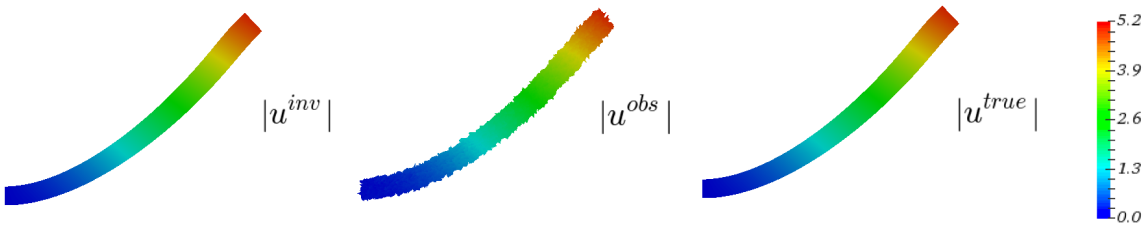

Figure 5.7: The displacement field of the beam with sinusoidal variation of the parameter λ. The solution of the forward model is shown by $\boldsymbol{u}^{true}$ (right). The synthetic observation $\boldsymbol{u}^{obs}$ (middle) is found by adding 1% noise to the $\boldsymbol{u}^{true}$. The recovered displacement field obtained by using the Newton method is $\boldsymbol{u}^{inv}$ (left).

scale with the accordingly deformed shapes of cantilever. The synthetic observations, $\boldsymbol{u}^{obs}$, are obtained by running the forward model with λ_{true} to obtain $\boldsymbol{u}^{true}$ and adding 1% noise (SNR $= 100$). The recovered displacement field is denoted by$\boldsymbol{u}^{inv}$. This figure demonstrates that the inversion matches well the observations. The optimum value of the regularization parameter, γ, for this numerical experiment is found by Morozov's criteria [50] as illustrated in Figure 5.8. The optimal γ using Morozov's criteria ensures that the norm of the misfit $|\boldsymbol{u} - \boldsymbol{u}^{obs}|$ is comparable to the norm of the noise in the data.

Finally, it is useful to recognize that the number of PDE solves for the Newton method is insensitive to the number of inversion parameters, an important requirement especially when the target application is of large scale. To this end, Table 5.1 shows that by refining the mesh, the computational cost, measured by number of PDE solves, remains approximately constant, which is not the case with gradient-based adjoint methods [101].

5.5.2 A discontinuous Lamé Parameter Field

This problem again has the same uniform Poisson ratio $\nu = 0.3$, but a discontinuous variation in the Young's modulus E. For $x \in [0,4]$ (left half cantilever), $E = 3 \times 10^5$, and for $x \in (4,8]$ (right half cantilever), $E = 2 \times 10^4$. Such discontinuities in nano-scale

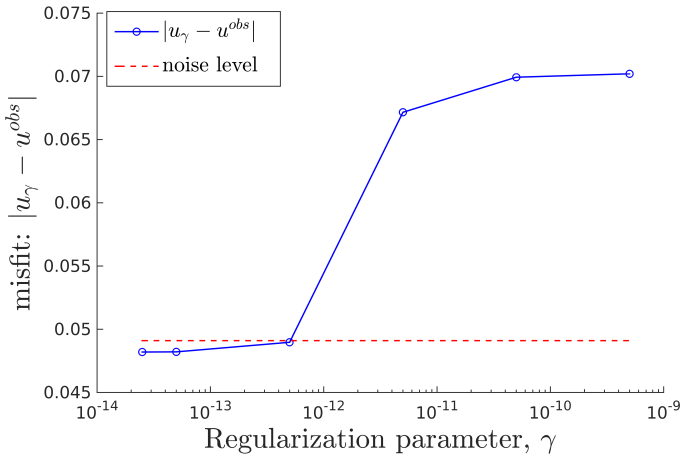

Figure 5.8: The Morozov's criteria is used to find the optimal value of regularization parameter γ.

filaments can occur due to changes in their chemical structure [26]. They are also found in the Magnetic Resonance Elastography (MRE) images of the interface between normal tissue and cancerous tissue [102].

Note that the overall stiffness of the beam in this problem is smaller than that in the previous problem. Therefore the synthetic observation is generated using a commensurately smaller uniform body force $\boldsymbol{f} = (-100, 30)$. As in the previous problem, a noise of 1% is added (i.e., SNR $= 100$).

The reconstructed parameter field for this problem is shown in Figure 5.9. It is evident from this figure that while the proposed inversion method captures the location of the discontinuity of the proposed λ parameter field, the reconstruction is smooth. This is due to the use of a Tikhonov regularization, which penalizes the magnitude of the gradient of λ. The abrupt changes and sharp edges are captured commonly using the total variation (TV) regularization [103] or regularization performed by the BV-seminorm [104].

Figure 5.10 shows the true (left), observed (center) and recovered (right) displacement fields. We note that despite the poor reconstruction of the parameter field on the left of the discontinuity, the recovered displacement field matches extremely well the true displacement field.

5.6 Discussion on the Deterministic Approach

This section presents a Hessian-based inversion approach to estimate the Lamé parameter field for cantilever beams from their displacement fields. We show that the number of PDE solves for the Newton method is insensitive to the number of inversion parameters, an important requirement especially when the target application is of large scale. This would not be the case with gradient (only)-based methods, as our previous

Table 5.1: Number of iterations (#iter) and the number of PDE solves (#PDE) for the inexact Newton method for an inverse elasticity problem. The first column (Mesh) shows the number of elements used to discretize the variables and the second column (#par) indicates the number of inversion parameters (λ). The third column reports the number of Newton iterations, and in parentheses the overall number of CG iterations. The last column reports the number of PDE solves needed by the method to converge. The iterations are terminated when the norm of the gradient is decreased by a factor of 10^6. This table shows that the cost of solving the inverse problem by the Newton method (measured in number of PDE solves) is roughly independent of the number of inversion parameters.

Mesh	#par	#iter	#PDE
80×20	1701	11 (42)	106
160×40	6601	11 (44)	110
240×60	14701	12 (47)	118
320×80	26001	12 (48)	120

experience shows [88]. While the method has been presented for inversion of a single Lamé parameter field, the extension to inversion of both the Lamé parameters is trivial.

We have formulated and solved two model problems to study the invertibility of the Lamé parameter field. First, we focused on the inversion of a smooth (sinusoidal) Lamé parameter field for different SNRs. We found that the reconstructions converge to the true Lamé parameter field as the noise in the synthetic observations decreases. The second model problem targeted a discontinuous parameter field. The results for this problem show that while we are able to reconstruct the location of the discontinuity, the Tikhonov regularization applied smoothed out the sharp edges. In future work we intend to extend this inversion framework to include total variation regularization, known to preserve sharp interfaces [50]. In addition, after a (deterministic) inverse solution is found, the question is how much confidence we can have in the inverse solution. To answer this question, we will turn to the framework of Bayesian inference, which provides a systematic means of quantifying uncertainty in the solution of the inverse problem.

5.7 Bayesian Inversion

In the previous section the regularized inverse formulation was effective to reconstruct the parameter field λ. In these scenarios the observable quantity u^{obs} was available at every computational node. However, in physical experiments it is not often possible to measure the observable quantity everywhere in the domain. For instance, a technique such as ultrasound elastography has low resolution in the directions perpendicular to the axis of the transducer and only one component of the displacement field is measurable this way [105]. In the cases where limited information is accessible, the Bayesian method can infer an statistical estimate about the expected values of the parameter field. The

Figure 5.9: The true parameter λ_{true} with a discontinuity (top), reconstructed parameter field (middle) and the initial guess for Newton iterations (bottom). The true parameter λ_{true} is calculated by substituting $E = 3 \times 10^5$, $\nu = 0.3$ for $x \in [0,4]$ and $E = 2 \times 10^4$, $\nu = 0.3$ for $x \in (4,8]$ in Eq. 5.24.

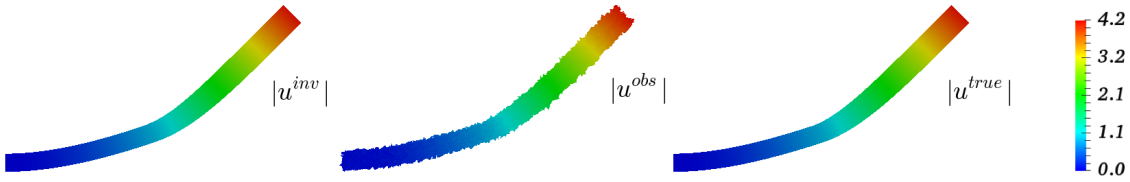

Figure 5.10: The displacement field of the beam with discontinuous jump in the parameter λ. The solution of the forward model is shown by $\boldsymbol{u}^{true}$ (right). The synthetic observation $\boldsymbol{u}^{obs}$ (middle) is found by adding 1% noise to the $\boldsymbol{u}^{true}$. The recovered displacement field obtained by using the Newton method is $\boldsymbol{u}^{inv}$ (left).

solution of the Bayesian inverse problem that is the posterior probability distribution, determines how the information from the observable quantity can be used to identify the unknown parameters. In other words, the estimation results approach the real values of the parameters, as much as the data is informative.

The mechanical properties of a linearly elastic material, which can be described by Young's modulus E and Poisson's ratio ν parameters, can not be directly observed or measured in an experiment hence these are typically unknown or uncertain. However in experimental techniques– such as elastography [105]– it is common to measure the components of the displacement field across the domain, which can be used to infer these parameters. Inferring the mechanical properties of a material using the measurements– such as the displacement field $\boldsymbol{u}^{obs}$ – can be formulated as an inverse problem. In this section we formulate an inverse problem for the elasticity parameter field E, and describe an efficient numerical technique to solve this problem.

In the following, we employ a constitutive law that relates the stress tensor $\boldsymbol{\sigma}_{\boldsymbol{u}}$ and

the strain tensor $\boldsymbol{\varepsilon}_{\boldsymbol{u}} = \frac{1}{2}(\boldsymbol{\nabla u} + \boldsymbol{\nabla u}^T)$ by

$$\boldsymbol{\sigma}_{\boldsymbol{u}} = \frac{E}{1+\nu}\boldsymbol{\varepsilon}_{\boldsymbol{u}} + \frac{E\nu}{(1+\nu)(1-2\nu)} tr(\boldsymbol{\varepsilon}_{\boldsymbol{u}})\boldsymbol{I}, \tag{5.25}$$

where $\boldsymbol{u}$ is the displacement, E is the Young's modulus, ν is the Poisson's ratio, and $\boldsymbol{I}$ is the second-order unit tensor.

5.8 Inverse Problem: Bayesian Quantification of the Parameter Uncertainty

To answer the question of what confidence we have in the inverse solution we turn to the framework of Bayesian inference [89, 90]. In this framework, the inverse problem is formulated as a problem of statistical inference over the space of uncertain parameters. The solution is the posterior probability distribution function that expresses how likely it is that a set of candidate parameters gives rise to the observed data via the physical model. The Bayes' theorem combines the prior probability distribution, $\pi_{\text{prior}}(E)$, with a likelihood, $\pi_{\text{like}}(\boldsymbol{u}^{obs}|E)$, to calculate the posterior probability distribution $\pi_{\text{post}}(E|\boldsymbol{u}^{obs})$, namely

$$\pi_{\text{post}}(E|\boldsymbol{u}^{obs}) \propto \pi_{\text{prior}}(E)\pi_{\text{like}}(\boldsymbol{u}^{obs}|E). \tag{5.26}$$

The prior captures any knowledge, information or assumption about the parameter field E, and the likelihood encodes the probability of observing data $\boldsymbol{u}^{obs}$, given a parameter field E. The posterior, which is the solution of the inverse problem, represents the probability of parameter field E given the observed data $\boldsymbol{u}^{obs}$. In this work we use an additive Gaussian noise model that gives

$$\boldsymbol{u}^{obs} = \boldsymbol{F}(E) + \boldsymbol{\eta}, \quad \boldsymbol{\eta} \sim \mathcal{N}(\boldsymbol{0}, \Gamma_{\text{noise}}), \tag{5.27}$$

where $\Gamma_{\text{noise}} \in \mathbb{R}^{q\times q}$ is the measurement noise covariance matrix, q represents the number of observation points, and $\boldsymbol{F}(\cdot)$ is the so-called parameter-to-observable operator that maps model parameters E to observations $\boldsymbol{u}^{obs}$. Here, evaluation of this map requires solution of the Navier-Lamé Eqs. (5.1) possibly combined with an observation operator B, that allows for extracting q observation points. Furthermore, since the noise $\boldsymbol{\eta}$ is independent of E, thus $\boldsymbol{u}^{obs}|E \sim \mathcal{N}(\boldsymbol{F}(E), \Gamma_{\text{noise}})$, the likelihood is given by

$$\pi_{\text{like}}(\boldsymbol{u}^{obs}|E) \propto \exp\Big(-\frac{1}{2}\Big\langle B\boldsymbol{u} - \boldsymbol{u}^{obs}, \Gamma_{\text{noise}}^{-1}(B\boldsymbol{u} - \boldsymbol{u}^{obs})\Big\rangle\Big), \tag{5.28}$$

where $\langle g, h\rangle$ represents the inner product of the two given functions g and h, i.e.,

$$\langle g, h\rangle = \int_{\Omega} ghdx. \tag{5.29}$$

We use a Gaussian prior defined by the mean E_{pr} and the covariance $\Gamma_{\text{pr}} \in \mathbb{R}^{n\times n}$. We define the covariance as the inverse of the square of a Laplacian-like operator, namely $\Gamma_{\text{pr}} = (-\gamma\boldsymbol{\Delta}E + \delta E)^{-2}$ as in [54]. The parameter γ determines the correlation length of the operator (i.e. the smoothness,) and δ determines the magnitude of its variance. The prior can therefore be written as

$$\pi_{\text{prior}}(E) \propto \exp\Big(-\frac{1}{2}\left\langle E - E_{\text{pr}}, \Gamma_{\text{pr}}^{-1}(E - E_{\text{pr}})\right\rangle\Big). \tag{5.30}$$

According to Bayes' theorem with Gaussian noise and prior, the posteriori density function of E is described as [89, 90]

$$\pi_{\text{post}}(E) \propto \exp\left(-\frac{1}{2}\left\langle B\boldsymbol{u} - \boldsymbol{u}^{obs}, \Gamma_{\text{noise}}^{-1}(B\boldsymbol{u} - \boldsymbol{u}^{obs})\right\rangle - \frac{1}{2}\left\langle E - E_{\text{pr}}, \Gamma_{\text{pr}}^{-1}(E - E_{\text{pr}})\right\rangle\right). \tag{5.31}$$

We note that if the parameter-to-observable map is linear the posterior probability density is Gaussian. However, the further this map is from being linear (which is the case here), the further the posterior is from being Gaussian [89, 90]. In such case, a sampling approach is applied to explore the posterior. To cope with the infinite-dimensional character of the parameter field (hence its high-dimensional nature stemming from discretization), here we construct a Gaussian approximation of the posterior at the maximum a posteriori probability (MAP) point (see [54], and references therein). This MAP point is the parameter vector maximizing the posterior (5.31). It can be found by minimizing the negative log of (5.31), which amounts to solving the optimization problem

$$E_{\text{MAP}} = \arg\min_{E} \mathscr{J}(E) := -\log \pi_{\text{post}}(E). \tag{5.32}$$

There is a number of optimization methods that one can use to solve (5.32), e.g., gradient-based methods such as steepest descent or nonlinear conjugate gradient, or second derivative based (i.e., Hessian) methods [93,94]. For an efficient computation of the MAP point, here we use adjoints- and Hessian-based methods, as we will show in the next section. One of the advantages in doing so is that the posterior covariance matrix Γ_{post} of the Gaussian approximation can then be obtained by computing the action of the inverse of the Hessian (of $\mathscr{J}$ at E_{MAP}) on vectors [89, 90].

5.8.1 Calculating the MAP points: adjoint-based inexact Newton-CG

To solve (5.32) efficiently, here we focus on the Newton method, which is known to converge at a superlinear rate [93, 94]. Starting with an initial guess for the parameter E, Newton's method iteratively updates this field by $E^{k+1} = E^k + \alpha\hat{E}^k$, where E^k is the current parameter and the Newton direction $\hat{E}^k$ is obtained by solving the linear system

$$\mathscr{H}(E^k)\hat{E}^k = -\mathscr{G}(E^k). \tag{5.33}$$

Here, $\mathscr{G}$ is the gradient of the regularized data misfit functional $\mathscr{J}$ in (5.32), and $\mathscr{H}$ is its Hessian operator. To guarantee convergence, the new value of the parameter is found by damping the Newton direction, i.e., by choosing a step length α via an Armijo line search for example, such that the cost functional in (5.32) is sufficiently decreased at each iteration [93, 94].

To facilitate the computation of the infinite-dimensional gradient and Hessian, we use the Lagrangian approach [95–97], in which the Lagrange multiplier function $\boldsymbol{p} \in V_d$ plays the role of the test function in enforcing the weak form of the elastic problem (5.2). The Lagrangian functional is given by

$$\mathscr{L}(\boldsymbol{u}, E, \boldsymbol{p}) = \mathscr{J}(E) + \left\langle \boldsymbol{\sigma}_{\boldsymbol{u}}, \boldsymbol{\varepsilon}_{\boldsymbol{p}} \right\rangle - \langle \boldsymbol{f}, \boldsymbol{p} \rangle . \tag{5.34}$$

The gradient of $\mathscr{J}$ can be found as the variation of the Lagrangian $\mathscr{L}$ with respect to E, provided variations of $\mathscr{L}$ with respect to $\boldsymbol{u}$ and $\boldsymbol{p}$ vanish. Thus, the gradient $\mathscr{G}(E)$ at E is found by taking the Freshet derivative of the Lagrangian functional in the directions $\tilde{\boldsymbol{p}}$, $\tilde{\boldsymbol{u}}$, and $\tilde{E}$ and is shown with $\mathscr{L}_{\boldsymbol{p}}$, $\mathscr{L}_{\boldsymbol{u}}$, and $\mathscr{L}_E$, respectively

$$\left\langle \boldsymbol{\sigma}_{\boldsymbol{u}}, \boldsymbol{\varepsilon}_{\tilde{\boldsymbol{p}}} \right\rangle - \langle \boldsymbol{f}, \tilde{\boldsymbol{p}} \rangle = \mathscr{L}_{\boldsymbol{p}} \tilde{\boldsymbol{p}}, \tag{5.35a}$$

$$\left\langle \boldsymbol{\sigma}_{\tilde{\boldsymbol{u}}}, \boldsymbol{\varepsilon}_{\boldsymbol{p}} \right\rangle + \left\langle B^* \Gamma_{\text{noise}}^{-1} (B\boldsymbol{u} - \boldsymbol{u}^{obs}), \tilde{\boldsymbol{u}} \right\rangle = \mathscr{L}_{\boldsymbol{u}} \tilde{\boldsymbol{u}}, \tag{5.35b}$$

$$\left\langle \Gamma_{\text{pr}}^{-1} (E - E_{\text{pr}}), \tilde{E} \right\rangle + \left\langle \frac{\tilde{E}}{1+\nu} \boldsymbol{\varepsilon}_{\boldsymbol{u}}, \boldsymbol{\varepsilon}_{\boldsymbol{p}} \right\rangle + \left\langle \frac{\tilde{E}\nu}{(1+\nu)(1-2\nu)} tr(\boldsymbol{\varepsilon}_{\boldsymbol{u}}) \boldsymbol{I}, \boldsymbol{\varepsilon}_{\boldsymbol{p}} \right\rangle = \mathscr{L}_E \tilde{E}. \tag{5.35c}$$

We note that the left hand side of (5.35a) is the weak form of the underlying forward problem, and the left hand side of (5.35b) represents the weak form of the corresponding adjoint equation, which is obtained by invoking stationary of $\mathscr{L}$ with respect to forward variable $\boldsymbol{u}$ (or $\mathscr{L}_{\boldsymbol{u}} = 0$). The strong form (obtained by integration by parts) for this equation reads

$$-\boldsymbol{\nabla} \cdot \boldsymbol{\sigma}_{\boldsymbol{p}} = -B^*(B\boldsymbol{u} - \boldsymbol{u}^{obs}) \quad \text{in } \Omega, \tag{5.36a}$$

$$\boldsymbol{p} = \boldsymbol{0} \quad \text{on } \Gamma_D, \tag{5.36b}$$

$$\boldsymbol{\sigma}_{\boldsymbol{p}} \boldsymbol{n} = \boldsymbol{0} \quad \text{on } \Gamma_N. \tag{5.36c}$$

We note that the adjoint equation is driven by the misfit between the solution $\boldsymbol{u}$ of the forward problem and the observational data $\boldsymbol{u}^{obs}$.

Once we have $\boldsymbol{u}$ and $\boldsymbol{p}$, we can evaluate the gradient, which is given in the left hand side of (5.35c). To enforce the stationary of the gradient (or $\mathscr{L}_E = 0$) I use the Newtons method, as explained above, where to compute the direction $\hat{E}^k$ I solve Eq. (5.33). The action of the Hessian operator $\mathscr{H}(E^k)$ in a direction $\hat{E}^k$ is obtained by taking second

variations of $\mathscr{L}$ with respect to all variables [88, 98]. This can be expressed as

$$\left\langle \boldsymbol{\sigma}_{\hat{\boldsymbol{u}}}, \boldsymbol{\varepsilon}_{\tilde{\boldsymbol{p}}} \right\rangle = \mathscr{L}_{\boldsymbol{pu}} \hat{\boldsymbol{u}}, \tag{5.37a}$$

$$\left\langle B^* \Gamma_{\text{noise}}^{-1} B \hat{\boldsymbol{u}}, \tilde{\boldsymbol{u}} \right\rangle = \mathscr{L}_{\boldsymbol{uu}} \hat{\boldsymbol{u}}, \tag{5.37b}$$

$$\left\langle \frac{\tilde{E}}{1+\nu} \boldsymbol{\varepsilon}_{\hat{\boldsymbol{u}}}, \boldsymbol{\varepsilon}_{\boldsymbol{p}} \right\rangle + \left\langle \frac{\tilde{E}\nu}{(1+\nu)(1-2\nu)} tr(\boldsymbol{\varepsilon}_{\hat{\boldsymbol{u}}}) \boldsymbol{I}, \boldsymbol{\varepsilon}_{\boldsymbol{p}} \right\rangle = \mathscr{L}_{E\boldsymbol{u}} \hat{\boldsymbol{u}}, \tag{5.37c}$$

$$0 = \mathscr{L}_{\boldsymbol{pp}} \hat{\boldsymbol{p}}, \tag{5.38a}$$

$$\left\langle \boldsymbol{\sigma}_{\tilde{\boldsymbol{u}}}, \boldsymbol{\varepsilon}_{\hat{\boldsymbol{p}}} \right\rangle = \mathscr{L}_{\boldsymbol{up}} \hat{\boldsymbol{p}}, \tag{5.38b}$$

$$\left\langle \frac{\tilde{E}}{1+\nu} \boldsymbol{\varepsilon}_{\boldsymbol{u}}, \boldsymbol{\varepsilon}_{\hat{\boldsymbol{p}}} \right\rangle + \left\langle \frac{\tilde{E}\nu}{(1+\nu)(1-2\nu)} tr(\boldsymbol{\varepsilon}_{\boldsymbol{u}}) \boldsymbol{I}, \boldsymbol{\varepsilon}_{\hat{\boldsymbol{p}}} \right\rangle = \mathscr{L}_{E\boldsymbol{p}} \hat{\boldsymbol{p}}, \tag{5.38c}$$

$$\left\langle \frac{\hat{E}}{1+\nu} \boldsymbol{\varepsilon}_{\boldsymbol{u}}, \boldsymbol{\varepsilon}_{\tilde{\boldsymbol{p}}} \right\rangle + \left\langle \frac{\hat{E}\nu}{(1+\nu)(1-2\nu)} tr(\boldsymbol{\varepsilon}_{\boldsymbol{u}}) \boldsymbol{I}, \boldsymbol{\varepsilon}_{\tilde{\boldsymbol{p}}} \right\rangle = \mathscr{L}_{\boldsymbol{p}E} \hat{E}, \tag{5.39a}$$

$$\left\langle \frac{\hat{E}}{1+\nu} \boldsymbol{\varepsilon}_{\tilde{\boldsymbol{u}}}, \boldsymbol{\varepsilon}_{\boldsymbol{p}} \right\rangle + \left\langle \frac{\hat{E}\nu}{(1+\nu)(1-2\nu)} tr(\boldsymbol{\varepsilon}_{\tilde{\boldsymbol{u}}}) \boldsymbol{I}, \boldsymbol{\varepsilon}_{\boldsymbol{p}} \right\rangle = \mathscr{L}_{\boldsymbol{u}E} \hat{E}, \tag{5.39b}$$

$$\left\langle \hat{E}, \Gamma_{\text{pr}}^{-1} \tilde{E} \right\rangle = \mathscr{L}_{EE} \hat{E}. \tag{5.39c}$$

Equations (5.37), (5.38), and (5.39) sequentially represent the derivatives of equation (5.35) with respect to $\boldsymbol{u}$, $\boldsymbol{p}$, and E. Here $\hat{E}$ represents the Newton direction and is found by solving

$$\mathscr{H} \begin{bmatrix} \hat{\boldsymbol{u}} \\ \hat{E} \\ \hat{\boldsymbol{p}} \end{bmatrix} = \begin{bmatrix} \mathscr{L}_{\boldsymbol{uu}} & \mathscr{L}_{\boldsymbol{u}E} & \mathscr{L}_{\boldsymbol{up}} \\ \mathscr{L}_{E\boldsymbol{u}} & \mathscr{L}_{EE} & \mathscr{L}_{E\boldsymbol{p}} \\ \mathscr{L}_{\boldsymbol{pu}} & \mathscr{L}_{\boldsymbol{p}E} & \mathscr{L}_{\boldsymbol{pp}} \end{bmatrix} \begin{bmatrix} \hat{\boldsymbol{u}} \\ \hat{E} \\ \hat{\boldsymbol{p}} \end{bmatrix} = \begin{bmatrix} -\mathscr{L}_{\boldsymbol{u}} \\ -\mathscr{L}_{E} \\ -\mathscr{L}_{\boldsymbol{p}} \end{bmatrix} = \begin{bmatrix} 0 \\ -\mathscr{G}(E) \\ 0 \end{bmatrix}. \tag{5.40}$$

The so-called incremental adjoint displacement $\hat{\boldsymbol{p}}$ satisfies the *incremental adjoint problem* which is derived from the first row of (5.40). In strong form reads

$$-\boldsymbol{\nabla} \cdot \boldsymbol{\sigma}_{\hat{\boldsymbol{p}}} = -B^* B \hat{\boldsymbol{u}} \quad \text{in } \Omega, \tag{5.41a}$$

$$\hat{\boldsymbol{p}} = \boldsymbol{0} \quad \text{on } \Gamma_D, \tag{5.41b}$$

$$\boldsymbol{\sigma}_{\hat{\boldsymbol{p}}} \boldsymbol{n} = \boldsymbol{0} \quad \text{on } \Gamma_N, \tag{5.41c}$$

and the so-called incremental forward displacement $\hat{\boldsymbol{u}}$ satisfies the *incremental forward*

problem derived from the third row of equation (5.40), which in strong form reads

$$-\boldsymbol{\nabla}\cdot\boldsymbol{\sigma}_{\hat{\boldsymbol{u}}} = -\boldsymbol{\nabla}\cdot\left(\frac{\hat{E}}{1+\nu}\boldsymbol{\varepsilon}_{\boldsymbol{u}} + \frac{\hat{E}\nu}{(1+\nu)(1-2\nu)}tr(\boldsymbol{\varepsilon}_{\boldsymbol{u}})\boldsymbol{I}\right) \quad \text{in } \Omega, \tag{5.42a}$$

$$\hat{\boldsymbol{u}} = \boldsymbol{0} \quad \text{on } \Gamma_D, \tag{5.42b}$$

$$\boldsymbol{\sigma}_{\hat{\boldsymbol{u}}}\boldsymbol{n} = \boldsymbol{0} \quad \text{on } \Gamma_N. \tag{5.42c}$$

5.8.2 Finite dimensional formulation

In order to demonstrate the calculation of the posterior covariance matrix Γ_{post} we discuss the finite dimensional representation of the Newtons equation (5.40).

$$\begin{bmatrix} W & 0 & C^T \\ 0 & R & A^T \\ C & A & 0 \end{bmatrix} \begin{bmatrix} \hat{\boldsymbol{u}} \\ \hat{E} \\ \hat{\boldsymbol{p}} \end{bmatrix} = \begin{bmatrix} 0 \\ -g \\ 0 \end{bmatrix}, \tag{5.43}$$

Where $W = B^*\Gamma_{\text{noise}}^{-1}B$ and $R = \Gamma_{\text{pr}}^{-1}$. Thus, the incremental forward variable is found by the third row of the system (5.43)

$$\hat{\boldsymbol{u}} = -C^{-1}A\hat{E}, \tag{5.44}$$

and the incremental adjoint variable by the first row

$$\hat{\boldsymbol{p}} = -C^{-T}W\hat{\boldsymbol{u}} = C^{-T}WC^{-1}A\hat{E}. \tag{5.45}$$

The Newton direction $\hat{E}$ can be identified using the second row of the system (5.43)

$$(R + A^TC^{-T}WC^{-1}A)\hat{E} = -g \tag{5.46}$$

where Hessian matrix is

$$H = (R + A^TC^{-T}WC^{-1}A) \tag{5.47}$$

The data misfit Hessian H_{misfit} in (5.47) is equal to $A^TC^{-T}WC^{-1}A$ and prior covariance matrix Γ_{pr}^{-1} is equal to R. We also introduce prior-preconditioned data misfit Hessian as follows.

$$H = (H_{\text{misfit}} + \Gamma_{\text{pr}}^{-1}) = \Gamma_{\text{pr}}^{-1}(\Gamma_{\text{pr}}H_{\text{misfit}} + I) \tag{5.48}$$

5.9 Results

This section presents two model problems to illustrate the performance of the inverse method described in Section 5.8. The first problem focuses on the inversion of a smooth (sinusoidal) Young's modulus field for a planar cantilever bending. The second problem targets the same inversion parameter but for a three dimensional helical structure. The observation data $\boldsymbol{u}^{obs}$ is synthesized by solving the forward problem described in

Section 5.2 and adding a noise level of 1 percent to the solution. In other words, the signal to noise ratio (SNR) is equal to 100. In what follows, the traction $\boldsymbol{t}$ on the boundary Γ_N is zero, and we consider a nonzero body force $\boldsymbol{f}$.

To solve the inverse problems we used hIPPYlib [106], an inverse problem python-based library. This library contains scalable algorithms for PDE-based deterministic and Bayesian inverse problems. It builds on FEniCS [99, 100], a finite element package that is used to solve the forward problem (5.1).

5.9.1 Cantilever Bending

The domain $\Omega = [0,8] \times [0,0.5]$ for this model problem is a two-dimensional rectangular section of a cantilever (as shown in Figure 5.1). The boundary conditions are the following. On the left boundary, Γ_D, we impose homogeneous Dirichlet condition to model a clamped end, and on Γ_N, we impose a traction-free, i.e., homogeneous Neumann boundary condition.

The goal of this model problem is to identify the Young's modulus E parameter field when Poisson's ratio ν is known (here taken as 0.25). The synthetic observation data $\boldsymbol{u}^{obs}$ for the inversion of E is obtained by simulating the cantilever bending subject to uniform body force $\boldsymbol{f} = (0, 6.5 \times 10^{-3})$ and with a "true" parameter field

$$E = 15.0 - 5.0 \sin\left(\pi\left(\frac{x}{8} - \frac{1}{2}\right)\right), \tag{5.49}$$

to which we add noise as explained above.

The prior is chosen in the following way. The mean is chosen to be zero and the prior covariance matrix is constructed by using the inverse of a Laplacian-like operator, as explained in Section 5.8. For the cantilever bending example, the parameter γ, which controls the smoothness of the parameter field E has a constant value 0.4, and parameter δ is also chosen to be constant 0.1. A one-dimensional representation (at $y = 0.25m$) of the prior mean, standard deviation and samples from the Gaussian prior distribution are illustrated on the left in Figure 5.11.

Figure 5.12 shows the synthetic observation data $\boldsymbol{u}^{obs}$, state variable obtained with the true parameter field $\boldsymbol{u}^{true}$, and the solution of the forward problem with the inversion result $\boldsymbol{u}^{inv}$ along the bending neutral axis of the beam (i.e. $y = 0$). This figure shows that the difference between $\boldsymbol{u}^{obs}$ and $\boldsymbol{u}$ is larger toward the right side of the beam.

In Figure 5.13 we compare the variance of the prior with that of the posterior. This result shows that the variance is decreased which can be attributed to the observations. We note that toward the free end of the cantilever (i.e., the right side of the cantilever), where the bending deformation decreases, the variance (i.e., the uncertainty) remains larger. This is because the sensitivity of the observable to the parameter vanishes, hence the data becomes uninformative. More specifically, in this loading scenario the maximum stress

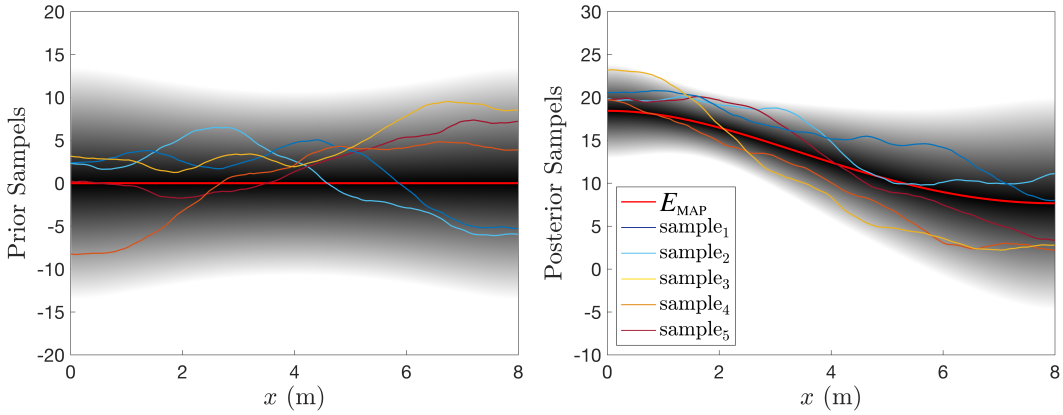

Figure 5.11: The standard deviation (σ) of the prior (left) and the posterior (right) probability distributions are shown in gray color scale in which higher probability density is indicated by darker shading. The prior mean and the MAP point of the posterior are shown in red and samples from the prior and the posterior are shown in different colors.

and strain values occur toward the clamped end of the beam while the free end has zero stress and strain

The Figure 5.14 shows the spectrum of prior-preconditioned data misfit Hessian. The spectrum of this Hessian is a measure of the informativity of the observed data. The preconditioning of the data misfit Hessian with Γ_{pr} is a mean to construct a Hessian that does not depend on the dimension of the problem, instead only depends on how informative the data is [54]. Moreover, to look at the spectrum of the prior-preconditioned data misfit Hessian, similar to [54] we make a low-rank approximation of the Hessian by truncating the eigenvalues that are small relative to 1. In this problem Figure 5.14 shows that only a few of the eigenvalues are larger than one. These large eigenvalues are the modes that direct the Newton's method to the final solution in the parameter space. Much smaller eigenvalues correspond to the noise in the data and do not help to infer the parameter. This is also illustrated by depicting a subset of the eigenvectors of prior-preconditioned data misfit Hessian as shown in Figure 5.15.

5.9.2 Helical Rod Stretching

In this section, we define a model problem for the identification of the elastic properties of a more realistic rod, namely of the helical proteins (sheath) that play a key role in the genome injection mechanism of the bacteriophage T4 virus [4, 4]. The helical sheath proteins on the viral tail are stretched before injection. When the virus attaches to a target cell, the elastic energy of the helical proteins is used to inject the DNA into the target cell. Continuum rod theory is shown to be capable of capturing the important features of this mechanism [4], however the accuracy of continuum modeling is strictly determined by the accurate knowledge of the constitutive law. The methodology presented here can

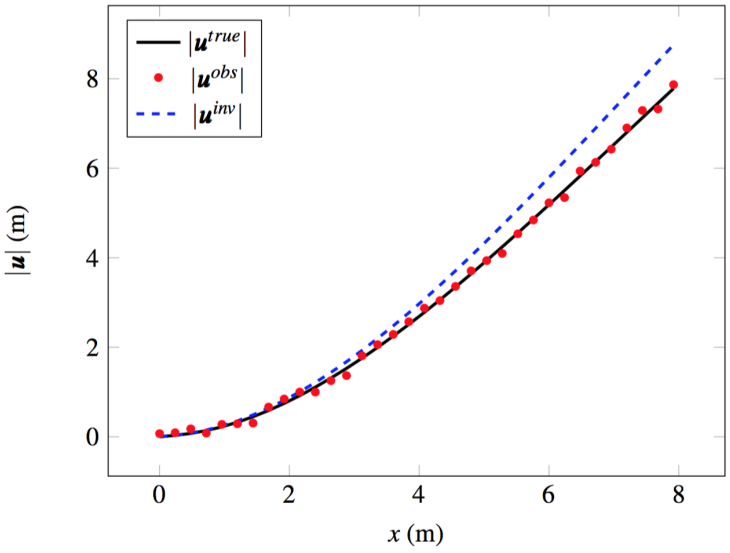

Figure 5.12: The synthetic observation $\boldsymbol{u}^{obs}$, state variable calculated with true parameter field $\boldsymbol{u}^{true}$, and the solution of the forward problem with the inversion results $\boldsymbol{u}^{inv}$ are shown along the bending neutral axis of the beam.

be used not only to estimate the constitutive law of such structures, but also to quantify the degree of uncertainty in the estimations. The problem presented in this section shows how the constitutive law of a helical rod can be estimated using the measurements of the displacement field.

The Poisson ratio ν in this model problem is constant, e.g., $\nu = 0.25$, and the sinusoidal Young's modulus, E, is given by

$$E = 15.0 - 5.0 \sin\left(\pi\left(\frac{x}{20} - \frac{1}{2}\right)\right). \tag{5.50}$$

The geometry for this problem is a helix with radius $R = 1$ mm and pitch $P = 2$ mm. The synthetic observations $\boldsymbol{u}^{obs}$ for this case are generated by stretching the helical structure under a uniform body force $\boldsymbol{f} = (2.2 \times 10^{-3}, 0, 0)$. In this example, the parameter γ has a constant value 1.0, and parameter δ is also chosen to be constant 0.1. In Figure 5.17 we show the variance and samples from the prior and posterior probability distributions. The results show that the variance of the posterior is smaller than that of the prior, which is due to the information we learned from the observations. However, toward the free end of the structure (right hand side in Figure 5.16) as the deformation declines to zero, the data is not informative for accurate identification of the parameter field, therefore the posterior shows a larger variance in this region.

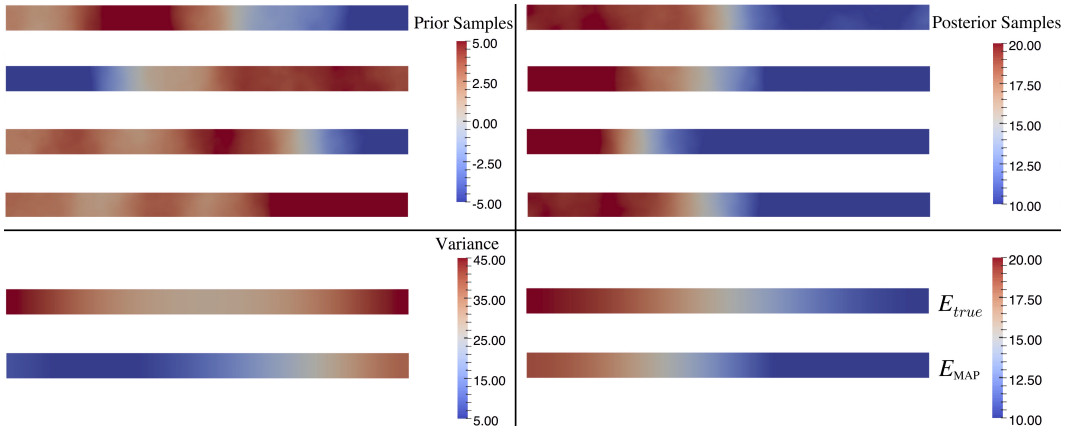

Figure 5.13: Several depictions of the prior (top left) and posterior (top right) using a color scale. The variance σ^2 (bottom left) of the prior (top) and posterior (bottom) is demonstrated in the domain. MAP points versus true parameter field.

5.10 Discussion on Bayesian Inversion

This section presents a Bayesian inversion approach to estimate the Elasticity parameter field for cantilever beams and helical springs from their displacement fields. In deterministic formulation of the inverse problem we have shown that the number of PDE solves for the Newton method is insensitive to the number of inversion parameters, an important requirement especially when the target application is of large scale. This would not be the case with gradient (only)-based methods, as our previous experience shows [88]. While the method has been presented for inversion of a single parameter field E, the extension to inversion of both the Young's modulus and Poisson's ratio is trivial.

We have formulated and solved two model problems to study the invertibility of the Young's modulus. First, we focused on the inversion of a smooth (sinusoidal) parameter field. The second model problem targeted a 3-dimensional parameter field. We found that the reconstruction of the parameter field (MAP points) were close to its true value and the uncertainty in the reconstruction is directly determined by the availability of informative data. For example, on the computational nodes near the free end of the cantilever under pure shear force, where deformations are nearly zero, the posterior probability distribution has large variances which is a measure of the uncertainty.

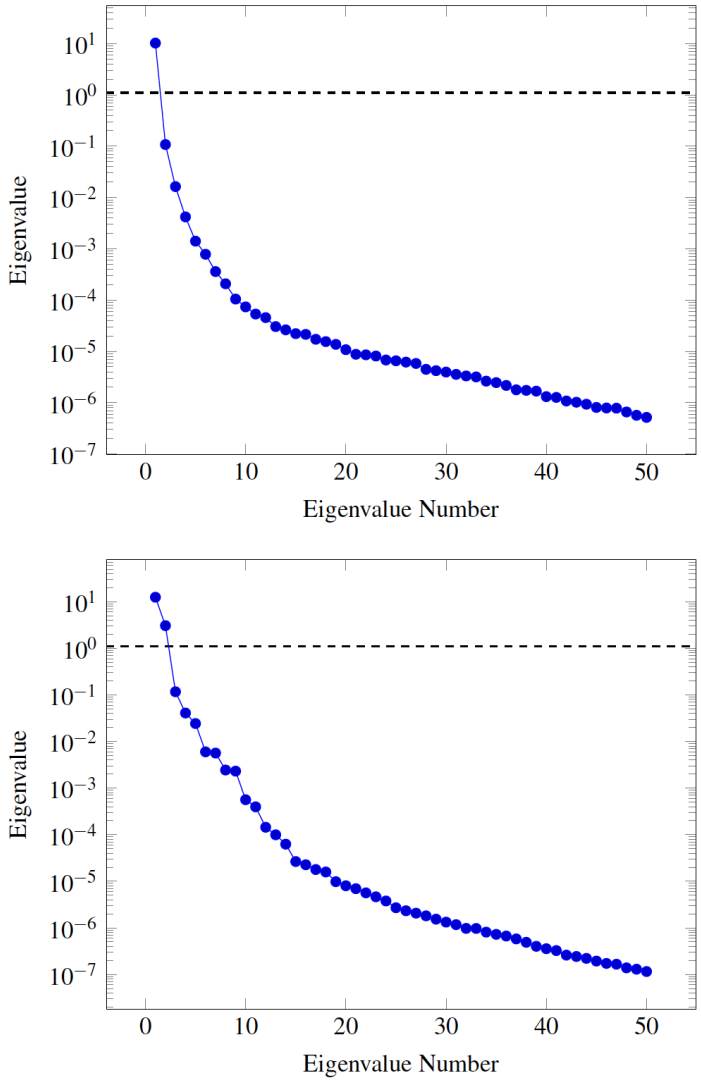

Figure 5.14: Logarithmic plot of the spectrum of prior-preconditioned data misfit Hessian for cantilever problem (top) and the helical rod (bottom).

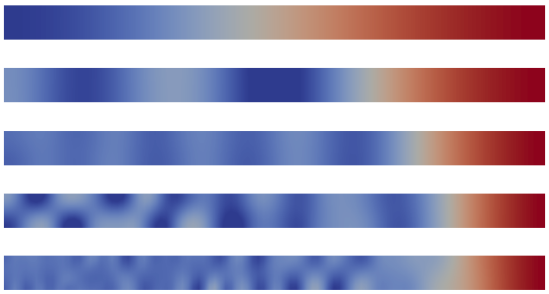

Figure 5.15: Several depictions of the eigenvectors of prior-preconditioned data misfit Hessian in the domain of the cantilever. From top to bottom the eigenvalues correspond to first, fifth, tenth and fiftieth eigenvalue.

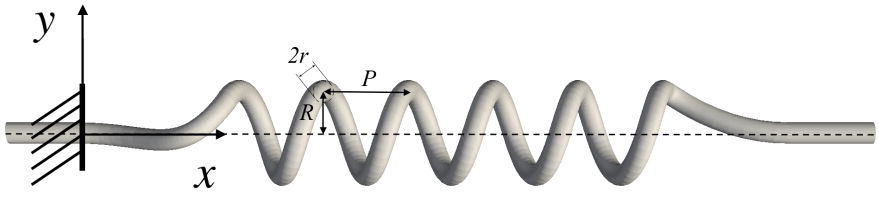

Figure 5.16: The domain of the linear elastic problem modeling a helical rod. The radius of the helix is $R = 1$ mm and its pitch $P = 2$ mm. The overall length of the structure is $L = 20$ mm shown with dashed line and the cross-section of the rod is a circle with radius $r = 0.25$ mm.

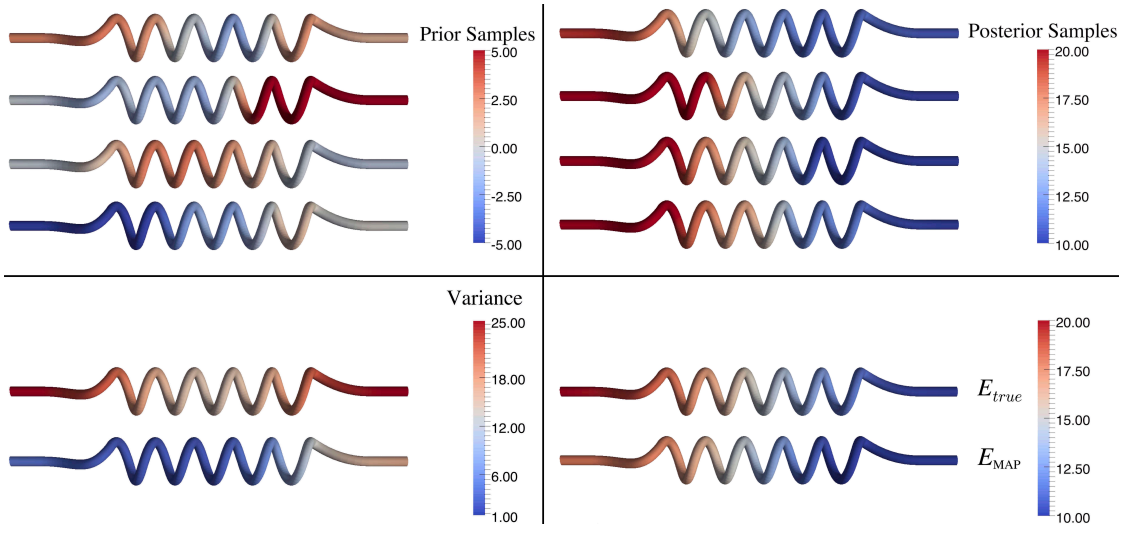

Figure 5.17: Several depictions of the prior (top left) and posterior (top right) using a color scale. The variance σ^2 (bottom left) of the prior (top) and posterior (bottom) is demonstrated in the domain. MAP points versus true parameter field (bottom right).

Chapter 6

STABILITY OF SLENDER STRUCTURES SUBJECTED TO FOLLOWER LOADS

6.1 Introduction

Stability analysis of slender structures subjected to follower loads are important instantiations of nonconservative problems in the theory of elastic stability. A number of thorough surveys of the developments and achievements on the structural stability of nonconservative systems can be found in the literature [107–109]. Conservative loads such as gravitational or electrostatic forces can be written as gradient of a time independent potential function [110]. Nonconservative loads, however, do not fit this criteria; their magnitude and direction depend on the configuration of a structure (e.g., deflection and slope), its velocity, and time. Viscous damping is a commonly encountered example of nonconservative forces which depend on the velocity of a structure. Follower forces are a second type of nonconservative force which, acting either as a point force or a distributed load, always act tangential to the deflection curve of a structure. Reut [111], Pfluger [112], Leipholz [110] and Beck [113] were among the first researchers to analyze the buckling of cantilevers subjected to follower forces. For instance, Beck [113] reports that the critical buckling load for a cantilever subjected to a compressive point load that always remains tangential to the free-end of the cantilever is approximately 10 times larger than for a force with constant direction.

Stability analysis of slender structures subjected to follower loads is critical in several applications such as pipes conveying fluid [114, 115], self-thrust structures [116], and rockets [117]. It is shown that equations motion of disc-brake systems [118] can be mapped to the equations that govern the stability of a cantilever subjected to a compressive and uniformly distributed follower load, the Leipholz column. More recently, follower forces have been studied at smaller scales in microfluidic settings where inertia is negligible. For instance, synthetic filaments comprised of connected paramagnetic beads when actuated are observed to mimic the shapes of beating flagella [119, 120]. Similarly, tunable colloidal chains assembled from chemically tailored Janus particles with controllable polarities can also be tuned to generate oscillatory beating [121–123]. While the length scales in these applications range from around 1-500 μm, dynamical principles underlying their structural stability are similar to classical, large-scale applications; indeed connections between mechanics at multiple length scales have been illustrated in other biological settings [3, 4, 12, 66, 124–127].

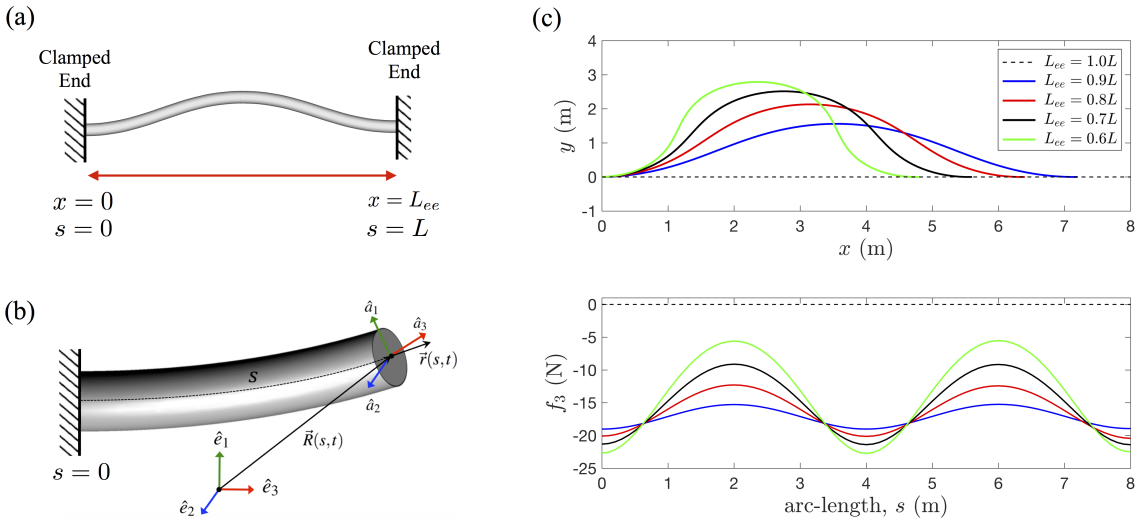

Figure 6.1: (a) Schematic representation of a rod of unstressed length L with fixed-fixed boundary condition (clamped at both ends). The end to end distance when buckled is $L_{\text{ee}} < L$. (b) The motion of material points comprising the cross-section of the rod at arc-length position, s and at time t is determined by tracking the transformations of the body-fixed frame $\hat{a}_i(s,t)$ with respect to the inertial frame of reference $\hat{e}_i$. (c) The shape (top) and pre-stress (bottom) in the buckled state for different values of L_{ee}/L. The dashed line corresponds to the unstressed case $L_{\text{ee}}/L = 1.0$. Pre-stress here is defined as the component of the Internal force in the direction of cross-sectional normal vector $\hat{a}_3(s,t)$ i.e., f_3.

Continuum models are effective approximations for analyzing the post-buckling behavior of inextensible filaments and rods subjected to shearing as well as compressive follower forces [123, 127, 128]. A crucial ingredient in the physical respons of these structures is the dissipation of energy due to viscous drag that provides a means to sustain steady oscillations. Furthermore, in these zero inertia settings, the dissipation rate (and not inertia) provides the time scales controlling the temporal characteristics of the post-buckled state such as the steady-state beating frequency [123, 128–130]. These studies have however focused on the buckling dynamics of free-free, fixed-free, and pinned-free filaments with the base state being a straight non-stressed filament or rod. The role of pre-stress in emergent oscillations driven by active distributed follower forces while important, is however yet to be elucidated.

I focus here on the complementary scenario of a fixed-fixed rod that is, a rod clamped at both ends and pre-stressed by decreasing the end-to-end distance, thereby generating a buckled shape and then subjected to a constant density follower force. In the fixed-free scenario, the lack of constraint at the free-end allow for either lateral oscillations or steady rotations to develop in favorable conditions [123]. In my fixed-fixed

scenario, the slack generated upon initial compression offers the necessary degree of freedom to allow for oscillations. The simulations are three-dimensional, but, by introducing strictly planar perturbations and loads, the oscillations remain planar.

In Section 6.2 of the present chapter, I discuss the modeling of the clamped rod with linear constitutive law. Section 6.3 presents and discusses the results of two case studies pertaining to oscillations under two types of drag forces. Finally, Section 6.4 presents some concluding remarks on the findings of this chapter.

6.2 Model

We consider a rod that is in stress-free state when straight. By displacing one of the clamped ends of the rod toward the other end and forcing the rod to bend and buckle as shown in Figure 6.1(a), I generate pre-stress in the rod. Thus, pre-stress is controlled by the end-to-end length of the rod, $L_{ee} < L$, here the slack being $L - L_{ee}$.

The continuum rod model that I use is explained in Chapter 3. Both shear and stretch deformations are negligible for filaments with large slenderness (length/thickness) ratio under compression. So, I assume $\vec{r}(s,t) = \hat{a}_3(s,t) = \hat{t}(s,t)$, where $\hat{t}(s,t)$ is the unit tangent vector along the arc-length. The distributed follower forces and moments in this model are captured by $\vec{F}$ and $\vec{Q}$ in Eqs. (3.1) and (3.2), respectively. In the scenario of fixed-fixed rod, I consider the effect of distributed follower forces in tangential direction (along $\hat{a}_3(s,t)$) in this section. Here for simplicity of notation, I refer to this tangential follower force density by scalar F.

The differential equations of equilibrium and compatibility (3.1)-(3.4) have to be solved together with a constitutive law relating the deformations to the restoring forces. The constitutive law, for an isotropic and linearly elastic rod takes the form of an algebraic constraint:

$$\vec{q}(s,t) = \underline{\mathbf{B}}(s)\vec{\kappa}(s,t). \tag{6.1}$$

The matrix $\underline{\mathbf{B}}$ in Eq. (6.1) encodes the bending and torsional stiffness moduli of the rod. By choosing the body-fixed frames of reference to coincide with principal axes of rod cross-sections, $\underline{\mathbf{B}}$ can be written as

$$\underline{\mathbf{B}} = \begin{bmatrix} EI_1 & 0 & 0 \\ 0 & EI_2 & 0 \\ 0 & 0 & GI_3 \end{bmatrix}, \tag{6.2}$$

where E is the Young's modulus, G is the shear modulus, and I_1, I_2, and I_3 represent the second moment of area of the rod cross-section about its principal axes. Our choice, as implicit in Figure 6.1(b), implies that subscripts $i = 1,2$ in $\hat{a}_i(s,t)$ represent the rod's axes of bending and $i = 3$ represents torsional axis.

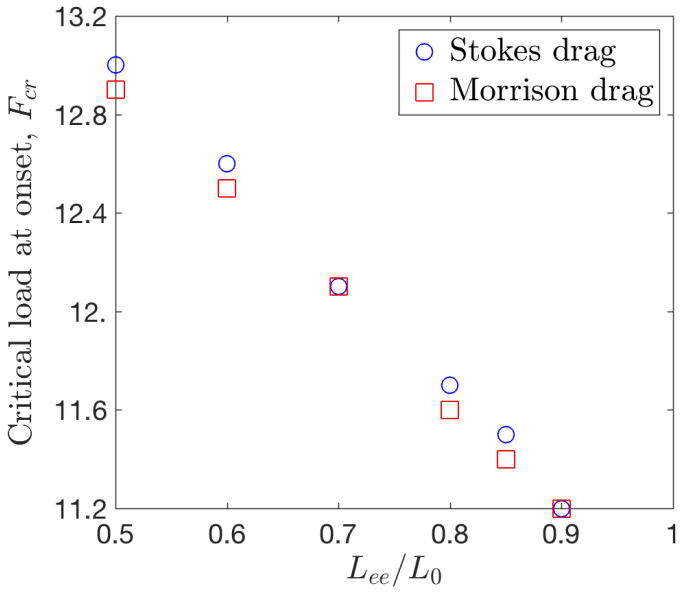

Figure 6.2: Critical load for onset of oscillations F_{cr} versus scaled end-to-end distance L_{ee}/L for both Stokes [S] drag and Morrison [M] drag. I note that the critical loads are roughly the same over the range of pre-stress values investigated.

The *Generalized-*α method [69] is adopted to compute the numerical solution of this system, subjected to necessary and sufficient initial and boundary conditions. A detailed description of this numerical scheme applied to this formulation is given in Chapter 3

6.3 Results

I next present results for the critical value of the follower force density F_{cr} versus end-to-end distance L_{ee}/L and explore how the beating frequency, $\omega(|F|, L_{\text{ee}}/L)$ both at the critical point and for values of the follower force $|F| > F_{\text{cr}}$ depends on the pre-stress. A cylindrical rod with slenderness ratio of 800 is simulated with properties given in Table 6.1. I compare the findings for two types of drag forces, namely Stokes drag [S] and Morrison drag [M] given in Eqs. (6.3) and (6.4), respectively as explained in [27].

$$\vec{F}_{\text{S}} = -\frac{1}{2}\rho_{\text{f}} d\left(C_n \hat{t} \times (\vec{v} \times \hat{t}) + \pi C_t (\vec{v} \cdot \hat{t})\hat{t}\right) \tag{6.3}$$

$$\vec{F}_{\text{M}} = -\frac{1}{2}\rho_{\text{f}} d\left(C_n |\vec{v} \times \hat{t}| \hat{t} \times (\vec{v} \times \hat{t}) + \pi C_t (\vec{v} \cdot \hat{t}) |\vec{v} \times \hat{t}| \hat{t}\right) \tag{6.4}$$

In both equations ρ_{f} and d represent the environment fluid density and diameter of the rod, respectively. Drag coefficients (per unit length) C_n and C_t are given in Table 6.1. In typical scenarios the normal drag coefficient is larger than the tangential coefficient ie,

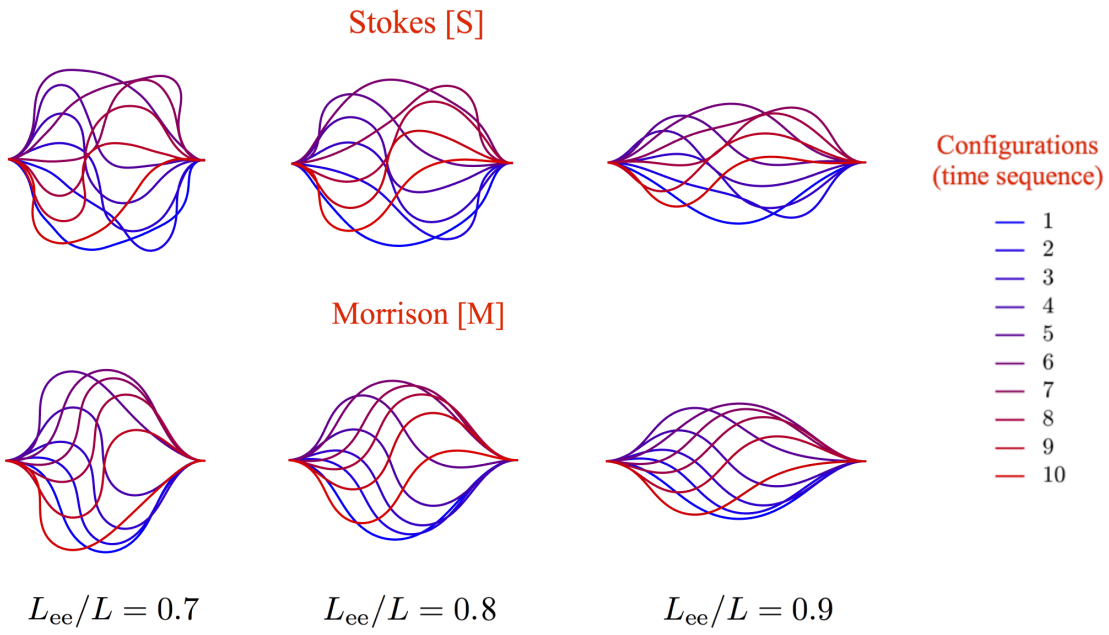

Figure 6.3: Configurations of the rod in sequence (1-10) over one period of oscillation when $|F| = 15$ N/m. The configurations (rod shapes) for Stokes drag are shown on the top, with shapes for Morrison drag shown in the bottom row.

Quantity	Variable	Value	Units
Diameter	d	0.0096	m
Length	L	8	m
Mass per unit length	m	0.2019	kg/m
Young's modulus	E	68.95	GPa
Shear modulus	G	27.58	GPa
Second moment of area	$I_1 = I_2$	4.24×10^{-10}	m^4
Polar moment of area	I_3	8.48×10^{-10}	m^4
Normal drag coefficient	C_n	0.1	m.s or m^2
Tangential drag coefficient	C_t	0.01	m.s or m^2
Surrounding fluid density	ρ_f	1000	kg/m^3

Table 6.1: Numerical values for the geometric and elastic rod properties and drag coefficients used in the computations.

$C_n > C_t$. For the nonlinear form of the Morrison drag, motivated by filament motions corresponding to high Reynolds number, $C_n/C_t \gg 1$. Strictly speaking, in the Stokes limit, and for motion in a Newtonian fluid, both actual drag coefficients are independent of density, weakly dependent on the diameter of the rod d. and proportional to fluid viscosity (and in fact, differ by a factor of two for very slender rods). Here in order to treat both limits in the same consistent framework, I set the values of these drag coefficients to constants and focus solely on the role of activity embodied in the follower force density and the pre-stress embodied in the ratio L_{ee}/L.

I note that the Stokes [S] form for the drag is linear in the velocity while the Morrison form [M] is quadratic, and hence nonlinear in the velocity. Thus for the same change in configuration and frequency, the Morrison form will result in a larger viscous dissipation per unit length than the Stokes form. Conversely, if we require that the same amount of energy be dissipated, the Stokes limit will be characterized by either higher frequency or by larger amplitude deformations or both.

6.3.1 Benchmark: Critical Force for Beck's Column

In order to benchmark the model presented in this section, I calculate the critical buckling force for the Beck's column and compare it with the values reported. Beck's column is a cantilever subjected to a compressive point load that is always tangential to the free-end of the column. Beck's analysis, published in German [113] and reviewed in English [108] yields the following expression for the critical buckling force, P_{cr} of a cantilever with bending stiffness, EI and length, L in absence of damping dissipation. $P_{cr} \approx 20.51\,(EI/L^2)$. Using the formulation presented in Section 6.2, I investigate the value of the critical buckling force for Beck's column and compare it to the value reported

in the literature. To approach the conditions of a quasi-static simulation and reduce the dynamic effects I apply a compressive follower force, which gradually increases in time, to the free-end of the cantilever. The critical force found by our computational model in absence of viscous drag is approximately $P_{\text{cr}} \approx 20.10\,(EI/L^2)$, which is within two percent error margin of the classical estimated value.

6.3.2 Oscillatory Beating of Fixed-Fixed Rods

In this section I present the results for the post-buckling analysis of pre-stressed rods with fixed-fixed boundary conditions for various values of the the slack (and thus, various values of the pre-stress as well as base curvature). Identifying and characterizing critical points as well as the force-frequency relationship is crucial to designing accurately controllable oscillations.

6.3.2.1 Onset of Oscillations

I study cylindrical rods that are in stress-free state when straight. When both ends of a rod are fixed and clamped, moving one of the clamped ends of the rod toward the other end forces the rod to bend or buckle (c.f., Figure 1(a)). This process generates pre-stress in a rod and thus, pre-stress rates can be controlled by the end-to-end length of the rod, L_{ee} - an example of this is shown in Figure 1(c). Starting from a base state completely determined by the ratio L_{ee}/L, I then apply uniformly distributed follower load, $F\hat{a}_3$ along the rod. When the magnitude of the follower load, $|F| > F_{\text{cr}}$, buckled shapes become unstable and beating oscillations emerge. Figure 6.2 shows the magnitudes of the critical follower load against end-to-end distance for the same rod subjected to two types of drag forces. Surprisingly I observe that critical follower load increases as the amount of pre-stress in the rod increases even though decreasing L_{ee}/L implies more slack. The magnitude of critical follower load found to be nearly the same for both Stokes and Morrison drags (discrepancies being $< 2\%$).

6.3.2.2 Shapes Far From Criticality

Despite the low sensitivity of F_{cr} to the nature of drag law, beating configurations as well as the steady frequency of oscillations are found to be significantly different for Stokes and Morrison drags. This can be explained by the fact that Morrison drag dissipates energy at a higher rate compared to the Stokes drag for the same frequency and mode shapes. Figure 6.3 illustrates how the shape of the rod evolves during one complete oscillation for both Stokes and Morrison drags. I visually observe that configurations of the rod subjected to Stokes drag consist of various shape modes. This suggests that higher order harmonics are stronger in this case. Whereas, for cases subjected to Morrison drag, higher order shapes are not recognizable visually. By looking at the Fourier transformation of any quantity I can also confirm the significance of higher order harmonics in Stokes regime compared to Morrison as is shown in Figure 6.4.

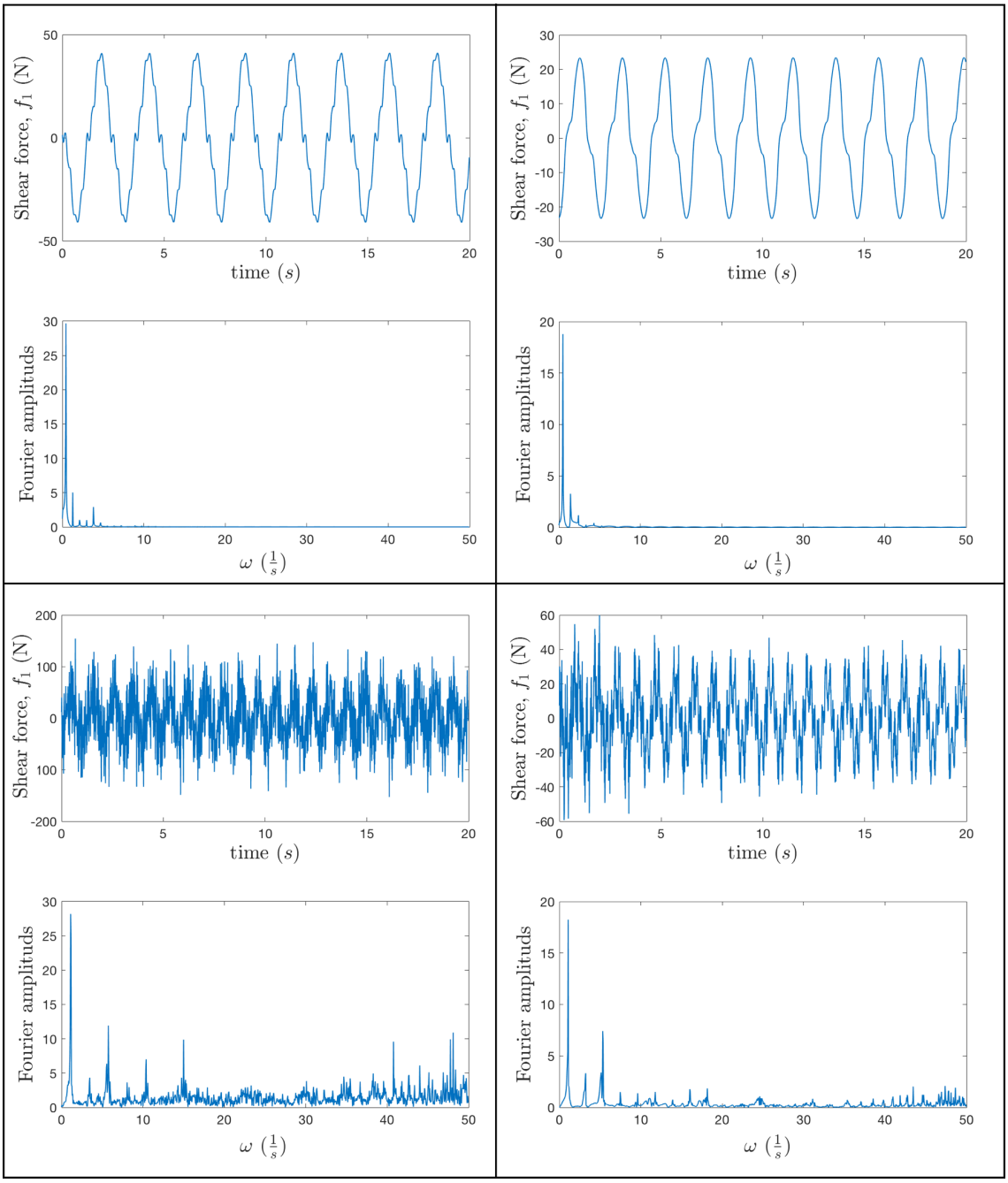

Figure 6.4: Fourier transform (in the time domain) of the shear force at the mid-span length of the rod shows that higher harmonics are damped in the case of the non-linear Morrison drag (top row) more effectively than for the linear Stokes drag (bottom row). The right column of the picture corresponds to $L_{ee}/L = 0.9$ while the left column corresponds to $L_{ee}/L = 0.7$. The ratio of drag coefficients for both cases is 10. Intuitively, we expect this ratio to affect the extent of dampening.

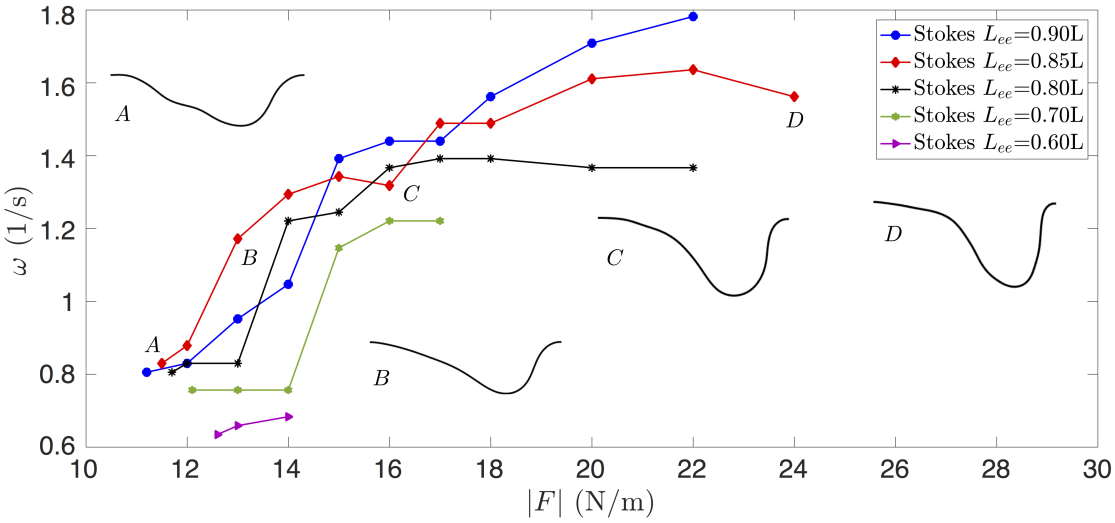

Figure 6.5: Frequency of beating oscillations for rods having various end-to-end distances L_{ee} for the linear Stokes [S] drag case. The frequency is plotted as a function of the distributed follower load. I note that the results for the Stokes drag features possible transitions that may be related to activation of higher order mode shapes as seen from Figure 6.3 (shown alongside).

With the computational model proposed here I next systematically investigate the effect of pre-stress and the follower force on the of frequency beating oscillations and emergent shapes. Figures 6.5 and 6.6 illustrate the frequency of beating oscillations for rods under various end-to-end distances and subjected to both types of viscous drag. I observe that frequency of oscillations under Stokes drag undergoes a sudden increase once the magnitude of the distributed follower load reaches a *second critical limit*. Such a behavior is absent under Morrison drag. Also for a region where magnitude of the distributed follower load is below 18 N/m I observe that larger pre-stress (or smaller end-to-end) distance results in smaller beating frequency. This pattern is also evident under the Stokes drag but only in the region in which the magnitude of the distributed follower load is above 18 N/m.

Examining the force dependence of the beating filaments subject to Morrison type drag forces more closely in Figure 6.6 (a), I find the frequencies in the limit $|F| \gg F_{\text{cr}}$ follow $\omega \sim |F|^{5/6}$. In the complementary analysis of a cantilever subject to follower forces moving under Stokesian drag conditions the exponent was found to be $4/3$ [123]. This scaling relationship was derived using a combination of dimensional analysis and a power balance for steady stable beating to occur. Here, I use a similar analysis to obtain the relationship between the frequency of beating and the follower force density for the Morrison drag case.

6.3.2.3 Stable Frequencies at Large $|F|$ for Morrison Drag

When oscillations reach steady state, the rate at which energy is input into the system due to the action of the nonconservative follower forces balances the rate at which energy is dissipated by the fluid drag,

$$\text{Active energy/time} \approx \text{Dissipation/time} \tag{6.5}$$

The rate at which active energy enters the system is proportional to the magnitude of the follower force (follower force density multiplied by a characteristic length) multiplied by a characteristic speed inherent to the oscillations. For very large F or small L_{ee}/L, the effect of the slack and indeed of the boundary (end to end distance L_{ee}) becomes negligible; instead, the oscillatory wavelength and amplitude are determined by a emergent length scale λ over which compression can be accommodated. Both of these deductions are consistent with the curves plotted in Figure 6.6. Figure 6.6(a) illustrates how the curves for various L_{ee}/L bunch together as $|F|/F_{cr} \gg 1$. Similarly from Figure 6.6(b), I see that the frequency curve is flatter for $|F| = 34$ N/m than for 15 N/m. Thus, the rate at which active energy is generated (with time scale here chosen as a period of oscillation) is

$$\text{Active energy} \sim (|F|\lambda)(\lambda\omega). \tag{6.6}$$

Energy dissipated by the drag for the Morrison case is proportional to the velocity squared, times the velocity of oscillations; energy is then dissipated in the system following

$$\text{Dissipation} \sim (C_{\text{eff}}\lambda^2\omega^2)\lambda(\lambda\omega), \tag{6.7}$$

where C_{eff} is the effective drag coefficient. Combining the Eqs. (6.5)-(6.7) I can find the following relationship.

$$\omega^2 \sim \frac{|F|}{C_{\text{eff}}\lambda^2} \tag{6.8}$$

relating the frequency ω to the follower force density.

To estimate λ, I examine the shapes of the buckled rod relative to the base state noting that activity arises not from the pre-stressed values of f_3 but solely from $|F|$. Assuming that the shape is dominated by the follower force (with pre-stress playing a possibly subdominant part), I examine the moments acting on the rod and use dimensional analysis to obtain,

$$\lambda \sim \left(\frac{EI}{|F|}\right)^{\frac{1}{3}}. \tag{6.9}$$

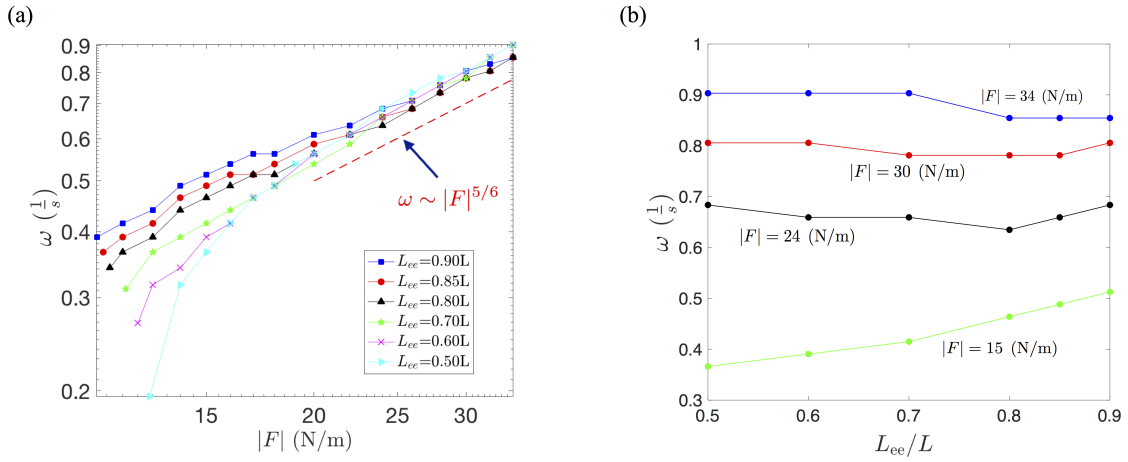

Figure 6.6: (a) Frequency for the Morrison [M] drag plotted as a function of the force density $|F|$ re-plotted in logarithmic scales to illustrate two salient features - (i) as the follower force increases to values much larger than the critical values, the effect of the pre-stress diminishes, and (ii) the frequencies in the limit $|F| \gg F_{\text{cr}}$ scales roughly as $|F|$ - note that for the case of a free cantilever subject to follower forces, I obtain using a scaling argument $\omega \sim |F|^{\frac{5}{6}}$. (b) Emergent frequency plotted as a function of the scaled end to end distance showing non-monotonic behavior indicating competition between geometric flexibility (the slack $1 - L_{\text{ee}}/L$ and the pre-stress f_3 in setting the frequency ω at fixed values of $|F|$.

Substituting (13) in (12) yields

$$\omega \sim \frac{1}{\sqrt{C_{\text{eff}}}} \left(\frac{|F|^{\frac{5}{2}}}{EI} \right)^{\frac{1}{3}} \sim |F|^{\frac{5}{6}}. \tag{6.10}$$

Figure 6.6(a) shows that our simulations follow the scaling $\omega \sim |F|^{\frac{5}{6}}$ for $|F| \gg F_{\text{cr}}$ with the force-frequency curves converging to a universal curve. This suggests that pre-stress (L_{ee}) has a significant effect on response frequency close to the onset of oscillations but not for $|F| \gg F_{\text{cr}}$.

6.4 Discussion and Conclusions

In this chapter I discussed the application of a computational rod model to analyze the buckling stability as well as the post-buckling oscillations of slender structures subjected to compressive follower loads. Simulations were first benchmarked with previous findings on magnitude of the critical buckling force for Beck's column. I focused on slender rods that maintain a straight shape corresponding to their stress-free state (i.e.,

having no intrinsic curvature and twist) with both ends clamped. By moving one end of the rod toward the other end, the structure undergoes buckling and the end-to-end distance represents a measure of the amount of pre-stress in the rod. I found that beyond a critical value of distributed and compressive follower loads the buckled shapes become unstable and oscillatory beating emerges. The magnitude of the critical follower load increases as the magnitude of the pre-stress in the structure increases. I also observed that frequency of the oscillations as well as the configuration of the rod are significantly influenced by the type of drag law used in modeling. Morrison drag induces higher dissipation rate than Stokes drag, therefore, under identical circumstances many more harmonics are discernible in the oscillations of a rod subjected to Stokes drag. Moreover, for the rods subjected to Stokes drag I observed that frequency of oscillations as a function of follower load undergoes a sudden increase once the magnitude of the distributed follower load reaches a *second critical limit*. Our results provide a starting point to systematically investigate the interplay between geometry, elasticity, dissipation and activity towards designing bio-inspired multi-functional, synthetic structures to move and manipulate fluid at various length scales.

Chapter 7

SUMMARY, CONCLUSIONS, AND FUTURE WORK

7.1 Summary and Major Conclusions

In fulfillment of the primary purpose of this dissertation which I defined as showing the possibility of developing inverse methods for identification of constitutive laws of slender structures modeled as beams or rods, this dissertation contributes inverse approaches that can use various types of measurements to infer the constitutive law of slender structures. A family of inverse approaches directly based on the rod model formulation is developed and analyzed for robustness of the constitutive law estimations. Next, an inverse problem governed by the linear elastic equation is presented to reconstruct the non-homogeneous Lamé parameter field from synthetic observations of the displacement field under cantilever loading. Finally, the inverse problem of identifying Young's modulus field from synthetic observations of the displacement field in a Bayesian inference framework is developed and tested in two scenarios.

This dissertation also contributes a computational rod model that describes the nonlinear dynamics of slender structures with user-defined nonlinear constitutive laws. Proposed formulation is benchmarked by comparing the dynamical solution with known equilibrium solution in case of a quasi-static (slow) loading. The model is then employed in several case studies that explore the stability of slender structures subjected to non-conservative follower loads. The description and the scope of major contributions of this dissertation are summarized in the following.

- Effect of Softening Nonlinearities of Constitutive Law on Buckling

I present the analytical solution for the buckling of a continuous fixed-free rod with cubic nonlinear constitutive law using perturbation analysis. The novel contribution of this work is to demonstrate three distinct regimes in the post-buckling solution, namely stable, unstable, and partially stable regimes. While the existing literature only report either stable or unstable post-buckling regimes, by investigating the convergence of the solutions to the perturbation problem the existence of partially stable buckling regime is revealed.

- An Efficient and Accurate Computational Rod Model with User-Defined Constitutive Law

To implement any arbitrary user-defined constitutive law in a computational rod model I contributed a simple and fast method. By expanding the user-input constitutive law function in a polynomial series and using the derivative of the series in the numerical formulation, this method avoids symbolic differentiation which is computationally undesirable. The method automatically modifies the Jacobian term based on the coefficients in the series expansion and is found to be as accurate as symbolic differentiation, yet significantly faster for the two case studies of hardening and softening constitutive laws in the force-extension behavior of a helical spring.

- An Inverse Approach Directly Based on Forward Rod Model for Nonlinear Constitutive Laws

Several inverse algorithms of a computational inverse method are developed, and analyzed for robustness with respect to numerical noise in the input data. The algorithms use the dynamic deformation data to estimate the constitutive laws of slender structures and can employ different combination of kinematic variables to estimate the restoring forces and moments in the filament. However, in all the algorithms, it is consistently found that the curvature and twist vector $\vec{\kappa}$ is the most crucial input compared to velocities, for example. The choice of the input variables determines how many steps will be involved in the method. Thus, the number of numerical integrations and differentiations vary in each algorithm and directly affect the estimation of the constitutive law. In this work I used the deformation data obtained from forward rod model simulations of planar bending with nonlinear constitutive law. Through robustness analysis it is found that the methods, in general, are more sensitive to the noise in curvature than the noise in velocity and angular velocity.

- An Adjoint-Based Inverse Approach for the Lamé Parameter field in an Elastic Model of Slender Structures

I have formulated and solved two model problems to study the invertibility of the Lamé parameter field from synthetic observations in a deterministic framework. First, I focused on the inversion of a smooth (sinusoidal) Lamé parameter field for different Signal to Noise Ratios. I found that the reconstructions converge to the true Lamé parameter field as the noise in the synthetic observations decreases. The second model problem targeted a discontinuous parameter field. The results for this problem show that while I was able to reconstruct the location of the discontinuity, application of Tikhonov regularization smoothed out the sharp edges.

- Bayesian Quantification of the Parameter Uncertainty in Linear Elastic Model

After a deterministic inverse solution is found for the linear elastic model of slender structures, the question is how much confidence we can have in the inverse solution.

To answer this question, I turned to the framework of Bayesian inference, which provides a systematic means of quantifying uncertainty in the solution of the inverse problem.

I have formulated and solved two model problems to study the invertibility of the Young's modulus. First, I focused on the inversion of a smooth (sinusoidal) parameter field. The second model problem targeted a 3-dimensional parameter field. I found that the reconstruction of the parameter field (MAP points) were close to its true value and the uncertainty in the reconstruction is directly determined by the availability of informative data. For example, on the computational nodes near the free end of the cantilever under pure shear force, where deformations are nearly zero, the posterior probability distribution has large variances which is a measure of the uncertainty. Identifying such relationships and patters can be used in optimal experimental design to obtain most informative data for identification of uncertain parameters.

- Follower Forces in Pre-Stressed Clamped Filaments Mimic Oscillatory Beating of Active Filaments

I employed the computational rod model to characterize the buckling stability as well as the post-buckling oscillations of slender structures subjected to compressive follower loads. Previous studies have focused on the buckling dynamics of free-free, fixed-free, and pinned-free filaments with the base state being a straight non-stressed filament or rod. The role of pre-stress in emergent oscillations driven by active distributed follower forces is analyzed in this dissertation. I focused on slender rods with no intrinsic curvature and twist with both ends clamped. By moving one end of the rod toward the other end, the structure undergoes buckling and the end-to-end distance represents a measure of the amount of pre-stress in the rod. I found that beyond a critical value of distributed and compressive follower loads the buckled shapes become unstable and oscillatory beating emerges. The magnitude of the critical follower load increases as the magnitude of the pre-stress in the structure increases. I also observed that frequency of the oscillations as well as the configuration of the rod are significantly influenced by the type of drag law used in modeling. Morrison drag induces higher dissipation rate than Stokes drag, therefore, under identical circumstances many more harmonics are discernible in the oscillations of a rod subjected to Stokes drag. Moreover, for the rods subjected to Stokes drag I observed that frequency of oscillations as a function of follower load undergoes a sudden increase once the magnitude of the distributed follower load reaches a second critical limit.

7.2 Future Work

The analysis of oscillatory beating of slender structures provide a starting point to systematically investigate the interplay between geometry, elasticity, dissipation and activity towards designing bio-inspired multi-functional, synthetic structures. Target applications include to move and manipulate fluid at various length scales, e.g., nano mixers

or swimming nano robots. Out of plane oscillations and three-dimensional rotary motion of active filaments is also another potential extension of this work. The three-dimensional formulation of our computational rod model is well suited to such scenarios.

To date, in all inverse models I have employed synthetic observations to study the performance of the proposed methods, as well as to probe the limits of reconstructability of the elasticity parameters. A natural extension of this work shall be to apply the adjoint-based and Bayesian inversion frameworks to more realistic applications, such as constitutive modeling of microtubules and nano-wires from their MD simulations and data obtained from physical experiments. The potential of success with such applications lies in extending the inverse method to three-dimensional cases, and to observation data in dynamic equilibrium. In real applications the use of static or dynamic model is determined by the availability of the measurements. Furthermore, for nano-scale filaments, it is important to account for the effect of thermal fluctuations in the observation data, which on one hand corrupts the deterministic data, but on the other hand provides information by itself on the deformability of the nano-scale filaments.

Yet another extension can be to include total variation regularization, known to preserve sharp interfaces [50], in the adjoint-based inversion framework. Finally, it is also important to consider nonlinearity in the constitutive laws without any a priori assumption on its form. Hence, the inverse methods based on linear elastic model can be extended to more general elastic models with nonlinear forms of constitutive law.

BIBLIOGRAPHY

[1] D. Swigon, B. D. Coleman, W. K. Olson, Modeling the lac repressor-operator assembly: the influence of DNA looping on lac repressor conformation, Proceedings of the National Academy of Sciences 103 (26) (2006) 9879–9884.

[2] T. D. Lillian, S. Goyal, J. D. Kahn, E. Meyhfer, N. Perkins, Computational analysis of looping of a large family of highly bent dna by laci, Biophysical Journal 95 (12) (2008) 5832 – 5842.

[3] A. Maghsoodi, A. Chatterjee, I. Andricioaei, N. C. Perkins, Dynamic Model Exposes the Energetics and Dynamics of the Injection Machinery for Bacteriophage T4, Biophysical Journal 113 (1) (2017) 195–205.

[4] A. Maghsoodi, A. Chatterjee, I. Andricioaei, N. C. Perkins, A First Model of the Dynamics of the Bacteriophage T4 Injection Machinery, Journal of Computational and Nonlinear Dynamics 11 (4) (2016) 041026.

[5] D. Ando, N. Korabel, K. Huang, A. Gopinathan, Cytoskeletal network morphology regulates intracellular transport dynamics, Biophysical Journal 109 (8) (2015) 1574 – 1582.

[6] M. Kikumoto, M. Kurachi, V. Tosa, H. Tashiro, Flexural rigidity of individual microtubules measured by a buckling force with optical traps, Biophysical Journal 90 (5) (2006) 1687 – 1696.

[7] D. Sept, F. C. MacKintosh, Microtubule elasticity: Connecting all-atom simulations with continuum mechanics, Phys. Rev. Lett. 104 (2010) 018101.

[8] T. Hawkins, M. Mirigian, M. S. Yasar, J. L. Ross, Mechanics of microtubules, Journal of Biomechanics 43 (1) (2010) 23 – 30.

[9] J. Howard, Mechanics of Motor Proteins and the Cytoskeleton, Sinauer Associates, Sunderland, 2001.

[10] A. D. Bicek, E. Tuzel, A. Demtchouk, M. Uppalapati, W. O. Hancock, D. M. Kroll, D. J. Odde, Anterograde microtubule transport drives microtubule bending in llc-pk1 epithelial cells, Molecular biology of the cell 20 (12) (2009) 2943–2953.

[11] J. C. Simo, J. E. Marsden, P. S. Krishnaprasad, The hamiltonian structure of nonlinear elasticity: The material and convective representations of solids, rods, and plates, Archive for Rational Mechanics and Analysis 104 (2) 125–183.

[12] S. Goyal, N. C. Perkins, C. L. Lee, Nonlinear Dynamics and Loop Formation in Kirchhoff Rods with Implications to the Mechanics of DNA and Cables, Journal of Computational Physics 209 (1) (2005) 371–389.

[13] W. Hwang, in: S. De, W. Hwang, E. Kuhl (Eds.), Multiscale Modeling in Biomechanics and Mechanobiology, 2015, pp. 63–83.

[14] S. Neukirch, G. van der Heijden, Geometry and mechanics of uniform n-plies: from engineering ropes to biological filaments, Journal of Elasticity 69 (1-3) (2002) 41–72.

[15] I. Klapper, Biological applications of the dynamics of twisted elastic rods, Journal of Computational Physics 125 (2) (1996) 325 – 337.

[16] K. A. Hoffman, Methods for determining stability in continuum elastic-rod models of DNA, Philosophical Transactions of the Royal Society of London A: Mathematical, Physical and Engineering Sciences 362 (1820) (2004) 1301–1315.

[17] S. Goyal, N. C. Perkins, J. C. Meiners, Resolving the Sequence-Dependent Stiffness of DNA Using Cyclization Experiments and a Computational Rod Model, Journal of Computational and Nonlinear Dynamics 3 (2008) 011003.

[18] A. Hilfinger, A. K. Chattopadhyay, F. Jülicher, Nonlinear dynamics of cilia and flagella, Phys. Rev. E 79 (2009) 051918.

[19] Z. Qin, M. J. Buehler, L. Kreplak, A multi-scale approach to understand the mechanobiology of intermediate filaments, Journal of Biomechanics 43 (1) (2010) 15 – 22.

[20] R. E. Goldstein, A. Goriely, Dynamic buckling of morphoelastic filaments, Phys. Rev. E 74 (2006) 010901.

[21] T. Odijk, Microfibrillar buckling within fibers under compression, The Journal of Chemical Physics 108 (16) (1998) 6923–6928.

[22] A. Kumar, S. Mukherjee, J. T. Paci, K. Chandraseker, G. C. Schatz, A rod model for three dimensional deformations of single-walled carbon nanotubes, International Journal of Solids and Structures 48 (20) (2011) 2849 – 2858.

[23] Y. Chen, B. L. Dorgan, D. N. McIlroy, D. Eric Aston, On the importance of boundary conditions on nanomechanical bending behavior and elastic modulus determination of silver nanowires, Journal of Applied Physics 100 (10).

[24] C. R. Calladine, H. R. Drew, B. F. Luisi, A. A. Travers, Understanding DNA, the Molecule and How It Works, Elsevier Academic Press, Amsterdam, 2004.

[25] S. Goyal, T. Lillian, S. Blumberg, J. C. Meiners, E. Meyhofer, N. C. Perkins, Intrinsic Curvature of DNA Influences LacR-Mediated Looping, Biophysical Journal 93 (12) (2007) 4342–4359.

[26] S. Goyal, N. Perkins, Looping mechanics of rods and DNA with non-homogeneous and discontinuous stiffness, International Journal of Non-Linear Mechanics 44.

[27] S. Goyal, N. Perkins, C. L. Lee, Non-linear dynamic intertwining of rods with self-contact, International Journal of Non-Linear Mechanics 43 (1) (2008) 65–73.

[28] T. E. Cloutier, J. Widom, Spontaneous Sharp Bending of Double-Stranded DNA, Molecular Cell 14 (3) (2004) 355–362.

[29] P. A. Wiggins, R. Phillips, P. C. Nelson, Exact Theory of Kinkable Elastic Polymers, Physical Review E 71 (2).

[30] S. Swati Verma, Goyal, H. J. Palanthandalam-Madapusi, Simulation based analysis of constitutive behavior of microtubules, in: Asian Conference on Mechanics of Functional Materials and Structures, 2012, pp. 679–681.

[31] S. Fatehiboroujeni, S. Goyal, Deriving mechanical properties of microtubules from molecular simulations, Biophysical Journal 110 (3, Supplement 1) (2016) 129a.

[32] R. L. Fosdick, R. D. James, The elastica and the problem of the pure bending for a non-convex stored energy function, Journal of Elasticity 11 (2) (1981) 165–186.

[33] P. Gupta, A. Kumar, Effect of material nonlinearity on spatial buckling of nanorods and nanotubes, Journal of Elasticity 126 (2) (2017) 155–171.

[34] M. L. Smith, T. J. Healey, Predicting the Onset of DNA Supercoiling Using a Nonlinear Hemitropic Elastic Rod, International Journal of Non-linear Mechanics 44.

[35] H. W. Haslach, Post-buckling behavior of columns with non-linear constitutive equations, International Journal of Non-Linear Mechanics 20 (1) (1985) 53 – 67.

[36] K. K. Baczynski, Buckling instabilities of semiflexible filaments in biological systems, Ph.d. dissertation, University of Potsdam (2009).

[37] S. Geggier, A. Vologodskii, Sequence dependence of DNA bending rigidity, Proceedings of the National Academy of Sciences 107 (35) (2010) 15421–15426.

[38] R. S. Manning, J. H. Maddocks, J. D. Kahn, A Continuum Rod Model of Sequence-Dependent DNA Structure, Journal of Chemical Physics 105 (13) (1996) 5626–5646.

[39] S. B. Smith, L. Finzi, C. Bustamante, Direct mechanical measurements of the elasticity of single DNA molecules by using magnetic beads, Science 258 (5085) (1992) 1122–1126.

[40] C. Deufel, S. Forth, C. R. Simmons, S. Dejgosha, M. D. Wang, Nanofabricated quartz cylinders for angular trapping: DNA supercoiling torque detection, Nature Methods 4 (3) (2007) 223–225.

[41] P. J. Hagerman, Flexibility of DNA, Annual Review of Biophysics and Biophysical Chemistry 17 (1988) 265–286.

[42] C. G. Baumann, S. B. Smith, V. A. Bloomfield, C. Bustamante, Ionic Effects on the Elasticity of Single DNA Molecules, Proceedings of the National Academy of Sciences of the United States of America 94 (12) (1997) 6185–6190.

[43] T. R. Strick, J. F. Allemand, D. Bensimon, A. Bensimon, V. Croquette, The Elasticity of a Single Supercoiled DNA Molecule, Science 271 (5257) (1996) 1835–1837.

[44] F. Gittes, B. Mickey, J. Nettleton, J. Howard, Flexural rigidity of microtubules and actin filaments measured from thermal fluctuations in shape., The Journal of Cell Biology 120 (4) (1993) 923–934.

[45] J. Käs, H. Strey, E. Sackmann, Direct imaging of reptation for semiflexible actin filaments .

[46] C. Snoeyink, S. Wereley, Three-dimensional locating of paraxial point source with axicon, Opt. Lett. 37 (11) (2012) 2058–2060.

[47] S. Avril, M. Bonnet, A.-S. Bretelle, M. Grédiac, F. Hild, P. Ienny, F. Latourte, D. Lemosse, S. Pagano, E. Pagnacco, F. Pierron, Overview of identification methods of mechanical parameters based on full-field measurements, Experimental Mechanics 48 (4) (2008) 381–402.

[48] M. Bonnet, A. Constantinescu, Inverse problems in elasticity, Inverse Problems 21 (2) (2005) R1.

[49] H. W. Engl, M. Hanke, A. Neubauer, Regularization of Inverse Problems, Springer Netherlands, 1996.

[50] C. R. Vogel, Computational Methods for Inverse Problems, Frontiers in Applied Mathematics, Society for Industrial and Applied Mathematics (SIAM), Philadelphia, PA, 2002.

[51] C. Snoeyink, S. Wereley, A novel 3d3c particle tracking method suitable for microfluidic flow measurements, Experiments in Fluids 54 (1) (2013) 1453.

[52] H. W. Haslach, Post-buckling behavior of columns with non-linear constitutive equations, International Journal of Non-Linear Mechanics 20 (1) (1985) 53 – 67.

[53] C. Szymczak, T. Mikulski, On post-buckling behavior of columns with cubic constitutive equations, International Journal of Non-Linear Mechanics 25 (1) (1990) 117 – 121.

[54] T. Isaac, N. Petra, G. Stadler, O. Ghattas, Scalable and efficient algorithms for the propagation of uncertainty from data through inference to prediction for large-scale problems, with application to flow of the Antarctic ice sheet, Journal of Computational Physics 296 (2015) 348–368.

[55] C. P. Brangwynne, F. C. MacKintosh, S. Kumar, N. A. Geisse, J. Talbot, L. Mahadevan, K. K. Parker, D. E. Ingber, D. A. Weitz, Microtubules can bear enhanced compressive loads in living cells because of lateral reinforcement, The Journal of Cell Biology 173 (5) (2006) 733–741.

[56] M. P. Murrell, M. L. Gardel, F-actin buckling coordinates contractility and severing in a biomimetic actomyosin cortex, Proceedings of the National Academy of Sciences 109 (51) (2012) 20820–20825.

[57] D. Fygenson, J. Marko, A. Libchaber, Mechanics of microtubule-based membrane extension, Physical Review Letters 79 (22) (1997) 4497–4500.

[58] M. Soheilypour, M. Peyro, S. Peter, M. Mofrad, Buckling behavior of individual and bundled microtubules, Biophysical Journal 108 (7) (2015) 1718 – 1726.

[59] T. Li, A mechanics model of microtubule buckling in living cells, Journal of Biomechanics 41 (8) (2008) 1722 – 1729.

[60] W. Olmstead, D. Mescheloff, Buckling of a nonlinear elastic rod, Journal of Mathematical Analysis and Applications 46 (3) (1974) 609 – 634.

[61] S. S. Antman, Equilibrium states of nonlinearly elastic rods, Journal of Mathematical Analysis and Applications 23 (2) (1968) 459 – 470.

[62] K. Kang, W. Cai, Size and temperature effects on the fracture mechanisms of silicon nanowires: Molecular dynamics simulations, International Journal of Plasticity 26 (9) (2010) 1387 – 1401, special Issue In Honor of David L. McDowell.

[63] W. R. Inc., Mathematica, Version 11.2, champaign, IL, 2017.

[64] A. R. Hinkle, S. Goyal, H. J. Palanthandalam-Madapusi, An Estimation Method of a Constitutive-Law for the Rod Model of DNA Using Discrete-Structure Simulations, ASME 2009 International Design Engineering Technical Conferences and Computers and Information in Engineering Conference IDETC/CIE, San Diego, California, USA (2009) Paper No. DETC2009–87763, pp. 1487–1493.

[65] H. J. Palanthandalam-Madapusi, S. Goyal, Robust estimation of nonlinear constitutive law from static equilibrium data for modeling the mechanics of DNA, Automatica 47 (6) (2011) 1175–1182.

[66] S. Goyal, A dynamic rod model to simulate mechanics of cables and DNA, Ph.d. dissertation in mechanical engineering, University of Michigan (2006).

[67] R. D. Neidinger, Introduction to Automatic Differentiation and MATLAB Object-Oriented Programming, 2010.

[68] G. Kirchhoff, Uber das gleichgewicht und die bewegung eines unendlich dunnen elastischen stabes, J. Reine Angew. Math. (Crelle) 56 (1859) 285–343.

[69] J. Chung, G. M. Hulbert, A Time Integration Algorithm for Structural Dynamics with Improved Numerical Dissipation - the Generalized-Alpha Method, Journal of Applied Mechanics-Transactions of The ASME 60 (2) (1993) 371–375.

[70] C. L. Bottasso, M. Borri, Integrating finite rotations, Computer Methods in Applied Mechanics and Engineering 164 (3) (1998) 307 – 331.

[71] J. Simo, L. Vu-Quoc, A three-dimensional finite-strain rod model. part ii: Computational aspects, Computer Methods in Applied Mechanics and Engineering 58 (1) (1986) 79 – 116.

[72] W. Z. Zhang Zhigang, Qi Zhaohui, F. Huiqing, A spatial euler-bernoulli beam element for rigid-flexible coupling dynamic analysis of flexible structures, J Shock and Vibration 2015.

[73] A. Cardona, M. Geradin, A beam finite element non-linear theory with finite rotations, International Journal for Numerical Methods in Engineering 26 (11) (1988) 2403–2438.
URL http://dx.doi.org/10.1002/nme.1620261105

[74] W. Fan, W. D. Zhu, An accurate singularity-free geometrically exact beam formulation using euler parameters, Nonlinear Dynamics 91 (2) (2018) 1095–1112.

[75] Y. Sun, J. W. Leonard, R. B. Chiou, Simulation of unsteady oceanic cable deployment by direct integration with suppression, Ocean Engineering Ocean Engineering 21 (3) (1994) 243–256.

[76] A. R. Haeusler, K. A. Goodson, T. D. Lillian, X. Wang, S. Goyal, N. C. Perkins, J. D. Kahn, FRET studies of a landscape of Lac repressor-mediated DNA loops, Nucleic Acids Research .

[77] Y. d.-C. C. T. Vincent Miele, Cdric Vaillant, T. Grange, DNA physical properties determine nucleosome occupancy from yeast to fly, Nucleic Acid Researh 36 (2008) 3746–56.

[78] T. C. B. Mithun Biswas, Jorg Langowski, Atomistic simulations of nucleosomes, Computational Molecular Science 3 (2013) 378–392.

[79] A. Balaeff, L. Mahadevan, K. Schulten, Modeling DNA Loops Using the Theory of Elasticity, Physical Review E 73 (3).

[80] T. R. Strick, J. F. Allemand, D. Bensimon, A. Bensimon, V. Croquette, The Elasticity of a Single Supercoiled DNA Molecule, Science 271 (5257) (1996) 1835–1837.

[81] P. J. Hagerman, Flexibility of DNA, Annual Review of Biophysics and Biophysical Chemistry 17.

[82] A. R. Hinkle, S. Goyal, H. J. Palanthandalam-Madapusi, Constitutive-Law Modeling of Microfilaments From Their Discrete-Structure Simulations - A Method Based on an Inverse Approach Applied to a Static Rod Model, ASME Journal of Applied Mechanics 79 (2012) 051005.

[83] A. love, A treatise on the mathematical theory of elasticity. 4th Ed. 1944, New York: Dover publications., dover publications, New York, 1944.

[84] C. Ablow, S. Schechter, Numerical simulation of undersea cable dynamics, Ocean Engineering 10 (1983) 443–457.

[85] A. Rajiv, H. J. Palanthandalam-Madapusi, An Inverse Model Approach for Estimating Constitutive Laws from Dynamic Planar Deformations of Bio-filaments, Proceedings of the Asian Conference on Mechanics of Functional Materials and Structures, New Delhi, India. .

[86] B. Fornberg, Numerical Differentiation of Analytic Functions, ACM Trans. Math. Softw. 7 (4) (1981) 512–526.

[87] S. Fatehiboroujeni, S. Goyal, A. Gramada, A method for identification of the constitutive law of biological filaments from their dynamic equilibria, in: ASME 2015 International Design Engineering Technical Conferences and Computers and Information in Engineering Conference, American Society of Mechanical Engineers, 2015, pp. V006T10A003–V006T10A003.

[88] N. Petra, H. Zhu, G. Stadler, T. J. R. Hughes, O. Ghattas, An inexact Gauss-Newton method for inversion of basal sliding and rheology parameters in a nonlinear Stokes ice sheet model, Journal of Glaciology 58 (211) (2012) 889–903.

[89] A. Tarantola, Inverse Problem Theory and Methods for Model Parameter Estimation, SIAM, Philadelphia, PA, 2005.

[90] J. Kaipio, E. Somersalo, Statistical and Computational Inverse Problems, Vol. 160 of Applied Mathematical Sciences, Springer-Verlag, New York, 2005.

[91] M. E. Gurtin, An Introduction to Continuum Mechanics, Academic Press, Boston, 2003.

[92] M. S. Gockenbach, Understanding and implementing the finite element method, Society for Industrial and Applied Mathematics (SIAM), Philadelphia, PA, 2006.

[93] C. T. Kelley, Iterative Methods for Optimization, SIAM, Philadelphia, 1999.

[94] J. Nocedal, S. J. Wright, Numerical Optimization, 2nd Edition, Springer Verlag, Berlin, Heidelberg, New York, 2006.

[95] F. Tröltzsch, Optimal Control of Partial Differential Equations: Theory, Methods and Applications, Vol. 112 of Graduate Studies in Mathematics, American Mathematical Society, 2010.

[96] M. Hinze, R. Pinnau, M. Ulbrich, S. Ulbrich, Optimization with PDE Constraints, Springer, 2009.

[97] A. Borzì, V. Schulz, Computational Optimization of Systems Governed by Partial Differential Equations, SIAM, 2012.

[98] N. Petra, G. Stadler, Model variational inverse problems governed by partial differential equations, Tech. Rep. 11-05, The Institute for Computational Engineering and Sciences, The University of Texas at Austin (2011).

[99] M. Alns, J. Blechta, J. Hake, A. Johansson, B. Kehlet, A. Logg, C. Richardson, J. Ring, M. Rognes, G. Wells, The fenics project version 1.5, Archive of Numerical Software 3 (100).

[100] A. Logg, K.-A. Mardal, G. Wells, Automated solution of differential equations by the finite element method: The FEniCS book, Vol. 84, Springer Science & Business Media, 2012.

[101] A. Oberai, N. Gokhale, G. Feijo, Solution of inverse problems in elasticity imaging using the adjoint method, Inverse Problems 19 (2) (2003) 297–313, cited By 124.

[102] A. Samani, J. Bishop, D. B. Plewes, A constrained modulus reconstruction technique for breast cancer assessment, IEEE Trans. Med. Imaging 20 (9) (2001) 877–885.

[103] M. S. Richards, P. E. Barbone, A. A. Oberai, Quantitative three-dimensional elasticity imaging from quasi-static deformation: a phantom study, Physics in Medicine and Biology 54 (3) (2009) 757.

[104] B. Jadamba, A. A. Khan, F. Raciti, On the inverse problem of identifying lamé coefficients in linear elasticity, Comput. Math. Appl. 56 (2) (2008) 431–443.

[105] A. A. Oberai, N. H. Gokhale, G. R. Feijo, Solution of inverse problems in elasticity imaging using the adjoint method, Inverse Problems 19 (2) (2003) 297.

[106] U. Villa, N. Petra, O. Ghattas, hIPPYlib: An extensible software framework for large-scale Bayesian inverse problems, codes available at: https://hippylib.github.io.

[107] M. Langthjem, Y. Sugiyama, Dynamic stability of columns subjected to follower loads: A survey, Journal of Sound and Vibration 238 (5) (2000) 809 – 851.

[108] I. Elishakoff, Controversy Associated With the So-Called "Follower Forces": Critical Overview, Applied Mechanics Reviews 58 (2) (2005) 117.

[109] V. V. Bolotin, Dynamic instabilities in mechanics of structures, Appl. Mech. Rev. 55 (1) (1999) R1–R9.

[110] H. H. E. Leipholz, Stability of elastic systems / Horst Leipholz, Sijthoff and Noordhoff Alphen aan den Rijn, the Netherlands, 1980.

[111] V. I. Reut, About the theory of elastic stability, in: Proceedings of the Odessa Institute of Civil and Communal Engineering, No. 1, 1939.

[112] A. Pfluger, Stabilitatsprobleme der Elastostatik, Springer-Verlag, Berlin, 1950.

[113] M. Beck, Die Knicklast des einseitig eingespannten, tangential gedruckten Stabes, ZAMP Zeitschrift fur angewandte Mathematik und Physik 3 (3) (1952) 225–228.

[114] M. P. Païdoussis, Fluid-Structure Interactions: Slender Structures and Axial Flow: Second Edition, 2016.

[115] M. P. Païdoussis, G. X. Li, Pipes conveying fluid: A model dynamical problem, Journal of Fluids and Structures 7 (2) (1993) 137–204.

[116] W. G. Wood, S. S. Saw, P. M. Saunders, The Kinetic Stability of a Tangentially Loaded Strut, Proceedings of the Royal Society A: Mathematical, Physical and Engineering Sciences 313 (1513) (1969) 239–248.

[117] M. Païdoussis, Dynamics of cylindrical structures subjected to axial flow, Journal of Sound and Vibration 29 (3) (1973) 365–385.

[118] B. Kang, C. A. Tan, Parametric instability of a Leipholz column under periodic excitation, Journal of Sound and Vibration 229 (5) (2000) 1097–1113.

[119] R. Dreyfus, J. Baudry, M. L. Roper, M. Fermigier, H. A. Stone, J. Bibette, Microscopic artificial swimmers, Nature 437 (7060) (2005) 862–865.

[120] A. Babataheri, M. Roper, M. Fermigier, O. Du Roure, Tethered fleximags as artificial cilia, Journal of Fluid Mechanics 678 (2011) 5–13.

[121] Y. Sasaki, Y. Takikawa, V. S. R. Jampani, H. Hoshikawa, T. Seto, C. Bahr, S. Herminghaus, Y. Hidaka, H. Orihara, Colloidal caterpillars for cargo transportation, Soft matter 10 (44) (2014) 8813–20.

[122] A. E. Patteson, A. Gopinath, P. E. Arratia, Active colloids in complex fluids, Current Opinion in Colloid & Interface Science 21 (2016) 86 – 96.

[123] R. Chelakkot, A. Gopinath, L. Mahadevan, M. F. Hagan, Flagellar dynamics of a connected chain of active, polar, brownian particles, Journal of the Royal Society, Interface 11 (92) (2014) 20130884.

[124] A. Vaziri, A. Gopinath, Cell and biomolecular mechanics in silico, Nature Materials 7 (1) (2008) 15–23.

[125] A. Gopinath, L. Mahadevan, Elastohydrodynamics of wet bristles, carpets and brushes, Proceedings of the Royal Society A: Mathematical, Physical and Engineering Sciences 467 (2130) (2011) 1665–1685.

[126] A. Vaziri, A. Gopinath, V. S. Deshpande, Continuum-based computational models for cell and nuclear mechanics, Journal of Mechanics of Materials and Structures 2 (6) (2007) 1169–1191.

[127] B. Qin, A. Gopinath, J. Yang, J. P. Gollub, P. E. Arratia, Flagellar kinematics and swimming of algal cells in viscoelastic fluids, Scientific Reports 5.

[128] G. De Canio, E. Lauga, R. E. Goldstein, Spontaneous oscillations of elastic filaments induced by molecular motors, Journal of The Royal Society Interface 14 (136).

[129] G. Herrmann, R. W. Bungay, On the stability of elastic systems subjected to non-conservative forces, Journal of Applied Mechanics, Transactions ASME 31 (3) (1964) 435–440.

[130] P. V. Bayly, S. K. Dutcher, Steady dynein forces induce flutter instability and propagating waves in mathematical models of flagella, Journal of The Royal Society Interface 13 (123).

Appendix A

ANALYTIC SOLUTION OF THE PERTURBATION PROBLEM

In this appendix we present the converged solution to the perturbation problem discussed in Chapter 2. External load, P is solved analytically to 14-th order accuracy, $O(b^{14})$, using a Mathematica manuscript given below. In the following, symbol b is replaced with $\mathbf{b}$ to make the reading of the equation more convenient.

$$
\begin{aligned}
P(\mathbf{b}) =& \pi^{14}\mathbf{b^{12}}\Big(94976832E_1I_1^6L^{12}+278558592\pi^2E_1I_1^5E_2I_2L^{10}-40448240\pi^4E_1I_1^4E_2I_2^2L^8 \\
&+7116301056\pi^6E_1I_1^3E_2I_2^3L^6-188178564\pi^8E_1I_1^2E_2I_2^4L^4+202311368\pi^{10}E_1I_1E_2I_2^5L^2 \\
&-110710077\pi^{12}E_2I_2^6\Big)/(1125899906842624E_1I_1^5L^{26}) \\
&+\pi^{12}\mathbf{b^{10}}\Big(1522368E_1I_1^5L^{10}+4146672\pi^2E_1I_1^4E_2I_2L^8-743040\pi^4E_1I_1^3E_2I_2^2L^6 \\
&+1574984\pi^6E_1I_1^2E_2I_2^3L^4-1915324\pi^8E_1I_1E_2I_2^4L^2 \\
&+1177959\pi^{10}E_2I_2^5\Big)/(2199023255552E_1I_1^4L^{22}) \\
&+\pi^{10}\mathbf{b^8}\Big(204976E_1I_1^4L^8+512416\pi^2E_1I_1^3E_2I_2L^6-101304\pi^4E_1I_1^2E_2I_2^2L^4 \\
&+153960\pi^6E_1I_1E_2I_2^3L^2-109125\pi^8E_2I_2^4\Big)/(34359738368E_1I_1^3L^{18}) \\
&+\pi^8\mathbf{b^6}\Big(464E_1I_1^3L^6+1044\pi^2E_1I_1^2E_2I_2L^4-200\pi^4E_1I_1E_2I_2^2L^2 \\
&+177\pi^6E_2I_2^3\Big)/(8388608E_1I_1^2L^{14}) \\
&+\frac{\pi^6\mathbf{b^4}\left(76E_1I_1^2L^4+148\pi^2E_1I_1E_2I_2L^2-21\pi^4E_2I_2^2\right)}{131072E_1I_1L^{10}} \\
&+\frac{\mathbf{b^2}\left(2\pi^4E_1I_1L^2+3\pi^6E_2I_2\right)}{256L^6}+\frac{\pi^2E_1I_1}{4L^2}+O(\mathbf{b^{14}})
\end{aligned}
\tag{A.1}
$$

Clear All and Restart

```
In[1]:= ClearAll["Global`*"]

In[2]:= Clear["Global`*"]
        ClearAll[f]

In[4]:= Remove["Global`*"]

In[5]:= (*Quit[]*)
```

Left Hand Side of the Euler Equation (2.19)

From linear term in the constitutive law (EI_1 represents $E_1\ I_1$)

```
In[6]:= LHS1 = EI1 (w⁽⁴⁾[s] (1 - w'[s]^2)^(-1) + 4 w'[s] w⁽²⁾[s] w⁽³⁾[s] (1 - w'[s]^2)^(-2) +
          w⁽²⁾[s]^3 (1 + 3 w'[s]^2) (1 - w'[s]^2)^(-3))
```

From cubic term in the constitutive law (EI_2 represents $E_2\ I_2$)

```
In[7]:= LHS2 =
          EI2 (3 w⁽⁴⁾[s] w⁽²⁾[s]^2 (1 - w'[s]^2)^(-2) + 6 w⁽³⁾[s]^2 w⁽²⁾[s] (1 - w'[s]^2)^(-2) +
            24 w⁽³⁾[s] w⁽²⁾[s]^3 w'[s] (1 - w'[s]^2)^(-3) +
            3 w⁽²⁾[s]^5 (1 + 5 w'[s]^2) (1 - w'[s]^2)^(-4))
```

From the external load (P)

```
In[8]:= LHS3 = P w⁽²⁾[s] (1 - w'[s]^2)^(-3/2)
```

Left Hand Side of Eq. (2.19)

```
In[9]:= LHS = LHS1 + LHS2 + LHS3
```

Power Series Expansion of Eq. (2.19)

```
In[10]:= LH = Series[LHS, {w'[s], 0, 13}]

In[11]:= LHS = Normal[LH]
```

Substitution with Perturbation Parameter b

Eq. (2.6)

In[12]:=
```
w[s_] = Sum[wᵢ[s] b^i, {i, 1, 13}]
```

Eq. (2.7)

In[13]:=
```
P = p_cr + Sum[pᵢ b^i, {i, 1, 13}]
```

Eq. (2.6) and Eq. (2.7) are substituted in Eq. (2.19)

In[14]:=
```
LHS
```

Coefficients of various powers of b, up to 14-th order

Coefficient of b^1

In[15]:=
```
coef1 = Coefficient[LHS, b, 1]
```

Coefficient of b^2

In[16]:=
```
coef2 = Coefficient[LHS, b, 2]
```

Coefficient of b^3

In[17]:=
```
coef3 = Coefficient[LHS, b, 3]
```

Coefficient of b^4

In[18]:=
```
coef4 = Coefficient[LHS, b, 4]
```

Coefficient of b^5

In[19]:=
```
coef5 = Coefficient[LHS, b, 5]
```

Coefficient of b^6

In[20]:=
```
coef6 = Coefficient[LHS, b, 6]
```

Coefficient of b^7

In[22]:=
```
coef7 = Coefficient[LHS, b, 7]
```

Coefficient of b^8

In[23]:=
```
coef8 = Coefficient[LHS, b, 8]
```

Coefficient of b^9

In[24]:=
```
coef9 = Coefficient[LHS, b, 9]
```

Coefficient of b^{10}

In[25]:=
```
coef10 = Coefficient[LHS, b, 10]
```

Coefficient of b^{11}

In[26]:=
```
coef11 = Coefficient[LHS, b, 11]
```

Coefficient of b^{12}

In[27]:=
```
coef12 = Coefficient[LHS, b, 12]
```

Coefficient of b^{13}

In[28]:=
```
coef13 = Coefficient[LHS, b, 13]
```

Moment Balance at the Fixed End

Eq. (2.26)

In[29]:=
```
mb = EI1 w''[0] + EI2 w''[0]^3 + P b
```

Coefficients of each power of b - Eq. (2.26)

In[30]:=
```
mbc1 = Coefficient[mb, b, 1]
```

In[31]:=
```
mbc2 = Coefficient[mb, b, 2]
```

In[32]:=
```
mbc3 = Coefficient[mb, b, 3]
```

In[33]:=
```
mbc4 = Coefficient[mb, b, 4]
```

In[34]:=
```
mbc5 = Coefficient[mb, b, 5]
```

In[35]:=
```
mbc6 = Coefficient[mb, b, 6]
```

In[36]:=
```
mbc7 = Coefficient[mb, b, 7]
```

In[37]:=
```
mbc8 = Coefficient[mb, b, 8]
```

In[38]:=
```
mbc9 = Coefficient[mb, b, 9]
```

```
In[39]:= mbc10 = Coefficient[mb, b, 10]

In[40]:= mbc11 = Coefficient[mb, b, 11]

In[41]:= mbc12 = Coefficient[mb, b, 12]

In[42]:= mbc13 = Coefficient[mb, b, 13]
```

Solving for Coefficients of Eq. (2.6) and Eq. (2.7)

Solving the ODE Coefficient of b^1 - Eq. (2.20)

Left Hand Side of the ODE

```
In[43]:= coef1
```

General solution

```
In[44]:= w1[s_] = Simplify[DSolveValue[coef1 == 0, w1[s], s]]
```

Satisfying boundary conditions

```
In[45]:= sol1 = Solve[{w1[0] == 0, w1'[0] == 0, w1''[L] == 0, w1[L] + 1 == 0, mbc1 == 0},
           {pcr, C[1], C[2], C[3], C[4]}]
```

w_1 - Eq. (2.30)

```
In[58]:= {temp} = w1[s] /. sol1

In[59]:= w1[s_] = FullSimplify[temp]
```

P_{cr} – Eq. (2.30)

```
In[60]:= {pcr} = pcr /. sol1

In[61]:= pcr = Simplify[pcr]
```

Solving the ODE Coefficient of b^2

Left Hand Side of the ODE

```
In[62]:= coef2 = FullSimplify[coef2]
```

General solution

```
In[63]:= w2[s_] = Simplify[DSolveValue[coef2 == 0, w2[s], s]]
```

Satisfying boundary conditions

```
In[64]:= sol2 = Solve[{w2[0] == 0, w2'[0] == 0, w2''[L] == 0, w2[L] == 0, mbc2 == 0},
           {p1, C[1], C[2], C[3], C[4]}]
```

w_2 – Eq. (2.31)

```
In[65]:= {temp} = w2[s] /. sol2
```

```
In[66]:= w2[s_] = FullSimplify[temp]
```

$P_{(1)}$ – Eq. (2.31)

```
In[67]:=
         {p1} = p1 /. sol2
```

```
In[68]:= p1 = Simplify[p1]
```

Solving the ODE Coefficient of b^3

Left Hand Side of the ODE

```
In[69]:= coef3 = FullSimplify[coef3]
```

General solution

```
In[70]:= w3[s_] = Simplify[DSolveValue[coef3 == 0, w3[s], s]]
```

Satisfying boundary conditions

```
In[71]:= sol3 = Solve[{w3[0] == 0, w3'[0] == 0, w3''[L] == 0, w3[L] == 0, mbc3 == 0},
           {p2, C[1], C[2], C[3], C[4]}]
```

w_3 – Eq. (2.32)

```
In[72]:= {temp} = w3[s] /. sol3
```

```
In[73]:= w3[s_] = FullSimplify[temp]
```

```
In[74]:= FullSimplify[Cos[Pi s / (2 L)] - Cos[3 Pi s / (2 L)]]
```

$P_{(2)}$ – Eq. (2.32)

```
In[75]:= {p2} = p2 /. sol3
```

```
In[76]:= p2 = Simplify[p2]
```

Solving the ODE Coefficient of b^4

Left Hand Side of the ODE

In[77]:=
```
coef4 = FullSimplify[coef4]
```

General solution

In[78]:=
```
w4[s_] = Simplify[DSolveValue[coef4 == 0, w4[s], s]]
```

Satisfying boundary conditions

In[79]:=
```
sol4 = Solve[{w4[0] == 0, w4'[0] == 0, w4''[L] == 0, w4[L] == 0, mbc4 == 0},
  {p3, C[1], C[2], C[3], C[4]}]
```

w_4 - Eq. (2.33)

In[80]:=
```
{temp} = w4[s] /. sol4
```

In[81]:=
```
w4[s_] = FullSimplify[temp]
```

$P_{(3)}$ - Eq. (2.33)

In[82]:=
```
{p3} = p3 /. sol4
```

In[83]:=
```
p3 = Simplify[p3]
```

Solving the ODE Coefficient of b^5

Left Hand Side of the ODE

In[84]:=
```
coef5 = FullSimplify[coef5]
```

General solution

In[85]:=
```
w5[s_] = Simplify[DSolveValue[coef5 == 0, w5[s], s]]
```

Satisfying boundary conditions

In[86]:=
```
sol5 = Solve[{w5[0] == 0, w5'[0] == 0, w5''[L] == 0, w5[L] == 0, mbc5 == 0},
  {p4, C[1], C[2], C[3], C[4]}]
```

w_5 - Eq. (2.34)

In[87]:=
```
{temp} = w5[s] /. sol5
```

In[88]:=
```
w5[s_] = FullSimplify[temp]
```

$P_{(4)}$ - Eq. (2.34)

In[89]:=
```
{p4} = p4 /. sol5
```

In[90]:=
```
p4 = Simplify[p4]
```

Solving the ODE Coefficient b^6

Left Hand Side of the ODE

In[91]:=
```
coef6 = FullSimplify[coef6]
```

General Solution

In[92]:=
```
w6[s_] = Simplify[DSolveValue[coef6 == 0, w6[s], s]]
```

Satisfying Boundary Conditions

In[93]:=
```
sol6 = Solve[{w6[0] == 0, w6'[0] == 0, w6''[L] == 0, w6[L] == 0, mbc6 == 0},
  {p5, C[1], C[2], C[3], C[4]}]
```

w_6

In[94]:=
```
{temp} = w6[s] /. sol6
```

In[95]:=
```
w6[s_] = FullSimplify[temp]
```

$P_{(5)}$

In[96]:=
```
{p5} = p5 /. sol6
```

In[97]:=
```
p5 = Simplify[p5]
```

Solving the ODE Coefficient b^7

Left Hand Side of the ODE

In[98]:=
```
coef7 = FullSimplify[coef7]
```

General Solution

In[99]:=
```
w7[s_] = Simplify[DSolveValue[coef7 == 0, w7[s], s]]
```

Satisfying the Boundary Condition

In[101]:=
```
sol7 = Solve[{w7[0] == 0, w7'[0] == 0, w7''[L] == 0, w7[L] == 0, mbc7 == 0},
  {p6, C[1], C[2], C[3], C[4]}]
```

w_7

```
In[102]:= {temp} = w7[s] /. sol7
In[103]:= w7[s_] = FullSimplify[temp]
```

$P_{(6)}$

```
In[104]:= {p6} = p6 /. sol7
In[105]:= p6 = Simplify[p6]
```

Solving the ODE Coefficient b^8

General Solution

```
In[106]:= w8[s_] = Simplify[DSolveValue[coef8 == 0, w8[s], s]]
```

Satisfying the Boundary Condition

```
In[107]:= sol8 = Solve[{w8[0] == 0, w8'[0] == 0, w8''[L] == 0, w8[L] == 0, mbc8 == 0},
            {p7, C[1], C[2], C[3], C[4]}]
```

w_8

```
In[108]:= {temp} = w8[s] /. sol8
In[109]:= w8[s_] = FullSimplify[temp]
```

$P_{(7)}$

```
In[110]:= {p7} = p7 /. sol8
In[111]:= p7 = Simplify[p7]
```

Solving the ODE Coefficient b^9

General Solution

```
In[112]:= w9[s_] = Simplify[DSolveValue[coef9 == 0, w9[s], s]]
```

Satisfying the Boundary Condition

```
In[113]:= sol9 = Solve[{w9[0] == 0, w9'[0] == 0, w9''[L] == 0, w9[L] == 0, mbc9 == 0},
            {p8, C[1], C[2], C[3], C[4]}]
```

w_9

```
In[114]:= {temp} = w9[s] /. sol9
In[115]:= w9[s_] = FullSimplify[temp]
```

$P_{(8)}$

```
In[116]:= {p8} = p8 /. sol9
In[117]:= p8 = Simplify[p8]
```

Solving the ODE Coefficient b^{10}

General Solution

```
In[118]:= w10[s_] = Simplify[DSolveValue[coef10 == 0, w10[s], s]]
```

Satisfying the Boundary Condition

```
In[119]:= sol10 = Solve[{w10[0] == 0, w10'[0] == 0, w10''[L] == 0, w10[L] == 0, mbc10 == 0},
            {p9, C[1], C[2], C[3], C[4]}]
```

w_{10}

```
In[120]:= {temp} = w10[s] /. sol10
In[121]:= w10[s_] = FullSimplify[temp]
```

$P_{(9)}$

```
In[122]:= {p9} = p9 /. sol10
In[123]:= p9 = Simplify[p9]
```

Solving the ODE Coefficient b^{11}

General Solution

```
In[124]:= w11[s_] = Simplify[DSolveValue[coef11 == 0, w11[s], s]]
```

Satisfying the Boundary Condition

```
In[125]:= sol11 = Solve[{w11[0] == 0, w11'[0] == 0, w11''[L] == 0, w11[L] == 0, mbc11 == 0},
            {p10, C[1], C[2], C[3], C[4]}]
```

w_{11}

```
In[126]:= {temp} = w11[s] /. sol11
In[127]:= w11[s_] = FullSimplify[temp]
```

$P_{(10)}$

```
In[128]:= {p10} = p10 /. sol11
In[129]:= p10 = Simplify[p10]
```

Solving the ODE Coefficient b^{12}

General Solution

```
In[130]:= w12[s_] = Simplify[DSolveValue[coef12 == 0, w12[s], s]]
```

Satisfying the Boundary Condition

```
In[131]:= sol12 = Solve[{w12[0] == 0, w12'[0] == 0, w12''[L] == 0, w12[L] == 0, mbc12 == 0},
            {p11, C[1], C[2], C[3], C[4]}]
```

w_{12}

```
In[132]:= {temp} = w12[s] /. sol12
In[133]:= w12[s_] = FullSimplify[temp]
```

$P_{(11)}$

```
In[134]:= {p11} = p11 /. sol12
In[135]:= p11 = Simplify[p11]
```

Solving the ODE Coefficient b^{13}

General Solution

```
In[136]:= w13[s_] = Simplify[DSolveValue[coef13 == 0, w13[s], s]]
```

Satisfying the Boundary Condition

```
In[137]:= sol13 = Solve[{w13[0] == 0, w13'[0] == 0, w13''[L] == 0, w13[L] == 0, mbc13 == 0},
            {p12, C[1], C[2], C[3], C[4]}]
```

w_{13}

```
In[138]:= {temp} = w13[s] /. sol13
In[139]:= w13[s_] = FullSimplify[temp]
```

$P_{(12)}$

```
In[140]:= {p12} = p12 /. sol13
In[141]:= p12 = Simplify[p12]
```

Reconstructing load P up to 14-th power of b

```
In[142]:= load[b_] = pcr + Sum[pi b^i, {i, 1, 12}]
```

Reconstructing the shape up to 14-th power of b

```
In[145]:= shape[b_] = Sum[wi[s] b^i, {i, 1, 13}]
```

Finding curvature

```
In[148]:= curv[b_] = D[shape[b], {s, 2}]
```